## Title

Optimization of 3D-Printed, Flexible, Rechargeable, Zinc-based Batteries via a Novel Gel Polymer Ionic Liquid Electrolyte



## Author

Winslow, Richard Lemuel

## Publication Date

2014

Peer reviewed|Thesis/dissertation

**Optimization of 3D-Printed, Flexible, Rechargeable, Zinc-based Batteries via a Novel Gel Polymer Ionic Liquid Electrolyte**

by

Richard Lemuel Winslow IV

A dissertation submitted in partial satisfaction of the

requirements for the degree of

Doctor of Philosophy

in

Engineering - Mechanical Engineering

in the

Graduate Division

of the

University of California, Berkeley

Committee in charge:

Professor Paul K. Wright, Chair
Professor James W. Evans
Associate Professor Hayden Taylor

Fall 2014

**Optimization of 3D-Printed, Flexible, Rechargeable, Zinc-based Batteries via a Novel Gel Polymer Ionic Liquid Electrolyte**

## Abstract

Optimization of 3D-Printed, Flexible, Rechargeable, Zinc-based Batteries via a Novel Gel Polymer Ionic Liquid Electrolyte

by

Richard Lemuel Winslow IV

Doctor of Philosophy in Engineering - Mechanical Engineering

University of California, Berkeley

Professor Paul K. Wright, Chair

The advent of printed and wearable electronics has generated a renewed interest in the development of new, novel form factors for high-capacity, flexible, rechargeable batteries. This research aims to enable such advancements by characterizing and optimizing the manufacturing processes and component interactions of printed, rechargeable, zinc-based batteries by utilizing an ionic liquid-based gel polymer electrolyte.

The ionic liquid 1-butyl-3-methylimidazolium trifluoromethanesulfonate ([BMIm][OTf]) with zinc trifluoromethanesulfonate ($Zn(OTf)_2$) salt dissolved in it comprises the electrolyte of interest. As a non-aqueous medium, it has been shown to enable rechargeability in zinc-based battery chemistries. When the electrolyte is combined with poly(vinylidenefluoride-co-hexafluoropropylene) (PVDF-HFP), a solid, stable, flexible electrolyte is produced. Is is through the lens of this material that the function and characterization of printed, rechargeable batteries comprised of zinc (Zn) and manganese dioxide-based ($MnO_2$) electrodes are investigated.

With the use of this novel electrolyte, additional variables must be taken into account in order to successfully and consistently produce high performance batteries. The printed electrode surface morphology, electrolyte composition, and manufacturing environment play significant roles in affecting the performance of the battery cells and the components within. To characterize these aspects, battery components were produced via stencil printing, dispenser printing, and casting. Their properties were investigated with electrochemical impedance spectroscopy, cyclic voltammetry, laser confocal microscopy, scanning electron microscopy, Karl Fischer titration, contact angle measurements, and cycle life tests.

The gel polymer electrolyte (GPE) was found to poorly wet the rough, wavy surfaces of the printed electrodes. Within features and cavities on the surface, air bubbles were trapped that increased the interfacial impedance and prevented cell cycling. This was overcome by wetting the interfaces with the ionic liquid-based electrolyte prior to cell assembly in order to produce cyclable batteries. With the manufacturing method determined and the surface morphology characterized, several electrolyte and gel polymer electrolyte com-

positions were investigated. Higher concentrations of $Zn(OTf)_2$ resulted in cells with higher discharge capacities and higher current densities during cyclic voltammetry tests indicating the importance of having adequate charge carriers within the electrolyte. The amount of environmental water absorbed by the electrolyte was also found to be a function of the quantity of dissolved $Zn(OTf)_2$, where more salt resulted in more higher water content. Cell testing and component characterization determined that the presence of some water within the electrolyte was beneficial to enable improved cell discharge capacities. As a result, it was shown that printed, rechargeable, zinc-based batteries can be manufactured successfully in an ambient laboratory environment without strict air quality control.

The optimal component compositions, as determined from the empirical analyses and characterization experiments, enabled the production of 25 cells with 100% yield. These cells exhibited an average discharge capacity of 0.6 $mAh/cm^2$ with a maximum of 1.0 $mAh/cm^2$ over many cycles. The cells also successfully powered a commercial, off-the-shelf microcontrol unit to confirm that printed, rechargeable, zinc-based batteries are capable of being deployed with conventional electronics.

The advancements made within this research have successfully produced and characterized printed, rechargeable, zinc-based batteries with an ionic liquid-based gel polymer electrolyte for printed and flexible electronics. The results presented herein will provide a basis with which many printed systems can be better understood and developed, especially for those comprised of multiple layers.

To my family and friends, for all of your love and support.

# Contents

# List of Figures

# List of Tables

# Acknowledgments

My time at UC Berkeley has been at times both easy and difficult, but always exciting and fulfilling. I cannot imagine what it would have been like without the support and guidance of so many people. I want to take this opportunity to thank all of them for being my strength through the years. I couldn't have done it without you.

First I would like to thank my parents, Rich and Harriet, and my sister, Maggie, for their constant support even from so many miles away. You have always been there to help me stand up through the triumphs and failures in and out of my academic career. Thank you for helping me to follow my dreams.

I would also like to thank my advisors, Prof. Paul K. Wright and Prof. James W. Evans, for supporting and guiding my work and allowing me to pursue solutions in the direction that I chose even when funding was running low. You were invaluable in teaching me how to navigate through the forest of research.

I would like to thank Dr. Peter Minor for not only having my back through the years, but also for helping to get me into Paul's lab so many years ago. Without your help, I might have left grad school permanently.

I would like to thank Dr. Alic Chen for being my first mentor in the Wright Lab. With your help, I learned how to conduct real research, a skill that no one else had taken the time to teach me.

I would like to thank Dr. Dana Carr for giving me strength every week and helping me navigate through some of my darkest moments. I would not have been able to persevere through grad school without your unwavering support. You have helped me emerge stronger than I thought I ever could be.

I would like to thank Dan Chapman for helping me maintain my sanity through the years of hard research and for becoming a friend that I always looked forward to seeing in the morning. Thank you for doing so much for me and many others whether it was asked of you or not.

Finally, I would like to thank all of my colleagues and friends for helping me along the path: Dr. Zuoqian Wang, Dr. Jayme Keist, Dr. Christine Ho, Dr. Chun Hsing Wu, Bernard Kim, Martin Cowell, Qian Zhang, Marco Salvioli Mariani, Grace Vasiknanonte, Jae Bin Ju, Dr. Abhinav Gaikwad, Dominic Cincione, Pit Pillatsch, Sean Wihera, Tracy Turner, Dr. Vince Battaglia at Lawrence Berkeley National Lab, Prof. Malcolm Keif at Cal Poly, San Luis Obispo, and Prof. Oliver M. O'Reilly.

My time at Berkeley has been an amazing adventure. I am privileged to have experienced it with all of you.

## 1. Hypothesis

The environment, printed electrode surface morphology, and eletrolyte composition play significant roles in determining the functionality of printed, rechargeable $Zn/MnO_2$ batteries with an ionic liquid-based gel polymer electrolyte.

## 2. Background

- Zinc Batteries
- Ionic Liquids
- Printed Manufacturing
- Gel Polymer Electrolytes

## 3. Experimental

- Develop design of experiments
- Manufacture electrode inks and electrolytes
- Manufacturing and Interfaces
- Electrolyte and Gel Polymer Compositions
- Water Interactions
- Component Characterization
- Full-Cell Cyclability
- Optimization and Integration

## 4. Conclusions

Printed, zinc-based batteries are successfully rechargeable with an ionic liquid-based gel polymer electrolyte, and their performance is indeed controlled by the manufacturing environment, printed surface morphology, and electrolyte composition.

# Chapter 1

# Introduction

Advancements in manufacturing have allowed electronics to move from the rigid circuit board to flexible substrates. Novel inks are being made to print sensors [76] and even energy harvesters [11]. To support these devices and the systems they are a part of, new forms of rechargeable, long-term energy storage must be produced that can be manufactured inline with these printed technologies. Several types of printed batteries have been researched and successfully fabricated [32, 31, 80, 30, 4, 27], yet a white space still exists to provide a full understanding of the printed interfaces and the interactions between the materials used. The goal of this research is to define many of the compositional and process boundaries that affect cell yield and capacity for the ionic liquid-based gel polymer electrolyte used in novel printed, rechargeable zinc batteries.

For printed, flexible applications, zinc-based batteries show a great deal of promise with their high theoretical gravimetric energy density and stability in air [53]. Unlike lithium-ion chemistries, zinc batteries are air stable and can be manufactured without the need for an inert environment to prevent material combustion. As such printed zinc-based batteries can be integrated directly into the manufacturing process of other devices without costly retrofits or additional environmental control.

Recent research into ionic liquid electrolytes has shown that zinc-based batteries can be recharged over one hundred times before failure [42, 45]. Such materials can enable cheap, rechargeable batteries. The ionic liquid electrolyte is a fluid that cannot simply be applied to free-standing electrodes, however. In order to integrate it with printed electrodes, a polymer must be added to create a solid, ionically-conductive film.

To prove device viability at laboratory scale, environments can be non-ideal and yield can be low. At the same time, special attention can be given to specific manufacturing variables that would normally not be controllable in larger production environments. Scaling up manufacturing, though, requires knowledge of the factors that affect many aspects of cell performance. The integration and use of an ionic liquid, a new class of material with many unknown properties and sensitivities, and a polymer to create a solid film add additional complexity to the manufacturing and process details that must be quantified and understood.

This work investigates the composition of and electrode interfacial interactions with a

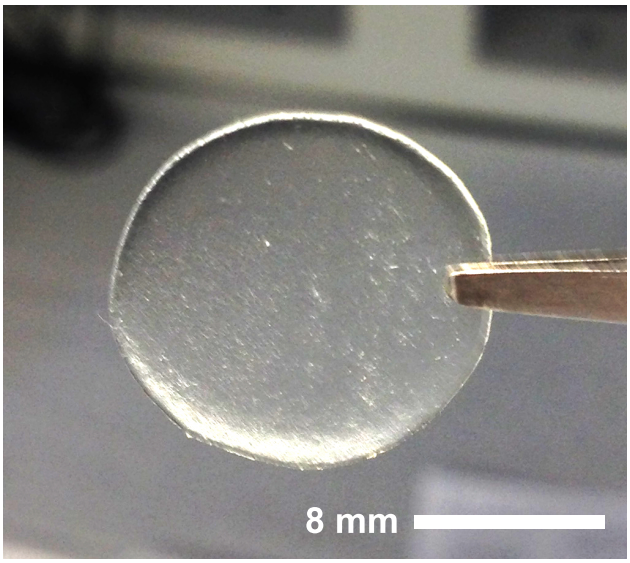


Figure 1.1: Solid ionic liquid-based gel polymer electrolyte.

ionic liquid-based gel polymer electrolyte. It aims to use those aspects to quantify how such a material affects full cell manufacturability and performance. This will enable a greater understanding of the process and environmental controls that must be in place to increase the manufacturing scale of printed energy storage with solid electrolytes from the laboratory to the marketplace.

The electrolyte of focus uses the ionic liquid 1-butyl-3-methylimidazolium trifluoromethanesulfonate ([BMIm][OTf]) with the salt zinc trifluoromethanesulfonate ($Zn(OTf)_2$) dissolved into it to form the electrolyte. This is then added to a solution of poly(vinylidene fluoride-co-hexafluoropropylene) (PVDF-HFP) dissolved in n-methylpyrrolidone (NMP) to form the gel polymer electrolyte of investigation.

This dissertation begins with the background of printed batteries, ionic liquids and their behavior and attributes in Chapter 2. It focuses on bounding the whitespace in the literature and provides the basis for research presented in further chapters. Chapter 3 presents the investigation into the manufacturing and characterization of the manganese dioxide ($MnO_2$) electrode and its interactions with the gel polymer electrolyte. The need for environmental process control is detailed in Chapter 5 through the investigation of the interactions between the electrolyte and water, both as an additive and from the environment in the form of humidity. Chapter 4 expands on the work by investigating additional gel polymer electrolyte compositions in order to understand what compositional factors most affect cell performance. Chapter 6 utilizes the findings in all previous chapters to determine material compositions that will yield the best performance and highest yield. Cells were made and integrated with an electrical circuit to determine real-world performance and this was reported in the chapter. The final section, Chapter 7, summarizes the findings and presents the recommendations of the researcher in addition to the potential future directions of the work.

## 1.1 Hypothesis

With reference to the present literature, it is hypothesized that the environment, printed electrode surface morphology, and electrolyte composition play significant roles in determining the functionality of printed, rechargeable $Zn/MnO_2$ batteries with an ionic liquid-based gel polymer electrolyte. The ability of the electrolyte to absorb water from the ambient environment may change its properties such that completed battery cells become non-functional or see a reduction in capacity. These effects can be quantified via several methods including cyclic voltammetry, electrochemical impedance spectroscopy, and Karl Fischer titration. The printed electrode surface has surface features that are expected to be directly influenced by the manufacturing method and may have an impact on the interactions at the electrode-electrolyte interface. These effects can be quantified with laser confocal microscopy, contact angle measurements, and full cell cycle tests. Finally, as the electrolyte composition changes relative to the amount of charge carriers and polymer binder, it is expected to have a quantifiable impact on cell performance and manufacturability. These effects can be quantified via electrochemical impedance spectroscopy, thermogravimetric analysis, and cyclic voltammetry amongst other methods.

# Chapter 2

# Printed Electrochemical Systems and Ionic Liquids

This chapter details the principles of battery operation and common metrics used to qualify their performance, along with zinc-based batteries, of which this research investigates. Electrolyte materials, specifically ionic liquids and gel polymer electrolytes are also discussed. Printed batteries, their achievements, and common manufacturing techniques are detailed in the following section. Battery material interfaces and models are then discussed. The final section describes the scope of the dissertation and research herein.

## 2.1 Battery Operating Principles

Charge is stored within a battery, also known as an electrochemical cell, within chemical bonds. A battery contains two electrodes, one where oxidation occurs called the anode, and the other where reduction occurs called the cathode. Both electrodes are connected by an ionically conductive medium called the electrolyte that facilitates the transport of ions between the two electrodes. The electrodes are then connected through an external circuit through which current, typically electrons, flows to provide sufficient power to the attached electronic systems. While a battery is being discharged or charged, two reactions are occurring simultaneously. Each is called a half reaction and together make up the overall reaction of the cell. A discharging battery is called a galvanic cell. As it discharges, the half reaction at the anode releases electrons and cations from the anode. The other half reaction at the cathode accepts those cations and electrons. For rechargeable cells, the polarity at the electrodes is reversed and a current is applied causing the reactions to run in the opposite direction. As an example, Figure 2.1 provides a schematic for these two types of cells with zinc and $MnO_2$ as the electrode materials and $NH_4Cl$ dissolved in $H_2O$. Note the existence of the current collector, a component used in batteries that connects to the circuit and typically has a higher electrical conductivity than the electrodes. The half reactions at the electrodes are

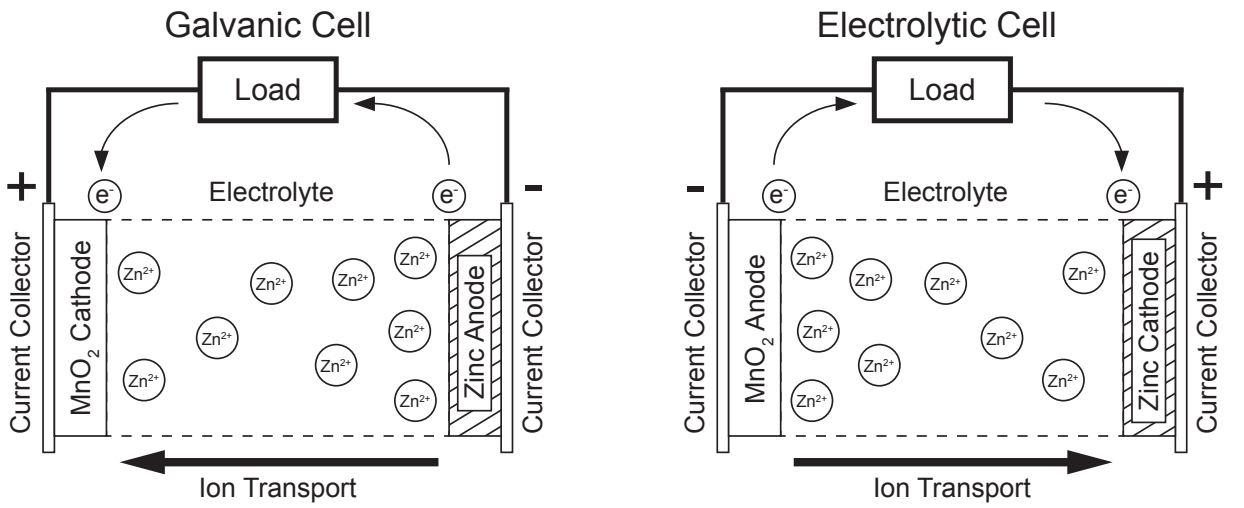


Figure 2.1: Schematic of galvanic and electrolytic zinc/$MnO_2$ cells during discharge and charge, respectively.

$$\mathrm{Zn_{(s)} \longrightarrow Zn^{2+}_{(aq)} + 2\,e^-} \tag{2.1}$$

$$\mathrm{2\,MnO_{2(s)} + 2\,e^- + 2\,NH_4Cl_{(aq)} \longrightarrow Mn_2O_{3(s)} + 2\,NH_{3(aq)} + H_2O_{(l)} + 2\,Cl^-} \tag{2.2}$$

and each has a potential that drives the process. These half reactions are always measured relative to the normal hydrogen electrode (NHE), also commonly referred to as the standard hydrogen electrode (SHE) [2]. This electrode has the half reaction described by

$$\mathrm{2\,H^+ + 2\,e^- \longrightarrow H_2} \tag{2.3}$$

and has a potential that is taken to be zero at all temperatures. When a reaction is measured relative to a NHE, the resulting value is called a standard potential. For example, the oxidation of zinc in Equation 2.1 has a standard potential of -0.76 V vs. NHE.

In order for the battery to continue to function, it must maintain charge neutrality within the electrolyte. As $Zn^{2+}$ cations become part of the solution during discharge, they move through the electrolyte to the cathode that has a high concentration of electrons, thus ensuring charge neutrality. The $Zn^{2+}$ cations have been shown to move into the crystal lattice of the $MnO_2$, known as intercalation, in order to react with the electrons [50] and maintain that charge neutrality. Common ways the two half reactions will cease include a lack of available zinc for reactions, saturation on the surface or in the crystal lattice of the cathode, and a rise in the impedance of the battery to a point at which it is not preferable for the reactions to occur.

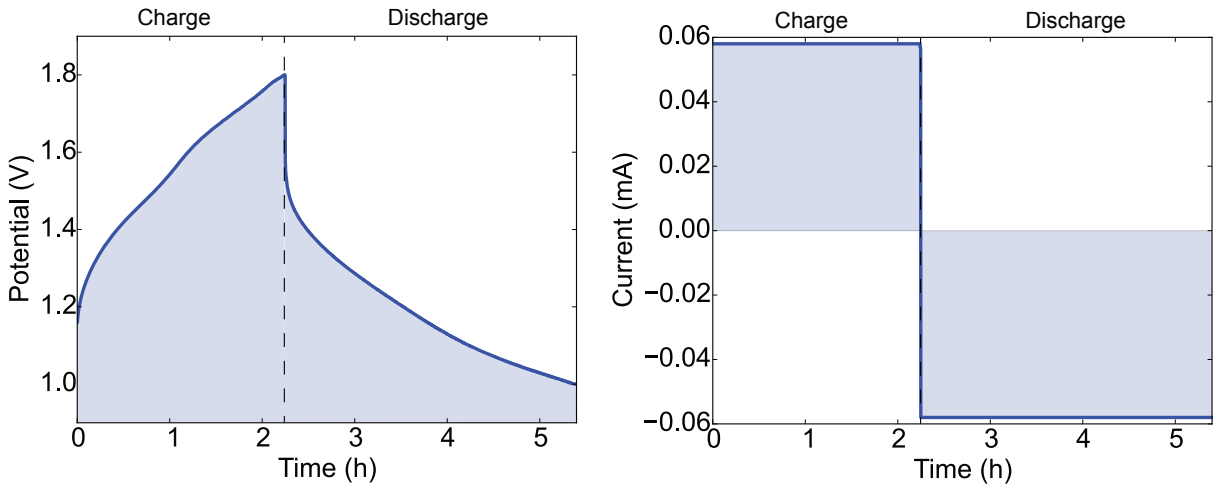


Figure 2.2: Charge and discharge voltage and current profiles over a single cycle for a $Zn/MnO_2$ cell with a [1:15]1:1:5 gel polymer electrolyte.

The performance of batteries can be described by many factors, the most common of which are the discharge capacity and energy capacity. By integrating over the charge and discharge parts of the voltage and current profiles, as shown in Figure 2.2, each capacity type can be determined. The discharge capacity is defined by

$$\text{Discharge Capacity} = \int_{\text{discharge}} I(t)dt \tag{2.4}$$

where $I$ is the current and $t$ is time, and the output energy capacity is defined by

$$\text{Output Energy Capacity} = \int_{\text{discharge}} I(t)V(t)dt \tag{2.5}$$

where $V$ is the voltage. Thus the discharge capacity, commonly referred to simply as the capacity as the discharge is what actually powers devices, has units of milliamp-hours (mAh) or amp-hours (Ah) depending on cell size. The energy capacity has units of watt-hours (Wh) or kilowatt-hours (kWh) again depending on cell size. Note that batteries are commonly designed to perform over a range of hours, thus all of the units use hours as opposed to another unit of time. Each of these values can also be normalized relative to volume (per $cm^3$), area (per $cm^2$), and mass (per g) to provide a basis for comparison between other battery chemistries and form factors.

From this set of graphs, the energy and coulombic efficiencies can be determined that help indicate how long a cell may last if allowed to cycle until failure. The coulombic efficiency quantifies how much charge has entered and left the cell from each cycle. A value greater than 1 indicates either the cell is not fully rechargeable, that side reactions may be taking

place, or both conditions. A value less than 1 indicates leakage of current. From Equation 2.4 we can determine the coulombic efficiency by taking the ratio of the amount of input to and output from the system during each part of the cycle. Thus the coulombic efficiency is defined as:

$$\text{Coulombic Efficiency} = \frac{\text{Discharge Capacity}}{\text{Charge Capacity}} = \frac{|\int_{\text{discharge}} I(t)dt|}{\int_{\text{charge}} I(t)dt} \tag{2.6}$$

The energy efficiency is found in a similar way as the coulombic efficiency. From Equation 2.5 we can determine the energy efficiency by taking the ratio of the energy input to and output from the cell during charge and discharge. Thus the energy efficiency is defined as:

$$\text{Energy Efficiency} = \frac{\text{Input Energy Capacity}}{\text{Output Energy Capacity}} \tag{2.7}$$

## 2.2 Zinc-based Batteries

The first true battery was invented by Alessandro Volta in 1800, known as the voltaic pile, that used zinc and copper plates as the electrodes with an electrode separator soaked in a salt water electrolyte [5]. Since then, zinc-based batteries, especially those composed of zinc and $MnO_2$, have become ubiquitous. The best known of these is most likely the alkaline cell.

Among the many benefits of zinc, it has high theoretical performance values, as shown in Figure 2.4. As noted previously, the capacity in Ah is a function of the amount of charge that a battery can provide. When zinc oxidizes it loses 2 electrons whereas lithium only loses one electron. Thus for the same mass of material, a $Zn/MnO_2$ cell can provide twice as much current as a lithium-ion cell can. Lithium-ion cells, though, operate at a higher potential than $Zn/MnO_2$ cells, approximately 3.7 V relative versus 1.5 V for a $Zn/MnO_2$ cell. This means that the lithium-ion cell can provide more power over the same amount of time, although the $Zn/MnO_2$ cell is not far behind [53].

One of the two main differences between zinc and lithium is that zinc is stable in ambient environments while lithium has the potential to react rather violently. This dramatically affects the environments each material can be manufactured in as well as the safety precautions that must be followed in production, storage, and use. This makes zinc an attractive choice for printed batteries because enclosing a large-scale printer in argon would be extraordinarily difficult and prohibitively expensive.

The other difference is rechargeability. While lithium-ion cells can be discharged and recharged potentially hundreds of times, zinc cells are typically only used as primary, or non-rechargeable, cells. This is because brittle, tree-like zinc structures called dendrites form on recharge within the cells and on the zinc surface. As such these structures can bridge the gap between the electrodes causing a short. If the brittle dendrites break off into the electrolyte, the zinc electrode has less material to contribute to the cell discharge and that results in a lower discharge capacity [42]. Additionally zinc oxide (ZnO) can form from

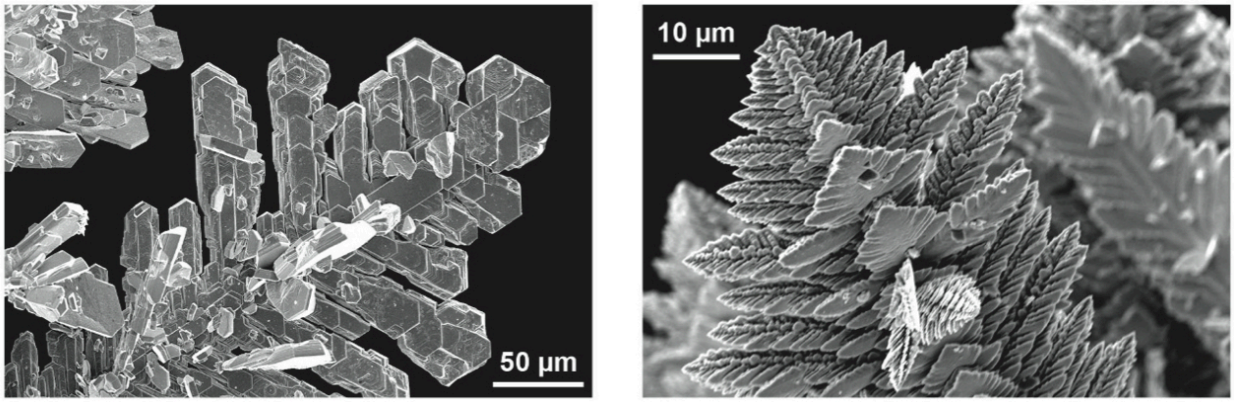


Figure 2.3: Dendrite formations after electrodeposition of Zn within a KOH solution [42].

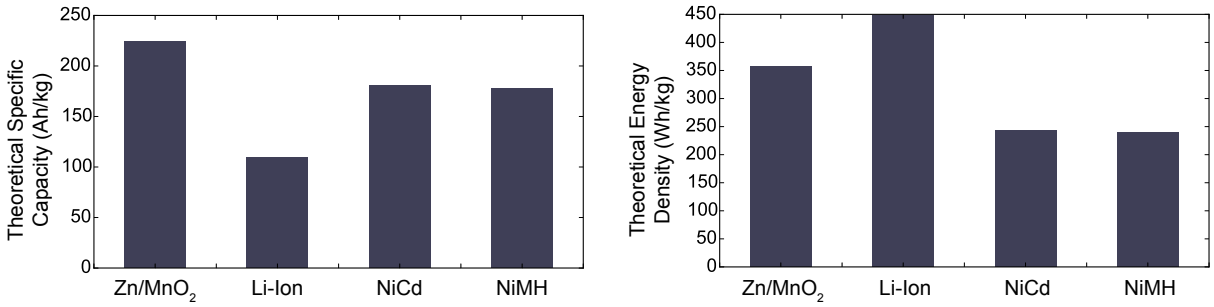


Figure 2.4: Theoretical performance for common battery chemistries: Zinc/Manganese Dioxide ($Zn/MnO_2$), Lithium Ion (Li-Ion), Nickel Cadmium (NiCd), Nickel Metal Hydride (NiMH) [53].

zincate ($Zn(OH)_4^{2-}$) that is in turn generated by reactions of $Zn_{(s)}$ with hydroxide ($OH^-$) ions. Research into alternative, non-aqueous electrolytes has proven fruitful for inhibiting the growth of dendrites and allowing zinc-based batteries to be recharged for a greater number of cycles [42, 33, 84]. With additional investigations into process control and manufacturing methods the hurdle of rechargeable zinc can be overcome, which will enable cheaper, safer energy storage.

## 2.3 Electrolyte Materials

This section provides an overview of ionic liquids as a material, their manufacture, and their use as novel electrolytes. Gel polymer electrolytes, common materials, and their use are also described. Finally the effect the environment may have on these materials is also discussed.

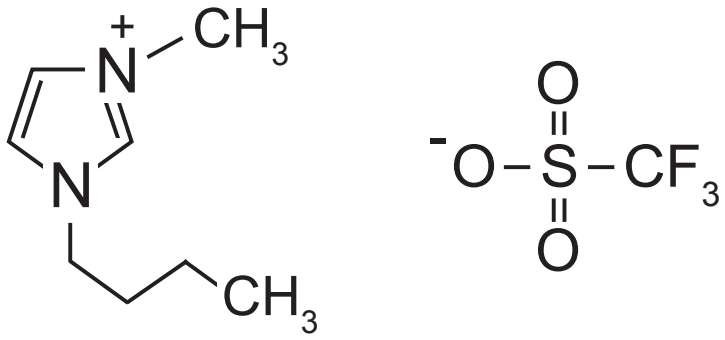

Figure 2.5: Molecular structure of 1-butyl-3-methylimidazolium trifluoromethanesulfonate ([BMIm][OTf]) with the large cation on the left and the small anion on the right.

### 2.3.1 Ionic Liquids

Ionic liquids (ILs) are a specific type of molten salt that has a very low melting point and is commonly liquid at room temperature. They are composed of large, bulky cations and smaller anions. The large difference in size between the cation and anion results in very low coordination between them such that solids do not form, although temporary ion pairs may manifest in the liquid [62, 88].

Typically the cation is composed of a central molecular structure with functional branches coming off at one or several points. It also has a direct influence on the viscosity of the liquid via intermolecular van der Waals interactions [82, 57]. Conversely anions, as a result of their small size, do not have any central structure with branches. They also have been shown to reduce the melting point of the IL [82]. Many hundreds of possible combinations of molecules are available that form ionic liquids. As a result they are commonly called designer materials. Imidazolium-, pyridinium-, pyrrolidinium-, and ammonium-based cations are common in many applications [24, 88]. Conversely hexafluorophosphate, tetrafluoroborate, trifluoromethanesulfonate (triflate), and acetate are just a few common anions [24, 88]. One example of an ionic liquid, and the material used in this research, is 1-butyl-3-methylimidazolium trifluoromethanesulfonate ([BMIm][OTf]) as shown in Figure 2.5.

ILs are commonly made by combining a halide salt, that is a salt that contains a chemical from the halogen group, and an anion salt, that is a salt that includes the desired anion with which a metathesis reaction can occur, together in a solvent [82]. Note that a metathesis reaction is simply the exchange of bonds between two chemical species such that their reaction can be described by $AB + CD \longrightarrow AD + CB$. Silver salts are commonly used because they have a very low solubility in the solvent methanol. This allows the desired chemical product, the ionic liquid, to be extracted from the solution with fewer impurities [82].

This results in a liquid with unique properties including extremely low vapor pressures [69, 88], high thermal stability [69, 61] and high electrical stability [44]. They are also known to be good solvents [81]. The combination of all of these properties gives them an additional

title of "green solvents" because they can be used in an application, removed, cleaned, and reused with little to no loss of material [81]. While these properties are very beneficial, "green" can be considered a misnomer because many ionic liquids are considered hazardous [7].

All of these properties make ILs ideal candidates for electrolytes in next-generation batteries. Their ability to dissolve many materials means they can be used for all types of battery chemistries from zinc to lithium. Like many solvents, ionic liquids commonly require a salt to be dissolved into them to turn them into an ionically conductive electrolyte for the desired chemistry, a zinc salt or lithium salt for example [24]. That salt, though, must include the anion used within the ionic liquid itself [14]. For example, for a $Zn/MnO_2$ battery chemistry with a [BMIm][OTf] ionic liquid as the base for the electrolyte, the salt $Zn(OTf)_2$ must be used. They have been shown to have ionic conductivities on the order of mS/cm [24] and resulted in the development of successful proof-of-concept battery cells [87, 88, 66, 85, 33, 42].

### 2.3.2 Gel Polymer Electrolytes

With new geometries, manufacturing methods, and materials available to batteries, gel polymer electrolytes (GPEs) are an ideal candidate for the ionically conductive medium. Such materials are composed of two main components: the liquid electrolyte and the polymer matrix that holds it. While the electrolyte is selected based on proven experiments with the desired battery chemistry, the polymer must be chosen such that it can sufficiently retain the electrolyte without dramatically impeding ionic conduction, withstand the electrical potentials the cell will operate at, remain inert during cell charge and discharge, and be easily integrated with the battery manufacturing process.

Typically GPEs are made by first dissolving the desired polymer in a solvent to form a gel. The electrolyte is then added to the gel solution and mixed, forming the GPE solution. To form the final solid film, the GPE solution is cast on the desired surface in the desired shape. The solvent is then driven out either by elevated temperatures or simply the vapor pressure the solvent applies upon the surrounding environment. After the solvent evaporates, the solid polymer is left with the electrolyte trapped within it [22, 34]. Commonly used polymers include poly(vinylidene fluoride-co-hexafluoropropylene) (PVDF-HFP) [22], poly(acrylonitrile) (PAN) [73], poly(ethylene oxide) (PEO) [74], and poly(methyl methacrylate) (PMMA) [74].

One important consideration during polymer selection is the structure that results after removing the solvent and the method used. A porous, amorphous film with low polymer crystallinity is commonly desired, although many different structures can form as shown in Figure 2.6. As a result, the porosity and pathways available for ions to travel can vary dramatically. These structures also affect the ionic conductivity, which can be anywhere between $10^{-8}$ and $10^{-2}$ mS/cm depending on the final morphology of the film and the amount of electrolyte present [12, 8, 41, 16]. As expected pure electrolytes have higher conductivities, but as noted previously they are typically liquid in nature.

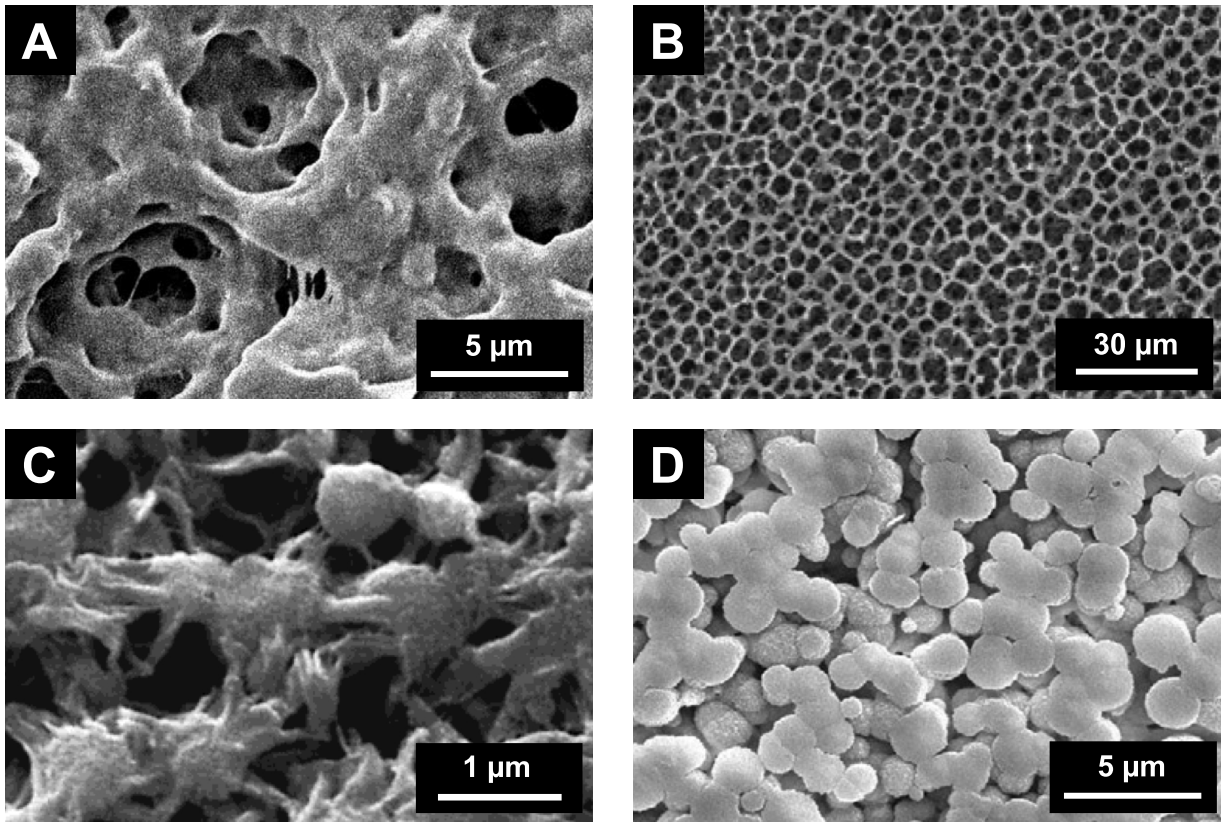


Figure 2.6: Various morphologies arising from the polymer selection and manufacturing process. A) PVDF-HFP reinforced by PEGDMA network [12]. B) Supercritical $CO_2$ induced phase separation of PVDF-HFP solution [8]. C) PVDF film made via phase inversion [41]. D) PVDF/PEO-PPO-PEO blend via thermally-induced phase separation [16].

Despite the drop in ionic conductivity, GPEs have been noted for their potential to inhibit the growth of dendrites [85]. The complex pathways within the GPE structure could assist in preventing dendrites from growing across the electrodes and causing a short.

### 2.3.3 Environmental Interactions

With new materials come new variables. Most traditional electrolytes are aqueous in nature and not concerned with the humidity or composition of their manufacturing environment. The switch to ionic liquids as the ionically conductive medium, addition of polymers for generating solid or semi-solid films, and use of organic solvents to tune the rheology for manufacturing has required that the environmental conditions and their effects be quantified and understood. Ionic liquids in particular may be very susceptible to the water present in air at ambient conditions. Research has shown that the anion present in the IL has an effect

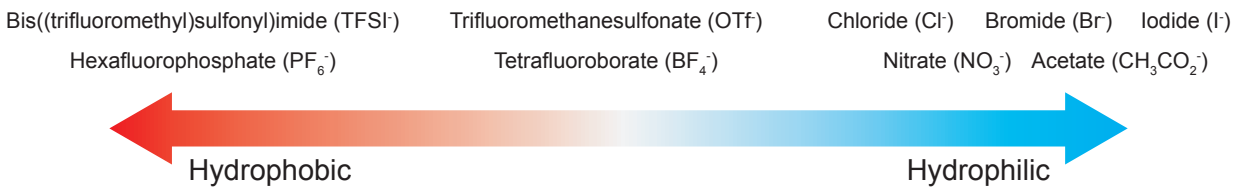


Figure 2.7: Hydrophobic/hydrophilic properties of several types of anions common in ionic liquids [88].

on the interactions with the material and water as shown in Figure 2.7 [88]. The alkyl chain length on the cation has also been shown to affect the amount of water that can be absorbed into the IL [9].

With this knowledge, models have been developed in an attempt to understand the solubility of water within ionic liquids [68]. They still require some empirical data to calculate the result, though. With knowing the hydrophobicity or hydrophilicity of the IL, one can expect certain environmental interactions. The results by Cao *et al.* elucidate the extent of those interactions for the IL 1-butyl-3-methylimidazoilum tetrafluoroborate as shown in Figure 2.8. It is expected that higher relative humidities would result in a greater mass of dissolved water, but the pronounced effect with temperature presents a unique conundrum. GPEs must be dried, and common manufacturing methods use elevated temperatures to achieve shorter drying times. If GPEs are placed in those elevated temperatures with ambient air, there is a high probability that they could rapidly absorb water from the environment.

Water in ionic liquids has been shown to affect their density, molar volume, surface tension, and viscosity [71, 78]. Despite this the effect water has on the capacity or cycle life of cells that use ionic liquids is unknown. For lithium cells water can be catastrophic, causing cells to burn spontaneously. Conversely zinc is stable in such environments. The additional water may generate side reactions, affect cell capacity, and affect the ionic conductivity of the electrolyte and GPE, although no data have yet been generated on such a topic.

## 2.4 Printed Batteries

The development of printed electronics has caused an increase in interest in the production of batteries that can be manufactured inline using the same methods as the rest of the device. The feasibility of such batteries has been shown by many groups through the utilization of different chemistries, form factors, and manufacturing techniques.

Ghiurcan *et al.* developed a non-rechargeable, thick-film, printed, zinc-alkaline battery on an alumina substrate with current collectors made with a commercial, conductive silver ink. They created custom manganese dioxide ($MnO_2$) cathode and zinc (Zn) anode inks with various compositions of polyethylene oxide (PEO) and other binders to attain the desired properties [27]. These were then printed with a stainless steel stencil onto the silver traces.

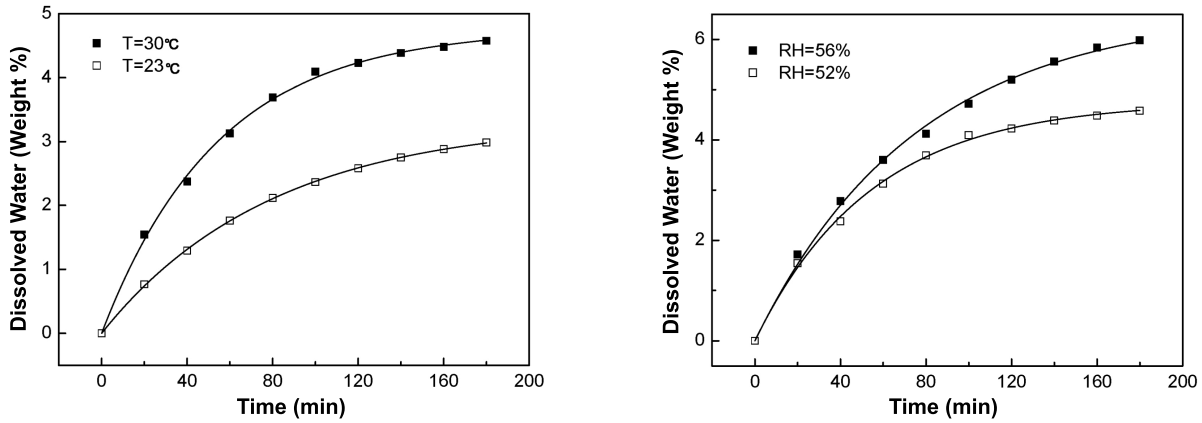


Figure 2.8: Left: The effect of temperature (T) on water sorption for [BMIm][$BF_4$] with a constant relative humidity of 52%. Right: The effect of relative humidity (RH) on water sorption for [BMIm][$BF_4$] with a constant temperature of 30 °C [88].

The potassium hydroxide (KOH) electrolyte and paper separator, though, were not printed. Droplets of the electrolyte were added to the electrodes and separator to wet their surfaces before being hand-assembled. They were able to achieve discharge capacities between 3 and 4 mAh/$cm^2$ and provided a reference for what could be possible with thick-film (approximately 100 $\mu$m thick) manufacturing techniques for batteries [27].

Other groups have expanded upon these principles. Tam *et al.* developed a rechargeable, thick-film, nickel-hydrogen battery [77]. Braam *et al.* optimized their ink compositions to produce non-rechargeable, silver-zinc batteries able to be discharged with a current density of 1.8 mA/$cm^2$ [4]. Gaikwad *et al.* produced a flexible, high-potential array of printed Zn-$MnO_2$ alkaline batteries [23]. Finally, Ho *et al.* proved the feasibility of printed, thick-film, Zn-$MnO_2$ batteries by utilizing an ionic liquid-based electrolyte held within a solid matrix of polymer [31]. Unfortunately, while each piece of research proved the feasibility of their respective chemistries and manufacturing process, their optimization methods, materials interactions, and system and component characterizations were often left uninvestigated.

### 2.4.1 Manufacturing Methods

Many methods of printing exist to produce devices and components at different scales. For high throughput, that is where printing speeds can be measured on the order of meters per second, flexographic and gravure printing are common. Dispenser and ink jet are commonly low throughput and are excellent for lab and research scales. Finally stencil casting and screen printing bridge the gap by having methods of integration with high-throughput processes, but can easily and cheaply be utilized at the much smaller lab scale. The acceptable ink viscosities for each printing process are described in Table 2.1.

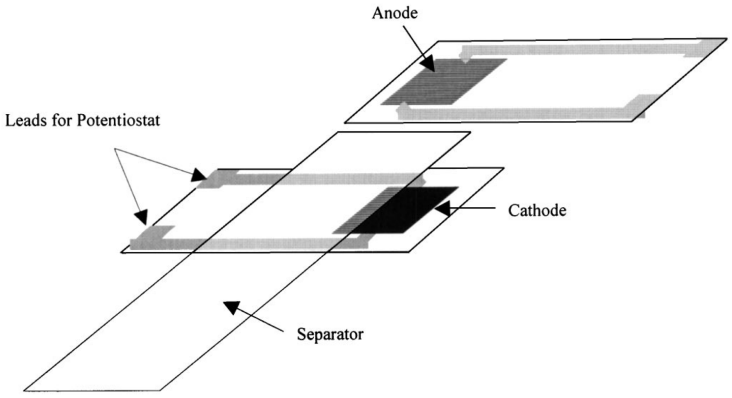


Figure 2.9: Schematic of clamped, printed prototype alkaline cell [27].

Table 2.1: Acceptable ink viscosities for common printing methods [28, 34, 43, 51].

| **Method** | **Viscosity Range (cP)** | **Common Film Thickness ($\mu$m)** |
|---|---|---|
| Flexographic | 50-500 | 1-5 |
| Gravure | 50-200 | 1-3 |
| Screen | 1000-10,000 | 1-12 |
| Stencil | Ink must flow | Limited by stencil thickness |
| Dispenser | 10-1,000,000 | 10-150 |
| Ink jet | 1-30 | $<1\mu$m |

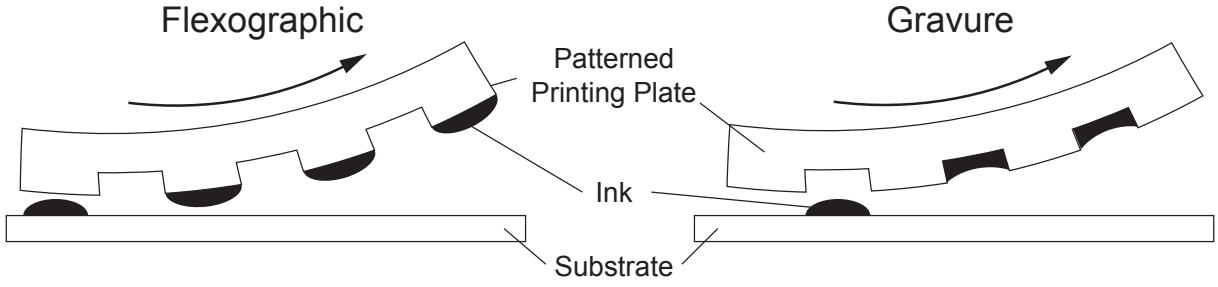


Figure 2.10: Methods of transferring ink for flexographic and gravure printing.

Despite having similar acceptable ranges of ink viscosity and both being contact-printing processes where the printing plate directly meets the substrate, flexographic and gravure printing have distinctly different methods of depositing ink. Both use a patterned surface known as a printing plate to produce a desired image. The differences between the two are illustrated in Figure 2.10 that shows the cross-section of the printing plate and the location of the ink for each printing method.

Flexographic printing uses a combination of rollers to coat raised portions of the printing plate where the image lies. Pressure is then applied by the printing plate onto the substrate to transfer the ink. The flexographic printing plates are often made of a soft photopolymer that deforms slightly with the application of pressure [43].

Gravure printing also uses a combination of rollers to coat the printing plate, but tiny indentations known as cells within the printing plate contain the image to be printed instead of peaks as with flexographic printing. After applying the ink, any excess is removed from the top of the gravure printing plate by a doctor blade. Pressure is applied by the printing plate to the substrate to transfer the ink, as with flexographic printing, but in this case the substrate must deform slightly to enter the grooves and accept the ink. To withstand the pressures applied, the printing plate is commonly made of steel and has the desired image laser-engraved. In order to ensure an even and controlled print, the image on the printing plate is broken up into individual cells of similar or equal size. After printing the deposited ink then reflows slightly to merge with the ink from other cells to form the full image [43].

Screen printing, unlike flexographic and gravure printing, does not use rollers or a printing plate to transfer the ink. Instead a mesh screen (hence its namesake) is stretched across a metal or wooden frame. A positive mask is then developed on it to allow ink to pass through only in predefined regions. The mask is commonly made by using a photo-sensitive emulsion that cures under ultraviolet light. To print the desired image, a line of ink is placed at one end of the screen and then drawn with a doctor blade over the areas the mask has exposed. As the doctor blade moves across the screen, it stretches it slightly so that only the ink and not the screen itself makes contact with the substrate [43].

Stencil printing is very similar to screen printing. Instead of having a mask made on a screen though, the mask itself is solid. The openings are called wells and ink fills them as it is drawn over the mask. As a result, the mask is in full contact with the substrate during printing. Because the mask is the only control layer in the printing process, all of the geometry in the desired image must be connected to each other. For example, a bullseye cannot be printed without modification because the internal circle would be free to move during printing [43].

Dispenser printing, unlike the other processes, is a raster printing process whereby a pneumatic controller applies metered amounts of air to a syringe filled with ink. The tip of the syringe is placed just above the substrate as droplets of ink are deposited with each burst of air. In order to create the desired shapes and images, the substrate is attached to a movable stage that can translate in the X- and Y-directions while the syringe armature translates in the Z-direction. It requires no mask and can produce virtually any 2-dimensional shape but is limited to the the area of travel of the stage and the size of the syringe tip. Hence larger

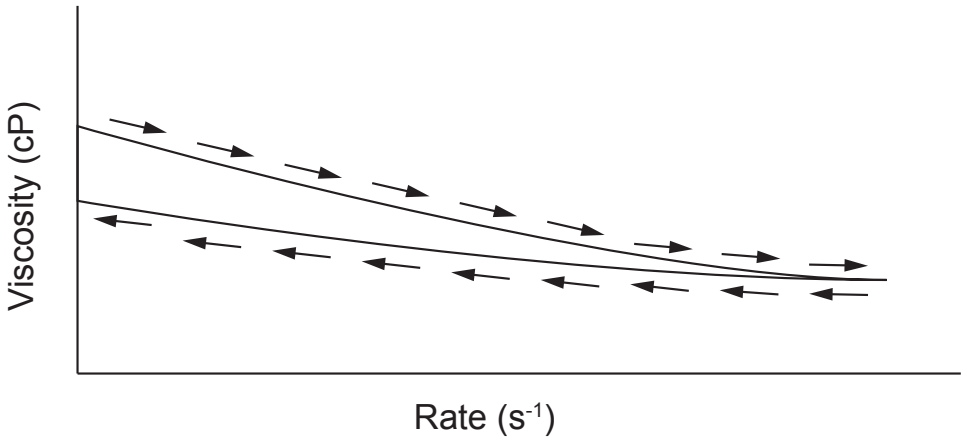


Figure 2.11: Viscosity hysteresis loop for a thixotropic material.

diameter tips can dispense more ink, but will have lower resolution.

Ink jet printing is also a non-contact printing process and most similar to dispenser printing. In place of bursts of pneumatic pressure is a piezoelectric crystal that changes shape when a potential is applied to it which forces a droplet of ink out of the nozzle. While dispenser printing has parts and pixels on the order of millimeters to centimeters, the parts that control ink jet printing are sized on the tens of microns. Inks must have very low viscosities, have very small particle sizes, and be well-mixed and homogeneous to prevent the buildup of particles within the system [43].

These printing processes rely on a fluid property called thixotropy, such that the viscosity of the ink is time dependent and will continue to drop when sheared, even if the shear rate remains constant [28]. Such a feature is commonly found in non-Newtonian fluids and is often called shear thinning. After being printed, the viscosity of the ink returns to its initial value as it rests undisturbed. Such materials exhibit a hysteresis loop of their viscosity, as shown in Figure 2.11.

Many of the printing processes are unfeasible to work with at laboratory scales. Batteries are also limited by the amount of mass of the reactive material available at the electrodes, so thick films are desirable. Thus for experimental and manufacturing flexibility, dispenser and stencil printing are used in this research.

## 2.5 Interfaces

Despite many years of research, the direct influence of the interfaces on battery performance is still being investigated. The morphology of the electrodes surface does, as one would expect, have an effect on what happens at the interface with the electrolyte, although it is dependent upon many factors including which phenomenon is being investigated.

The investigation into the effect of electrode structure on cell performance began with the development of porous electrode theory. The theory presented a model of porous electrodes such that the exact distribution and geometry of the material could be neglected. Conversely the model could be described by features like porosity and volume-average surface area that are easily experimentally determined. As a result of these assumptions, the model is mainly applicable to systems in dilute solutions with only two phases of material where the shape-change of the electrodes is minimal [60].

In 1968 De Levie modeled the double-layer capacitance of specific sawtooth morphologies of platinum electrodes in a KOH solution and through many observations and simplifications elucidated the problems associated with interpreting data with rough electrodes [17]. He concluded that many of the effects were only able to be sufficiently quantified if the surface was smooth, as with a flat plate. If that was not achievable, the surface was to be made very rough, as with a brush electrode. In addition, his research noted that unquantified electrode surfaces could cast doubt on the results from electrochemical tests.

As a result of these conclusions, it is evident that investigations into the surface morphology of electrodes and their interactions with the electrolyte are very important. Unfortunately the simplifications made, as noted by the authors, cause the models to break down when non-dilute, non-liquid materials are used. Thus until accurate predictive models for solid electrolytes and non-ideal electrodes are determined, empirical methods must suffice in quantifying what happens at the interfaces. Electrochemical impedance spectroscopy [3, 55], cyclic voltammetry [56], and direct inspection of surfaces [18, 36] can provide data that explain what the morphologies are and what happens at the interfaces. The empirical nature of these methods, though, requires that these experiments be run for all new combinations of materials and battery compositions.

## 2.6 Scope of Dissertation

A large amount of whitespace exists in the literature related to the understanding of ionic liquids as electrolytes, their interactions with polymers as solid electrolytes, and their interactions with various electrode morphologies. In order to produce batteries with higher capacities, longer cycle lives, and easier manufacturability, each of those points must be quantified and understood. The benefits afforded by changing the electrolyte to an ionic liquid reinforce the need to investigate each of these phenomena. Therefore it is important to focus on each of the areas through the lens of electrolyte and battery performance. The aim of this research is to understand what aspects of ionic liquids affect cell capacity, their limitations both electrochemically or environmentally, and the most effective way to manufacture functional batteries with them.

Zinc and manganese dioxide ($MnO_2$) were chosen for the battery chemistry because of their stability in air and their high theoretical capacities. The ionic liquid 1-butyl-3-methylimidazolium trifluoromethanesulfonate ([BMIm][OTf]) was chosen as the basis of the electrolyte predominately because of its compatibility with zinc and $MnO_2$ [33], abil-

ity to make that chemistry rechargeable [42], and hydrophobic/hydrophilic properties [10]. Poly(vinylidenefluoride-co-hexafluoropropylene) (PVDF-HFP) was chosen for the breadth of research that shows its compatibility with ionic liquids to form stable GPEs [38].

Several factors are known to influence the performance of electrolytes, gel polymer electrolytes, their manufacturability, and their interactions with the electrodes. These include salt concentration, water concentration, polymer concentration, environmental humidity, temperature, material selection, and surface morphology. This project investigated the influence of those factors on the electrolyte, GPE, and the full cell performance in order to improve and optimize manufacturability, cell cycle life, cell capacity, and cell yield.

# Chapter 3

# Manufacturing Process and Layer Interfaces

The objective of this chapter is to compare the effects that result from stencil and dispenser printing on the resulting electrode surface and how those features interact with the gel polymer electrolyte. It achieves this through an investigation of the morphology of the printed electrodes composed of $MnO_2$, acetylene black, and PVDF-HFP and a characteristic gel polymer electrolyte composed of $Zn(OTf)_2$, [BMIm][OTf], and PVDF-HFP. Section 3.1 provides a brief overview of the methods of surface wetting measurements, Fourier transforms, laser confocal microscopy, and scanning electron microscopy used to conduct the experiments and the results that can be determined from each. Section 3.2 discusses the use of those methods to acquire data in a controlled manner, including ink and electrolyte making, electrode manufacturing, imaging techniques, surface analysis, contact angle measurements, and cell manufacturing. This section also discusses the different inks used and the reasoning behind their compositions. The final section provides an overview of the conclusions gathered from the experiments presented.

## 3.1 Surface Analysis Methods

This section overviews the methods and techniques used to characterize and qualify the surfaces of the electrodes under investigation. Surface wetting, Fourier transforms, laser confocal microscopy, and scanning electron microscopy were used to determine the interactions between surfaces, the roughness and waviness of each electrode, and the overall quality of the printed components.

### 3.1.1 Surface Wetting

For a given solid surface, a liquid droplet will form a specific shape as a result of the surface energies between it, the surface, and the surrounding environment. Young originally

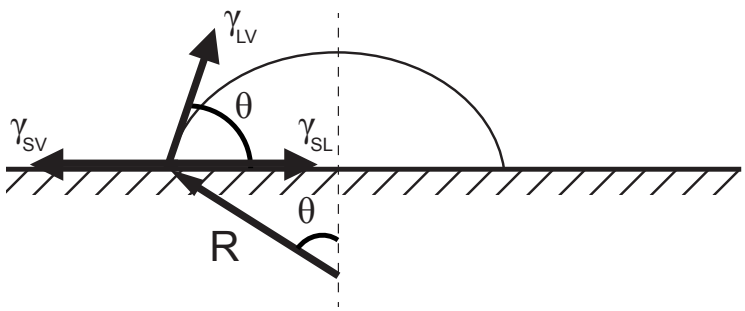


Figure 3.1: Graphical representation of of Young's equation for contact angle measurements via vector sum.

described the phenomenon as a balance of surface energies at the interface between the solid, liquid, and vapor substances, which was given by

$$\gamma_{LV} cos(\theta) = \gamma_{SV} - \gamma_{SL} \tag{3.1}$$

The derivation of Equation 3.1 can be found via thermodynamics by starting with a droplet of liquid of radius $R$ on an ideally flat surface, where $\theta$ denotes the contact angle, $V$ is the volume, and $S$ is the area of the liquid-air interface as shown in Figure 3.1. The volume of that droplet and the area of the interface are defined by

$$V = \frac{\pi R^3}{3}(1 - cos\theta)^2(2 + cos\theta) \tag{3.2}$$

$$S = 2\pi R^2(1 - cos\theta). \tag{3.3}$$

The Gibbs free energy of the droplet is then expressed by

$$G = \gamma_{LV} S + \pi(Rsin\theta)^2(\gamma_{SL} - \gamma_{SV}) = \gamma S - \pi(Rsin\theta)^2 a \tag{3.4}$$

where $\gamma_{LV}$ is the surface tension at the liquid-vapor interface, $\gamma_{SL}$ is the surface tension at the solid-liquid interface, $\gamma_{SV}$ is the surface tension at the solid-vapor interface, and $a$ is $\gamma_{SV} - \gamma_{SL}$ for a flat, homogeneous surface. Assuming that the volume of the droplet is constant, Equations 3.2 and 3.3 can be substituted into 3.4 to yield

$$G = \left[\frac{9\pi V^2}{(1 - cos\theta)(2 + cos\theta)^2}\right]^{1/3} (2\gamma_{LV} - a(1 + cos\theta)) \tag{3.5}$$

where $G$ is now a function of only the contact angle, $\theta$. Taking the derivative of $G$ with respect to $\theta$ yields

$$\frac{dG}{d\theta} = \left[\frac{9\pi V^2}{(1 - cos\theta)^4(2 + cos\theta)^5}\right]^{1/3} 2(a - \gamma_{LV} cos\theta) sin\theta. \tag{3.6}$$

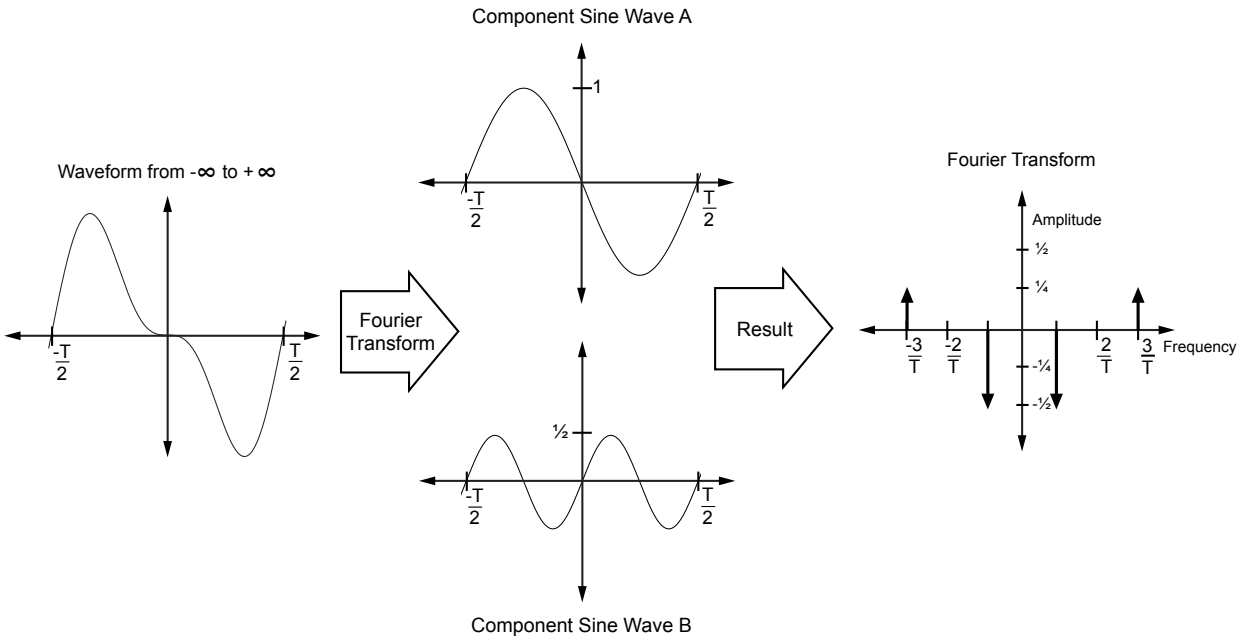


Figure 3.2: Graphical explanation of Fourier transform.

Thus $\frac{dG}{d\theta}(\theta = \theta_{Equilibrium}) = 0$ is fulfilled when $a = \gamma_{LV}$ yielding

$$\gamma_{LV} cos(\theta) = \gamma_{SV} - \gamma_{SL}. \tag{3.7}$$

While non-homogeneous surfaces and more complex systems cannot be described accurately by Young's equation and require additional derivation, the presence of the contact angle remains to explain the interactions the interfaces between multiple materials. [83].

### 3.1.2 Fourier Transforms

The Fourier transform is a method of decomposing a waveform in the time or spatial domain into a sum of sinusoids with different amplitudes in the frequency domain. The resulting spectrum provides a basis for filtering and analyzing waveforms of many types. For example Figure 3.2 shows how a waveform composed of sine waves A and B is broken into its constituent parts. The resulting graph in the frequency domain shows the contribution of each waveform at its specific frequency and amplitude.

The Fourier integral that accomplishes the transformation is stated as

$$H(f) = \int_{-\infty}^{\infty} h(t) e^{-j2\pi ft} dt \tag{3.8}$$

where $h(t)$ is the function in the time domain to be transformed, $H(f)$ is the resulting frequency domain function, $f$ is the frequency, $t$ is time, and $j = \sqrt{-1}$ [6].

After performing operations on $H(f)$ in the frequency domain, $h(t)$ in the time domain can be retrieved by performing an inverse Fourier transform on $H(f)$, defined as

$$h(t) = \int_{-\infty}^{\infty} H(f) e^{j2\pi ft} df \tag{3.9}$$

The functions $h(t)$ and $H(f)$ are thus described as a Fourier transform pair.

For use in computer algorithms however, only numerical integration is possible, thus a suitable Fourier transform pair must be developed for such a method of computation. For a sampled signal that is non-periodic, this is called the discrete Fourier transform (DFT). The function $h(t)$ is normally continuous in the time or spatial domain for use in conducting Fourier transformations, so it must be sampled over only a finite number of points that will most closely approximate the complete Fourier transform. Beginning from the notion that the time-domain waveform $h(t)$ must be sampled at some interval T and some time-domain sampling function $\Delta_0(t)$, the sampled function can be written as

$$\begin{aligned} h(t)\Delta_0(t) &= h(t) \sum_{k=-\infty}^{\infty} \delta(t - kT) \\ &= \sum_{k=-\infty}^{\infty} h(kT)\delta(t - kT) \end{aligned} \tag{3.10}$$

Following Brigham's derivation produces the common form of the DFT given by

$$\begin{aligned} G(\frac{n}{NT}) &= \sum_{k=0}^{N-1} g(kT) e^{-j2\pi nk/N} \\ & n = 0, 1, ..., N-1 \end{aligned} \tag{3.11}$$

and the discrete inverse Fourier transform is given by

$$\begin{aligned} g(kT) &= \frac{1}{N} \sum_{n=0}^{N-1} G(\frac{n}{NT}) e^{j2\pi nk/N} \\ & k = 0, 1, ..., N-1 \end{aligned} \tag{3.12}$$

where N is the number of samples, n and k are the sample indexes in the proper domain, and T is the sampling interval [6].

Note that Equation 3.11 produces a series of N equations, one at each sample. An algorithm can be produced to solve this series of equations. The fast Fourier transform (FFT) is simply the algorithm that can solve the system of equations in $O(NlogN)$ operations, whereas solving the DFT directly would require $O(N^2)$ operations [6]. The algorithm itself is omitted for brevity, but an inspection of Figure 3.3 shows the computational benefit of the development of the FFT.

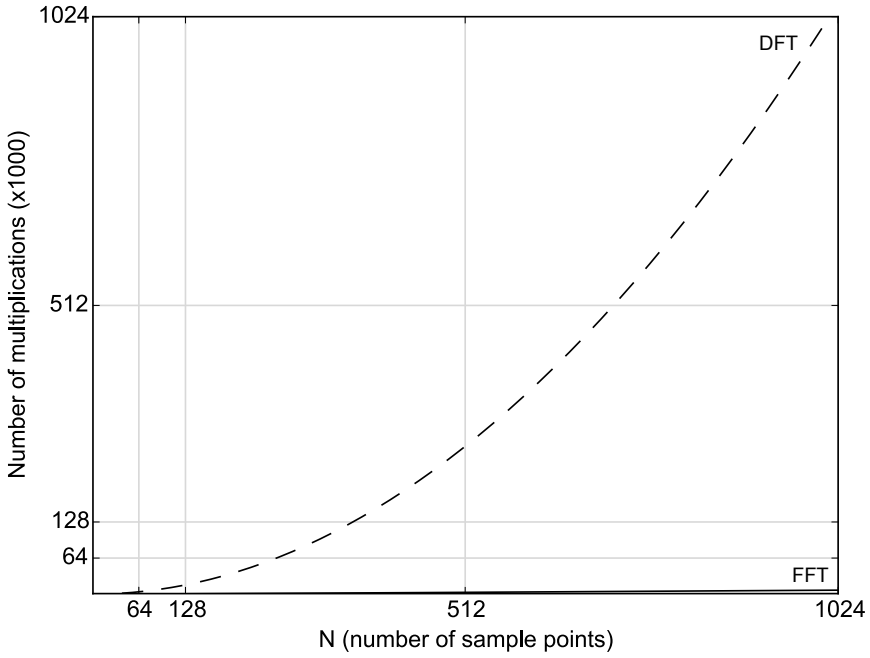


Figure 3.3: Comparison of number of operations between DFT and FFT.

### 3.1.3 Laser Confocal Microscopy

While laser confocal microscopy provides several benefits over other microscopy methods, one of the most advantageous is the ability to rapidly acquire a 3-dimensional surface map. Prasad *et al.* provide a succinct description of how such a microscope functions [65]. Laser light is first reflected by a dichroic mirror onto a set of rotating mirrors. This allows the microscope to raster along a surface and to illuminate individual points. The light that reflects off of the surface at the point that receives the laser light is reflected across the rotating mirrors and through the dichroic mirror. Before it is received by the photodetector, it passes through a pinhole filter placed in the conjugate focal plane, thus rejecting the majority of out-of-focus light reflected from of the target surface. This provides clear, crisp images within the focal plane. The microscope then steps vertically across a sample to acquire the necessary sections to produce the 3D map [65].

### 3.1.4 Scanning Electron Microscopy

At the basic level, a scanning electron microscope bombards an object of interest with a beam of high-energy electrons and, through the use of special detectors that are sensitive to the reflected electrons, produces an image from the interactions between the electrons and the object. Those interactions can be classified as either elastic or inelastic [89]. Zhou *et al.* explain how the elastic interactions are essentially deflections, where the electron is redirected by the atomic nuclei or outer shell electrons of similar energy in the surface of interest. Such

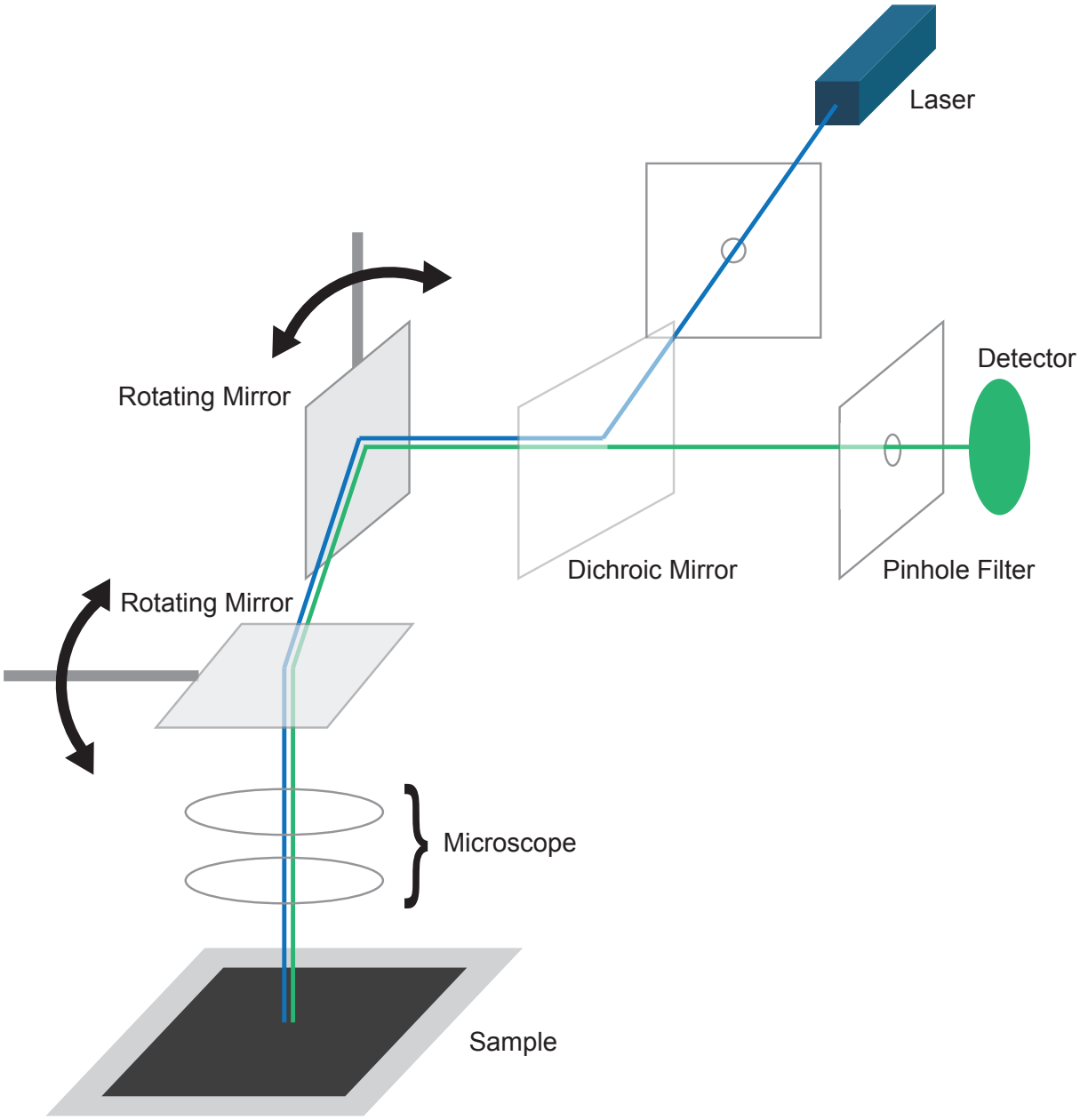


Figure 3.4: Components and orientation of confocal microscope parts.

interactions give rise to backscattered electrons that can be used to produce an image of the surface. Inelastic interactions are absorptions into the structure that can produce secondary electrons or other emissions such as x-rays, Auger electrons, or cathodoluminescence.

Backscattered electrons (BSEs) are defined by Zhou *et al.* as electrons "[that have] undergone single or multiple scattering events [that] escape from the surface with an energy greater than 50 eV." Depending on the material to be imaged, different amounts of the electron beam are reflected back toward the source. The detector is designed to produce an image only from electrons that travel in a straight path between the sample and the detector. A major benefit of using backscattered electrons is the obtained images have high contrast despite having a lower lateral resolution (approximately 1 $\mu$m) [89].

## 3.2 Surface Analysis Experiments and Procedures

This section details the procedures, techniques, and metrics used to analyze the surface morphology of printed electrodes, Zn foil, and dried gel polymer electrolyte as well as the interactions of the layers and materials with each other. The procedures used in these investigations included dispenser printing, stencil casting, confocal optical microscopy, contact angle measurements, scanning electron microscopy, and cell cycling.

### 3.2.1 $MnO_2$ Electrode Ink Production and Preparation

The creation of custom $MnO_2$ inks was necessary because no standard printed $MnO_2$ electrode existed when this research was conducted. Based off the work by Ho *et al.*, the inks were composed of $MnO_2$, acetylene black (AB), and PVDF-HFP as described in Table 3.1. The $MnO_2$ is the active electrochemical component that was expected to allow zinc to intercalate into its crystal lattice. The small amount of AB was added to improve electrical conductivity in the electrodes [34]. The polymer PVDF-HFP was included to provide structural support for the powders and to tune the rheology to the desired range and ensure manufacturability. NMP was chosen as the solvent because it readily dissolved PVDF-HFP and allowed for further fine tuning of the ink rheology. Both the $MnO_2$ electrode and gel polymer electrolyte used PVDF-HFP as their binder, thus ink compositions were created to characterize the surface wetting and interactions based on both surface morphology and amount of binder present. Composition A maintained a low mass percentage of polymer consistent with compositions found in the literature and as recommended by material suppliers [33, 23, 27, 59]. Composition B had 7.5 times more polymer and a similar amount of $MnO_2$ to AB to provide an extreme case to compare composition A against.

In order to add PVDF-HFP to each ink, a gel was added that was composed of PVDF-HFP and NMP. The gel was created by adding 1 part by mass (pbm) of PVDF-HFP (Arkema) into 5 pbm of NMP (Alfa Aesar, ACS grade, 99.0+%). To dissolve the PVDF-HFP, it was added to the NMP then placed in the sonicator with the heater on for at least 2 hours until fully dissolved.

Table 3.1: Solid material ratios for $MnO_2$ electrode compositions. NMP was added to achieve the desired rheology for printing.

| | **Composition A** | **Composition B** |
|---|---|---|
| **Material** | **Mass %** | **Mass %** |
| $MnO_2$ | 90% | 66% |
| AB | 6% | 4% |
| PVDF-HFP | 4% | 30% |

Table 3.2: Masses of material used to create $MnO_2$ electrode inks for each composition.

| | **Composition A** | **Composition B** |
|---|---|---|
| **Material** | **Mass (g)** | **Mass (g)** |
| $MnO_2$ | 3.6 | 2.6 |
| AB | 0.24 | 0.16 |
| PVDF-HFP | 0.16 | 1.2 |
| NMP | 2.9 | 6 |

The solid, dry $MnO_2$ and AB powders were weighed and mixed together in a separate bottle with a vortex mixer (Fischer Scientific, Digital Vortex Mixer 120V) before being added to the desired mass of gel. After being added to the gel, additional NMP was pipetted into the mixture in 0.25-0.50 g increments until the desired rheology was obtained. After each pipette of material, the components were mixed on the vortex mixer for 30-60 s.

Upon completion, the final mixture was placed on the vortex mixer for 3 minutes at 2500 rpm. The ink was then placed in the sonicator for 30 minutes with the heat on. Finally, the bottle was placed in a ball mill (Across International, PQ-N04) for mixing. Ball mills use a planetary gear system to spin steel or ceramic jars that contain a slurry of coarse material, a solvent, and grinding balls. The jars are placed on the planet gears and spun at a high rate of speed. The grinding balls within the jars impact and pulverize the coarse material to produce a finer powder. While commonly used for materials processing, the mill was used in this research to thoroughly mix each ink. The ball mill was run at 30 Hz for 1 hr, where the direction of rotation would reverse every 15 minutes to sufficiently mix each ink.

### 3.2.2 Dispenser Printing

A custom dispenser printer was utilized to produce thick-film electrodes on various surfaces. A 23 TW gauge (0.635 mm outer diameter, 0.432 mm inner diameter) syringe tip was filled with the desired functional ink and connected to a 5 cubic centimeter, luer lock syringe. The syringe assembly was then inserted into a housing connected to a Z-axis stage. A hose with a screw lock was finally connected to the top of the assembly to allow for air to be injected

into the syringe body to dispense the functional ink. A pressure controller (Musashi ML-808 FX) was used to dispense metered amounts of compressed air to produce pixels of ink onto the desired surface. The source was house air that was filtered for water and particulates before entering the controller. An X- and Y-axis stage was used to mount the substrate and to translate it to produce various printed geometries. This stage had two pairs of holes milled into it that were connected to a vacuum pump to ensure the substrate would not move during printing. Custom software developed in Java with the Netbeans IDE was used to control the stages and dispenser controller. This software was used to dispense inks onto the substrates to produce squares for testing and analysis.

### 3.2.3 Stencil Casting

In order to produce 1 $cm^2$ electrodes with a consistent morphology, stencil casting was used. The stencil was produced by using a laser cutter (Universal Laser Systems VLS3.50) to cut 1 $cm^2$ squares in a 2-by-4 array in 150 $\mu$m-thick polyethylene terephthalate (PET) film. The squares were spaced 1 cm apart on each side to ensure separation of the printed areas in the event of ink bleed as a result of capillary forces in the small cavity between the stencil and the substrate. The substrate chosen for the electrodes was 50.8 $\mu$m-thick stainless steel foil because of its electrical conductivity and structural stability required for constant handling at the research scale.

A 25 $cm^2$ glass mirror was used as a casting surface because it provided a small, easy to handle, flat surface. The mirror, substrate, and stencil were cleaned with acetone and wiped down with Kimwipes to ensure good contact and a smooth casting surface. After cleaning the substrate was placed on the mirror and taped along the top end where casting would begin. The stencil was then placed on top of the substrate and taped also at the top end. A small amount of acetone was added between the stencil and the substrate and wiped down with a Kimwipe to distribute the fluid under the entire stencil. This generated an adhesion force between the stencil and substrate to improve casting quality and edge fidelity.

Small amounts of the ink to be cast were placed at the top of each square with a wood applicator stick (Puritan). A glass slide was then slowly drawn down the stencil while being held at a small acute angle relative to the direction of casting.

Upon completion, a pair of tweezers were used to carefully peel the stencil off the substrate. The resulting cast was then placed in an oven for at least 2 hours to evaporate all of the solvent. The stencil and mirror were then cleaned with acetone for future reuse.

### 3.2.4 Laser Confocal Microscopy

An Olympus LEXT OLS3000 3D Laser Confocal Microscope was used to image and measure the height of a subsection of the surface of printed electrodes and electrolytes. Note that the calibration table for the microscope presented in Appendix A. Each surface was scanned using the fast scanning mode. To obtain a single, 1789 $\mu$m-square image, 9 images each 643 $\mu$m-square, were taken and stitched together with 10% overlap within the software

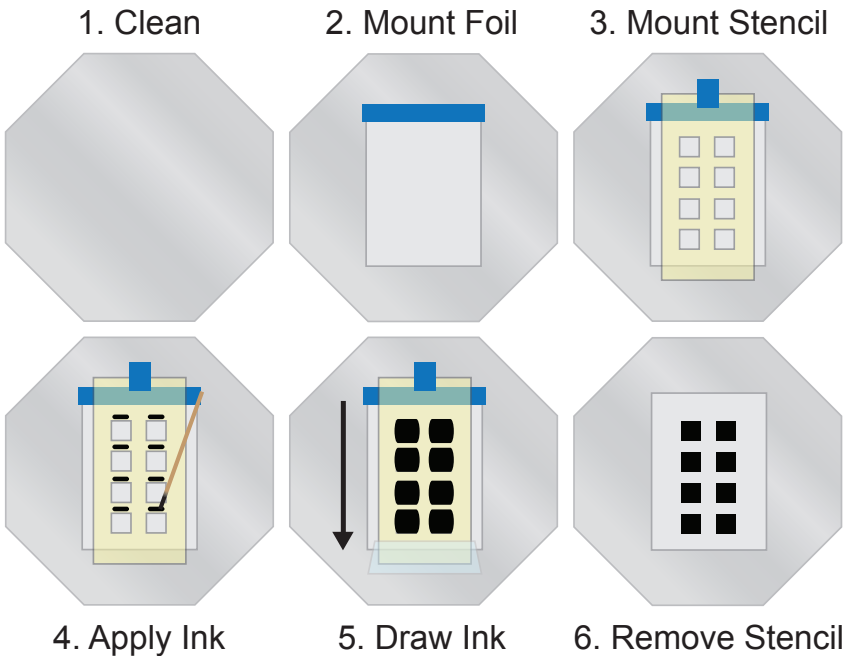


Figure 3.5: Stencil casting process.

automatically after acquisition. After obtaining the data, the resulting image was leveled with the built-in quick level function in the Olympus LEXT software. The height map was then exported to a comma separated value (CSV) file for analysis with custom software.

The resulting height map, called the primary profile, included both high and low wavelength features, called the roughness and waviness respectively. To conduct analyses of the surface and separate out these different features, an FFT was applied to each row of data of the primary profile. This produced a spectrum of sine waves with different wavelengths and amplitudes that represented each row of data. This was then used to parse the low wavelengths that represented the waviness profile and to then convert them from frequency and amplitude data to position and height data by using an IFFT.

To parse those low wavelengths, a low-pass filter was implemented and applied to the FFT data. As per the standard from the American Society of Mechanical Engineers (Standard B46.1-2009), an 80 $\mu$m cutoff wavelength was used for the low-pass filter. Thus all waveforms with a wavelength higher than 80 $\mu$m were unmodified and the rest were set to zero to remove their contribution. The transfer function for a low-pass filter is described by

$$H(s) = \frac{f_s/\lambda_c}{s + f_s/\lambda_c} = \frac{1}{1 + s\lambda_c/f_s} \tag{3.13}$$

where $s$ is the value at a point, $\lambda_c$ is the cutoff wavelength, and $f_s$ is the sampling frequency [40].

When the IFFT was applied to the subset of wavelengths that represented the waviness, the returned profile had a value of zero at the origin and half the magnitude. The zero origin was because the FFT used sine waves as a representative waveform and the profile is not an infinite, continuous function. The half magnitude was because the FFT produced a symmetric map of wavelengths for exclusively real-numbered data. Only the first section of that data was used in the IFFT, thus half of the magnitude was left out. To fix the magnitude, the IFFT result was simply multiplied by a factor of two. To move the origin from zero back to that of the primary profile, an extended primary profile was used.

This extended primary profile was produced by using the original primary profile as the center of a mirror repeating pattern. If L represented the left edge and R represented the right edge of the original primary profile, then the extended primary profile was RLLRRL. This ensured congruency with the features at the edges and that the correct waviness profile had no zero origin. After performing an FFT, low-pass filter, and IFFT on this extended primary profile, the center of the pattern was extracted as the correct waviness profile. Figure 3.6 shows these steps with a cross-section of a primary profile of a stencil-printed electrode with ink composition A.

The roughness profile was calculated by subtracting the waviness profile from the primary profile.

The arithmetic average ($R_a$, $W_a$) and root mean square ($R_q$, $W_q$) were calculated over the full, 2-D roughness and waviness profiles, R and W respectively, associated with surface produced by each manufacturing method. The equations for each are as follows,

$$R_a, W_a = \frac{1}{MN} \sum_{j=1}^{N} \sum_{i=1}^{M} |\eta(x_i, y_j)| \tag{3.14}$$

$$R_q, W_q = \sqrt{\frac{1}{MN} \sum_{j=1}^{N} \sum_{i=1}^{M} \eta^2(x_i, y_j)} \tag{3.15}$$

where $\eta$ represents the matrix of surface heights, $x_i$ and $y_j$ represent the indices for values in the matrix of height data, and $M$ and $N$ represent the number of rows and columns of the matrix.

### 3.2.5 Scanning Electron Microscopy

A scanning electron microscope (SEM) (Hitachi TM-1000) was used to image surfaces and cross-sectional edge views of the printed components. It is important to note that the system uses back-scattered and secondary electrons to produce images, thus the surface to be investigated must be able to sufficiently reflect electrons.

For viewing the top surface, the sample was mounted on a flat holder with carbon tape. For viewing edges, the sample was cut with a pair of scissors, then mounted with the edge facing upward on a right angle holder with carbon tape. After mounting the sample on

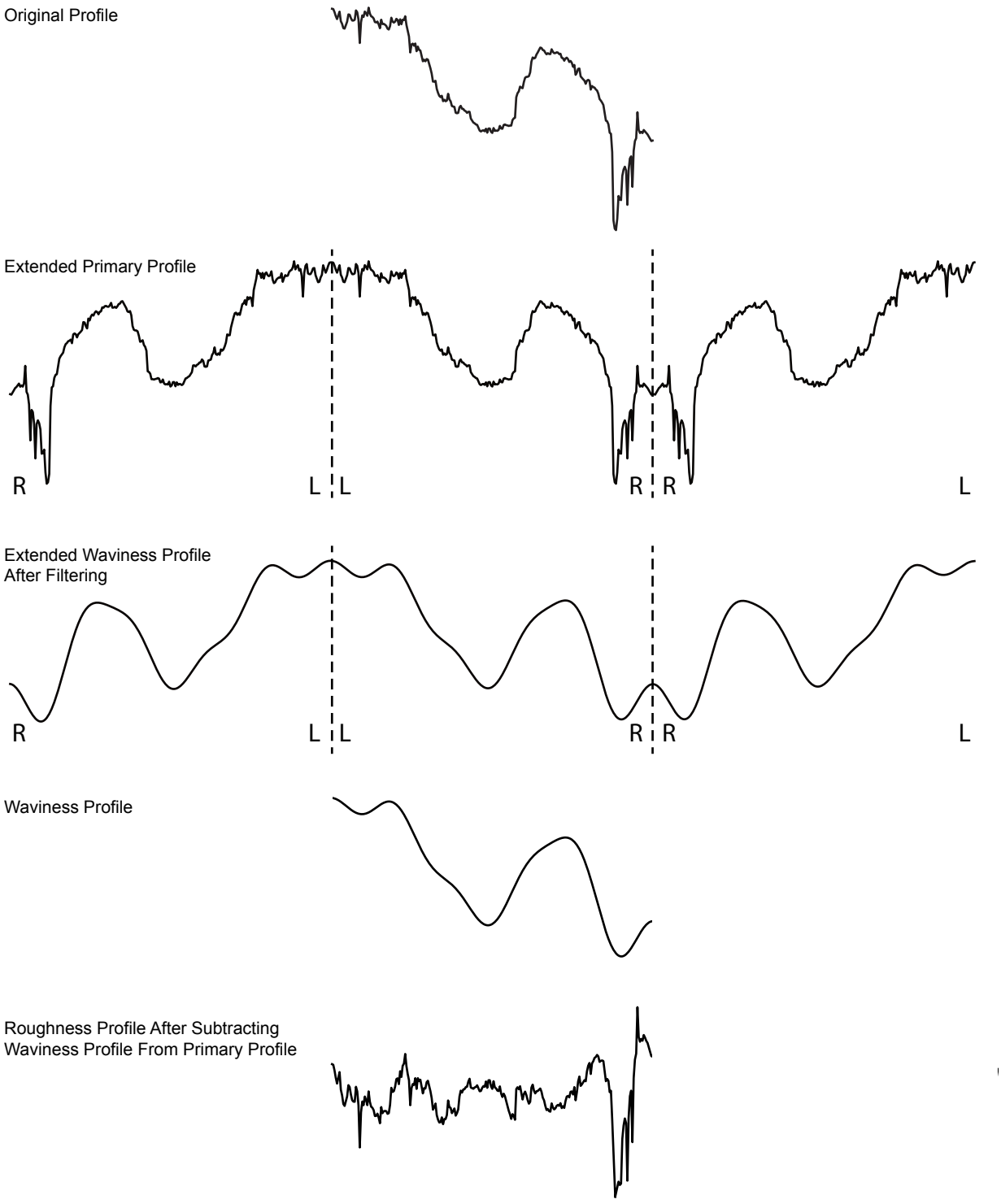


Figure 3.6: Process to acquire correct waviness profile and roughness profile from a primary profile by utilizing a mirror repeating pattern.

the holder, the sample was placed on the screw stem and the height was adjusted on the clearance guide. Finally, the full assembly was inserted into the SEM to be analyzed.

### 3.2.6 Contact Angle Measurements

To measure the interaction between the printed and non-printed surfaces in relation to the gel polymer electrolyte, the contact angle between the materials was measured via the sessile drop method. The dispenser printer was utilized to produce controlled droplets for testing. A 23 TW gauge (0.635 mm outer diameter, 0.432 mm inner diameter) syringe tip was used to produce droplets approximately 0.095 to 0.125 mm in diameter, or 1.5 to 2 times the outer diameter of the tip.

After producing a droplet of sufficient size at the end of the tip, it was brought into contact with the target surface. The tip was then retracted, leaving the droplet on the target surface. The droplet was allowed to settle for approximately 10 seconds to an equilibrium before an image was captured for analysis. Because the morphology of the printed electrodes was variable over the area, the contact angles at both the left and right edges of the droplet were measured. The software ImageJ64 was used to measure the angle between the droplet and target surface. The average value of those results was then calculated to represent the interaction between the electrolyte and target surface.

### 3.2.7 Cell Manufacturing

Coin cells were assembled by placing a printed, 1 $cm^2$ square $MnO_2$ electrode in the center of the CR2032 form factor stainless steel can. Several drops of electrolyte were pipetted onto the $MnO_2$ electrode to fully wet the surface. A 19 mm diameter separator (Freudenberg Nonwovens, FS22430-06LF, polyolefin) was cut and placed on top of the wet $MnO_2$ electrode to electrically insulate it from the counter electrode and prevent shorting. Several more drops of electrolyte were pipetted onto the separator to fully wet the surface. The counter electrode was 50 $\mu$m thick, 99.95+% pure zinc (Zn) foil (Goodfellow, 307-980-18) cut to 1 $cm^2$ square. This was placed in the center on top of the wetted separator. Two 15.8 mm diameter, stainless steel spacers (MTI Corp, EQ-CR20-Spacer304-05) and two 15.8 mm diameter spring (MTI Corp, Belleville washer, EQ-CR20BW-Spring304) were stacked on top of the Zn foil. A CR2032 lid (MTI Corp, EQ-CR2032-CASE) with insulating ring already attached was then set on top of the final stack inside of the can. The assembly was placed in a coin cell crimper (BTInnovations) and sealed shut. The open circuit voltage (OCV) of the completed cell was checked to ensure there was no short.

To assemble a dry stack cell, a 1.2 $cm^2$, 10 $\mu$m thick, dispenser-printed GPE was picked and placed onto a 1 $cm^2$ $MnO_2$ electrode. A 1 $cm^2$ zinc foil counter electrode was then placed on top of the wetted GPE to complete the cell.

To assemble a wet stack cell, two drops of electrolyte were pipetted onto a printed 1 $cm^2$ $MnO_2$ electrode. A 1.2 $cm^2$, 10 $\mu$m thick, dispenser-printed GPE was then picked and placed onto the electrode to completely cover it. Two more drops of electrolyte were then pipetted

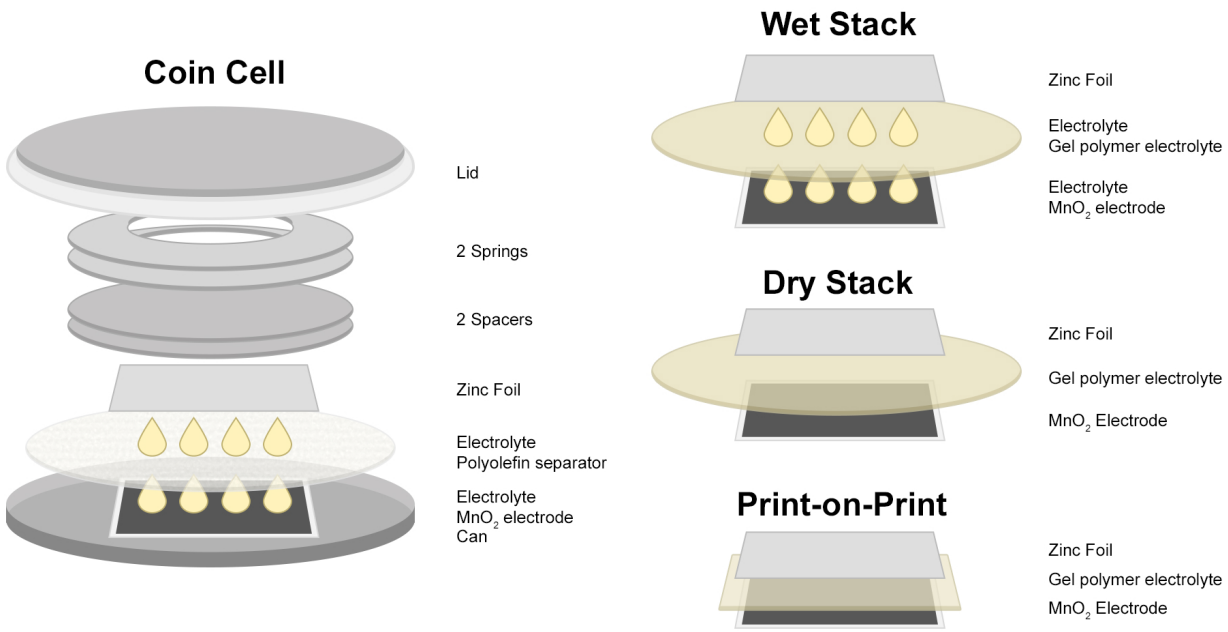


Figure 3.7: Exploded view of each assembly method and cell form factor.

onto the GPE layer. A 1 $cm^2$ zinc foil counter electrode was then placed on top of the GPE to complete the cell.

A print-on-print stack cell was assembled by dispenser printing a 1 $cm^2$ $MnO_2$ electrode that was then dried for at least 3 hours at 80 °C in the oven. Then a 1.2 $cm^2$ GPE was dispenser-printed onto the cathode then dried for at least 3 hours at 80 °C in the oven. A 1 $cm^2$ zinc foil counter electrode was then placed on top of the GPE to complete the cell.

## 3.3 Results and Discussion

### 3.3.1 Printed Electrode Composition

SEM images were obtained for electrodes with composition A, as shown in Figure 3.8, to determine the distribution of active material within the printed cathode and the overall quality of the surfaces produced. The images show how the polymer caused the build up of large, spherulite-like structures between 10 and 100 $\mu$m in diameter [38].

For composition A, cracks on the order of 10 $\mu$m wide and 50 to 100 $\mu$m long were present. Voids were also visible for the dispenser-printed electrodes with feature sizes between 10 to 50 $\mu$m wide. These features tended to form both superficially and within the electrode itself, as shown in Figure 3.8. Despite this the cross-sectional edge views for both the stencil and dispenser-printed electrodes showed a high degree of particle packing, thus providing conduction pathways through the electrode to the current collector. The low fraction of

polymer in the ink composition ensured particle contact without fully coating the functional material. Although the electrodes exhibited these beneficial qualities, they were very brittle and were unable to withstand the bending of the substrate or other perturbations.

While composition B does show good particle packing, a layer of the PVDF-HFP coated the majority of the top surface of the electrodes, as visible in Figure 3.8. The polymer was also found to have infiltrated into the electrodes, thus creating regions with low conductivity within the structure. This is even more pronounced in the stencil-printed electrode where the polymer has mixed almost completely through the layer. This coating likely arose because the density of PVDF-HFP (0.288 g/cm$^3$) was lower than that of the $MnO_2$ (5.03 g/cm$^3$) or AB (1.95 g/cm$^3$). Some settling may also have occurred where the rheology of the solution was not strong enough to continually suspend the large solid particles throughout drying. While the presence of this film was not ideal for electrochemical conduction, it is possible that it could provide an improvement in the wetting of the GPE on the electrode surface because they both contain the same polymer.

Voids similarly ranged between 10 $\mu$m and 50 $\mu$m wide in the dispenser-printed electrode made from composition B. Unlike the dispenser-printed electrode made from composition A, this had no visible cracks. This was attributed to the much higher amount of polymer in the ink. The additional binder caused the electrodes to be more mechanically robust and they could be flexed without breaking.

As noted previously, the addition of excess polymer to the ink composition did increase the mechanical strength of the films and reduced the number of cracks and voids. However this boon to manufacturability may have caused passivation of large areas of the electrode by fully coating the functional material, thus reducing conductivity to a non-functional range. This was confirmed when full cells were made, as will be discussed in Section 3.3.4.

### 3.3.2 Surface Morphology Characterization

The primary profiles shown in Figure 3.9 elucidate the differences between the $MnO_2$ printed electrodes manufactured with compositions A and B via stencil and dispenser printing.

The stencil-printed $MnO_2$ electrodes for both compositions exhibited randomly distributed, sharp, well-defined valleys. Composition A contained valleys between 20 and 80 $\mu$m deep and peaks 40 to 80 $\mu$m tall across the electrode. Composition B contained valleys between 20 and 125 $\mu$m deep depending on location and peaks between 30 and 130 $\mu$m tall. The profiles also showed less packing and a wider distribution between the extreme features of the surface made with composition B.

Of the printed electrodes, the dispenser-printed composition A exhibited wide, shallow valleys between 20 and 60 $\mu$m deep and peaks 20 to 80 $\mu$m tall. It also had a row-like configuration associated with the raster method the dispenser printer used to deposit material. These features can be slightly seen as columns for the dispenser-printed composition B.

Comparing the printed electrodes with each other, composition A exhibited fewer extreme holes and steps in the surface while composition B had many. The dispenser-printed

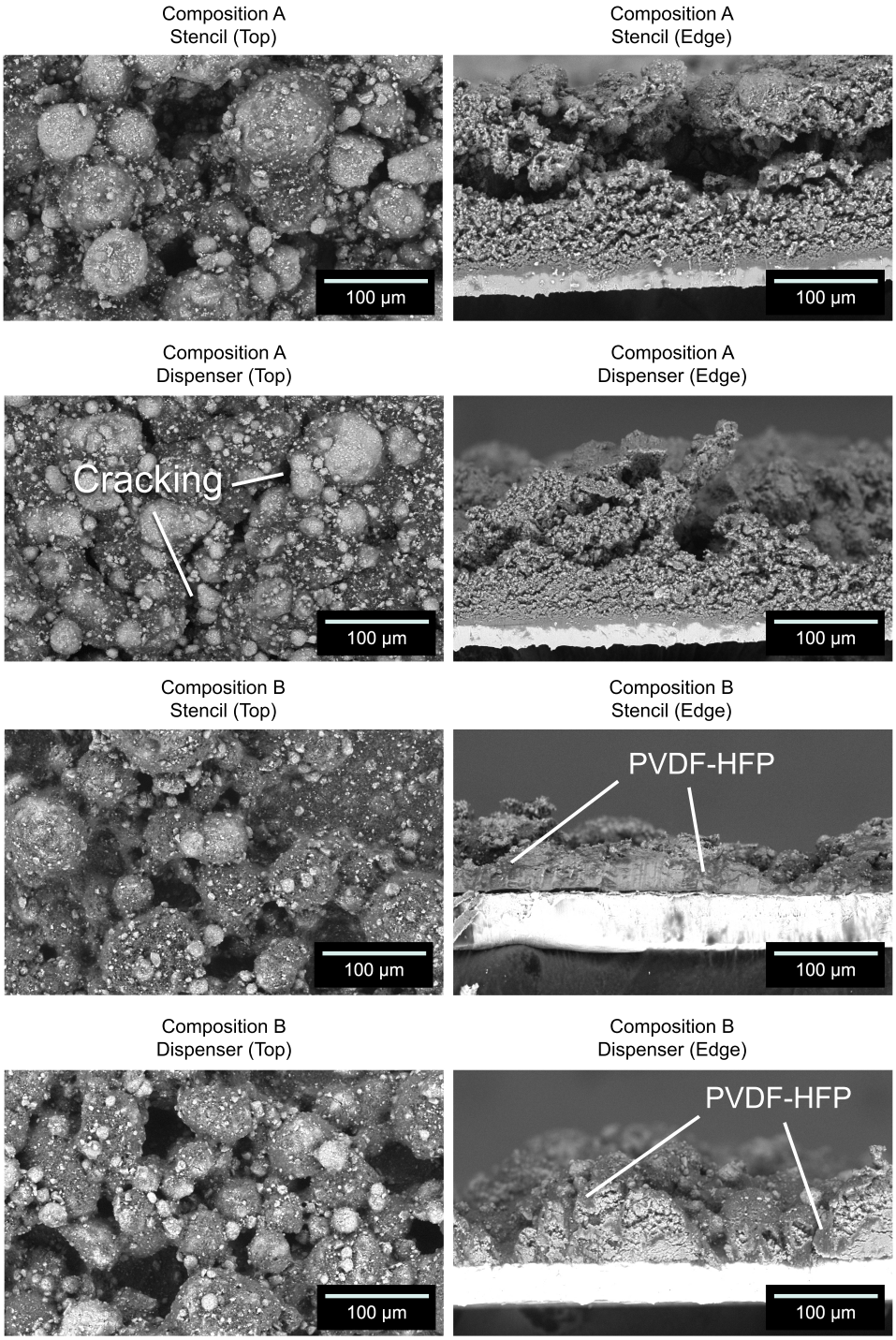


Figure 3.8: Top and edge views of stencil and dispenser-printed $MnO_2$ electrodes of composition A and B.

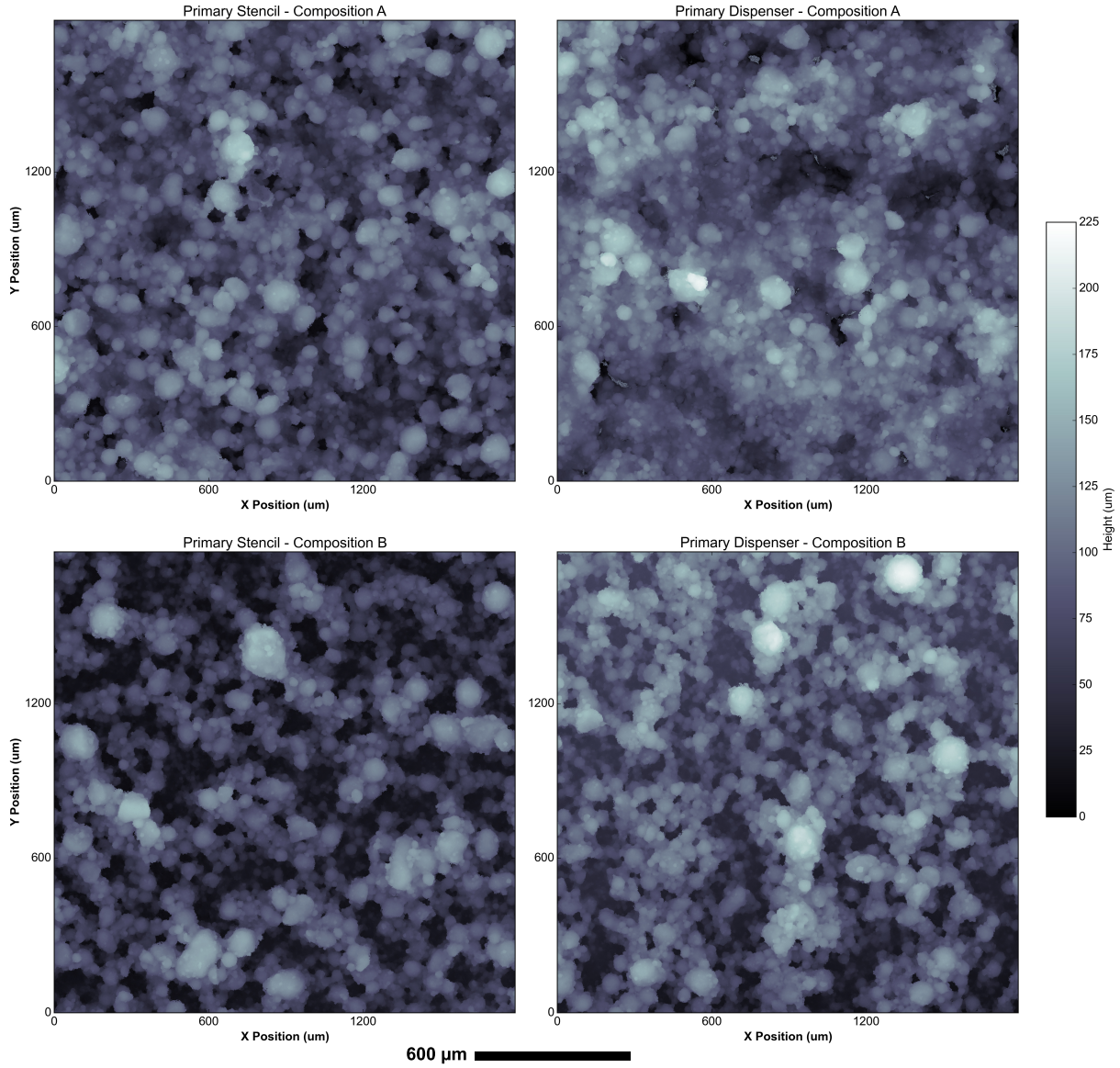


Figure 3.9: Primary surface profiles of stencil and dispenser-printed $MnO_2$ electrodes for compositions A and B.

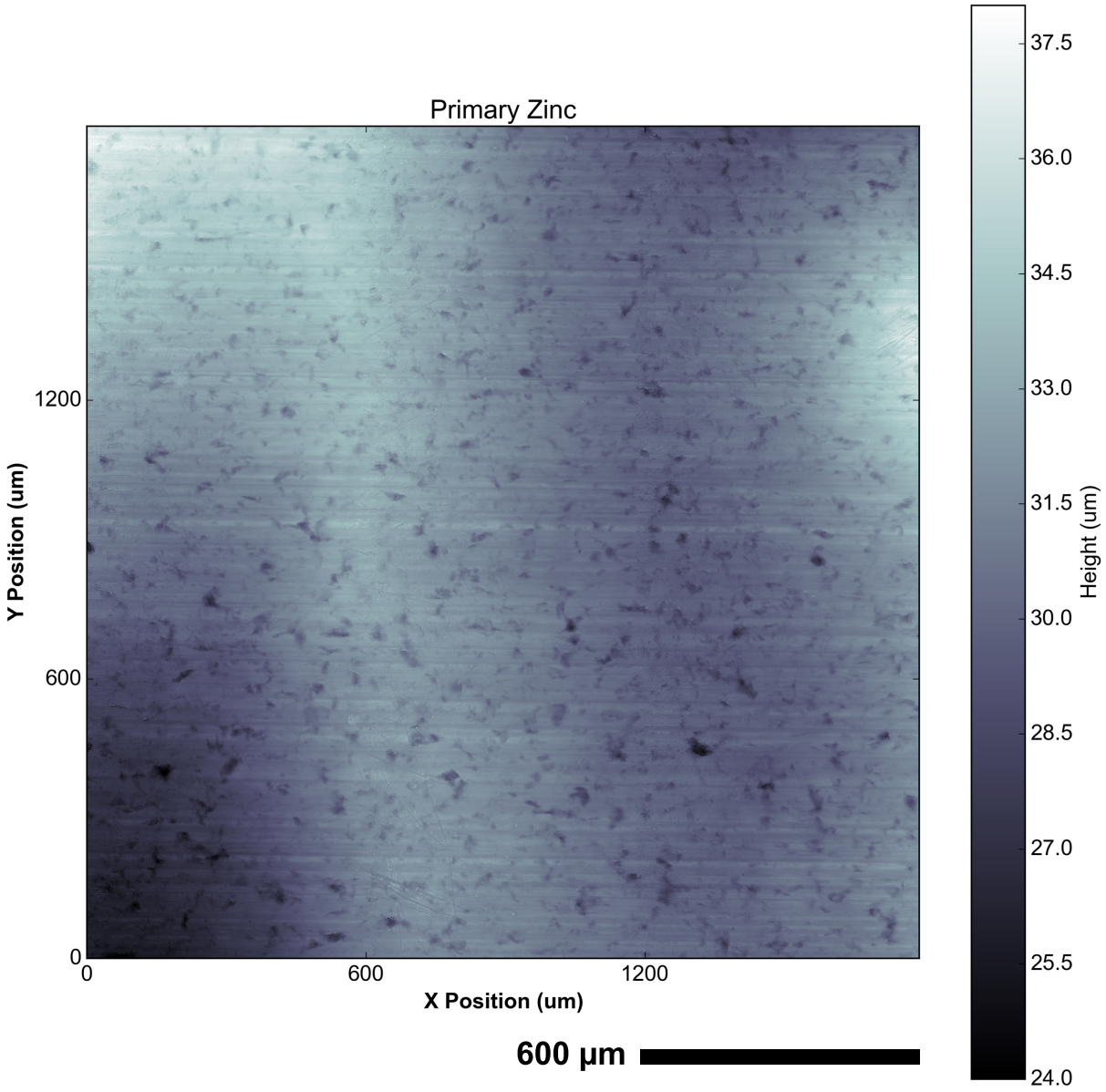


Figure 3.10: Primary surface profile of zinc foil to provide a reference against the stencil and dispenser-printed $MnO_2$ electrodes for compositions A and B. Note the change in scale relative to the other surface maps.

electrodes appeared to have a more regular distribution of particles than their stencil-printed counterparts.

Table 3.3: Arithmetic average and root mean square roughness ($R_a$, $R_q$) and waviness ($W_a$, $W_q$) of $MnO_2$ electrodes inline with the scanning direction with the microscope. Note that all units are in $\mu$m.

| | **Composition A** | | **Composition B** | | |
|---|---|---|---|---|---|
| | **Stencil** | **Dispenser** | **Stencil** | **Dispenser** | **Zinc Foil** |
| $R_a$ | 3.490 | 3.314 | 3.776 | 3.853 | 0.228 |
| $R_q$ | 5.396 | 5.406 | 5.511 | 5.610 | 0.320 |
| $W_a$ | 20.75 | 20.35 | 24.89 | 25.44 | 1.380 |
| $W_q$ | 26.24 | 25.97 | 30.59 | 30.94 | 1.707 |

Table 3.4: Arithmetic average and root mean square roughness ($R_a$, $R_q$) and waviness ($W_a$, $W_q$) of $MnO_2$ electrodes orthogonal to the scanning direction with the microscope. Note that all units are in $\mu$m.

| | **Composition A** | | **Composition B** | | |
|---|---|---|---|---|---|
| | **Stencil** | **Dispenser** | **Stencil** | **Dispenser** | **Zinc Foil** |
| $R_a$ | 3.501 | 3.119 | 3.698 | 4.213 | 0.310 |
| $R_q$ | 5.427 | 5.263 | 5.413 | 5.888 | 0.423 |
| $W_a$ | 20.79 | 21.58 | 25.726 | 25.217 | 1.248 |
| $W_q$ | 26.19 | 27.60 | 31.356 | 31.653 | 1.911 |

The metrics used to describe the surface subsections, as shown in Tables 3.3 and 3.4, showed that in all cases, except between $R_q$ for the stencil-printed electrodes in the orthogonal direction, the composition B electrodes were rougher and wavier than their composition A counterparts. Between manufacturing methods, though, there were no large discrepancies. The largest change was a 13.9% (0.515 $\mu$m) between the orthogonal $R_a$ values for the stencil and dispenser-printed composition B electrodes. Relative to the printed electrodes, the zinc foil exhibited very low roughness and waviness values, as expected for a metal foil. The slight changes in height in the foil were due to handling when placing it on the microscope because of the high malleability of zinc.

The average and RMS values, commonly used to quantify the surface features of materials, lacked the ability to take feature distribution into account. Despite this a visual inspection of the distribution of features may be important for determining the ability of successively printed layers to fully wet each electrode during and after printing, especially if air may be trapped within such features.

### 3.3.3 Contact Angle Measurements

A gel polymer electrolyte (GPE) with the composition 1:1:5 parts by mass (pbm) for [1:15 of $Zn(OTf)_2$:[BMIm][OTf]]:PVDF-HFP:NMP and the electrolyte 1:15 pbm of $Zn(OTf)_2$:[BMIm][OTf] were pipetted onto the electrodes to determine the resulting contact angles. Figure 3.11 shows the result for droplets of each electrolyte on the printed electrode surfaces.

As noted in Table 3.5, the contact angles of the GPE on the composition A printed electrodes from both stencil and dispenser printing were very similar to each other. The average of the stencil-printed contact angles was 25.28° and the average of the dispenser-printed contact angles was 23.40°, though. Here the distribution of features may have played a role with the improved wetting (associated with a smaller contact angle) on the dispenser-printed electrodes. The electrolyte with no PVDF-HFP attained effectively perfect wetting with a contact angle of 0° for both types of printed electrodes.

Table 3.6 shows the contact angles of the GPE on the composition B printed electrodes which, as noted previously, the contact angles were very similar between manufacturing methods. The average of the stencil-printed contact angles was 10.84° and the average of the dispenser-printed contact angles was 10.49°. On a per-sample basis, the dispenser-printed electrode had slightly improved wetting, though. The electrolyte with no PVDF-HFP attained effectively perfect wetting with a contact angle of 0° for both types of printed electrodes as with composition A.

Interestingly, the electrolyte and GPE in contact with the zinc foil exhibited the highest contact angles of all of the materials tested as shown in Tables 3.7 and 3.8. The electrolyte alone had a higher contact angle than the GPE indicating that, on zinc, problems with conductivity may arise if an insufficient amount of electrolyte is used in making full battery cells.

A comparison of all of the contact angle results shows that for the majority of cases, wetting of the electrolyte was dictated predominantly by material selection and composition other than by surface morphology. It was hypothesized that like materials would wet each other well. For example, a droplet of gel solution composed of PVDF-HFP was expected to wet a PVDF-HFP film well because they both contain the same polymer. This result was confirmed for composition B, which had a greater fraction of PVDF-HFP than composition A.

Conversely, the surface morphology did have a very large influence on the retention of air at the interfaces between the GPE and the printed electrodes, as shown in Figure 3.12. The high quantity of bubbles was indicative of this. An investigation of Figure 3.12 shows that the images with the most bubbles corresponded to the surfaces with the greatest distribution of tall peaks with deep trenches or holes, which were the stencil-printed composition A, stencil-printed composition B, and dispenser-printed composition B electrodes. The zinc, which had the highest contact angles and smoothest and flattest surface and was tested with the same material, conversely had no bubbles at all. Note that the bright spots in the zinc image were from a ring of LEDs for overhead illumination.

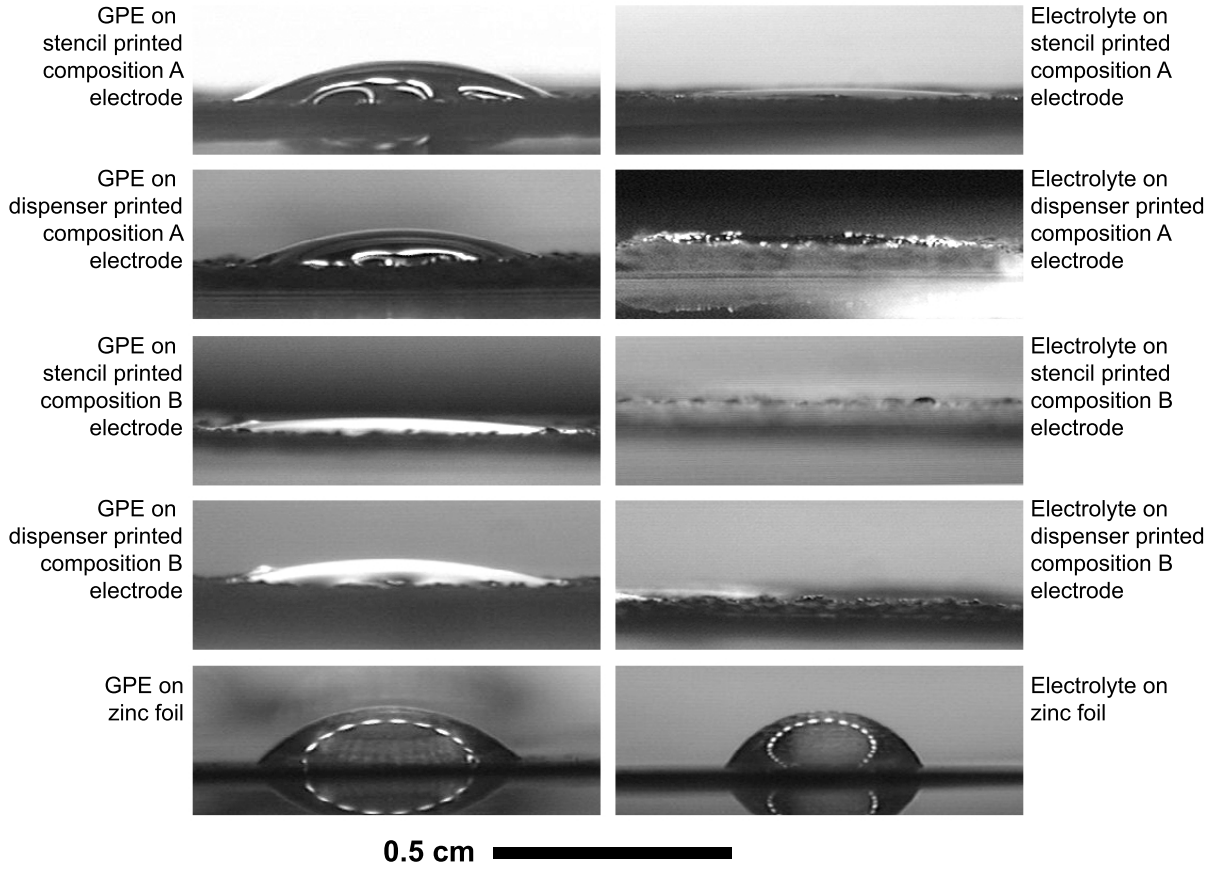


Figure 3.11: Droplets of gel polymer electrolyte (GPE) and electrolyte on each printed electrode and on zinc foil.

Table 3.5: Contact angle of gel polymer electrolyte (GPE) on printed $MnO_2$ electrodes with composition A. Measurement error = $\pm 2°$

| | **Composition A** | | | | | |
|---|---|---|---|---|---|---|
| | **Stencil** | | | **Dispenser** | | |
| | **Left** | **Right** | **Average** | **Left** | **Right** | **Average** |
| 1 | 24.59° | 24.31° | 24.45° | 24.47° | 22.66° | 23.57° |
| 2 | 25.00° | 21.52° | 23.26° | 22.75° | 20.19° | 21.47° |
| 3 | 26.39° | 29.89° | 28.14° | 25.82° | 24.52° | 25.17° |

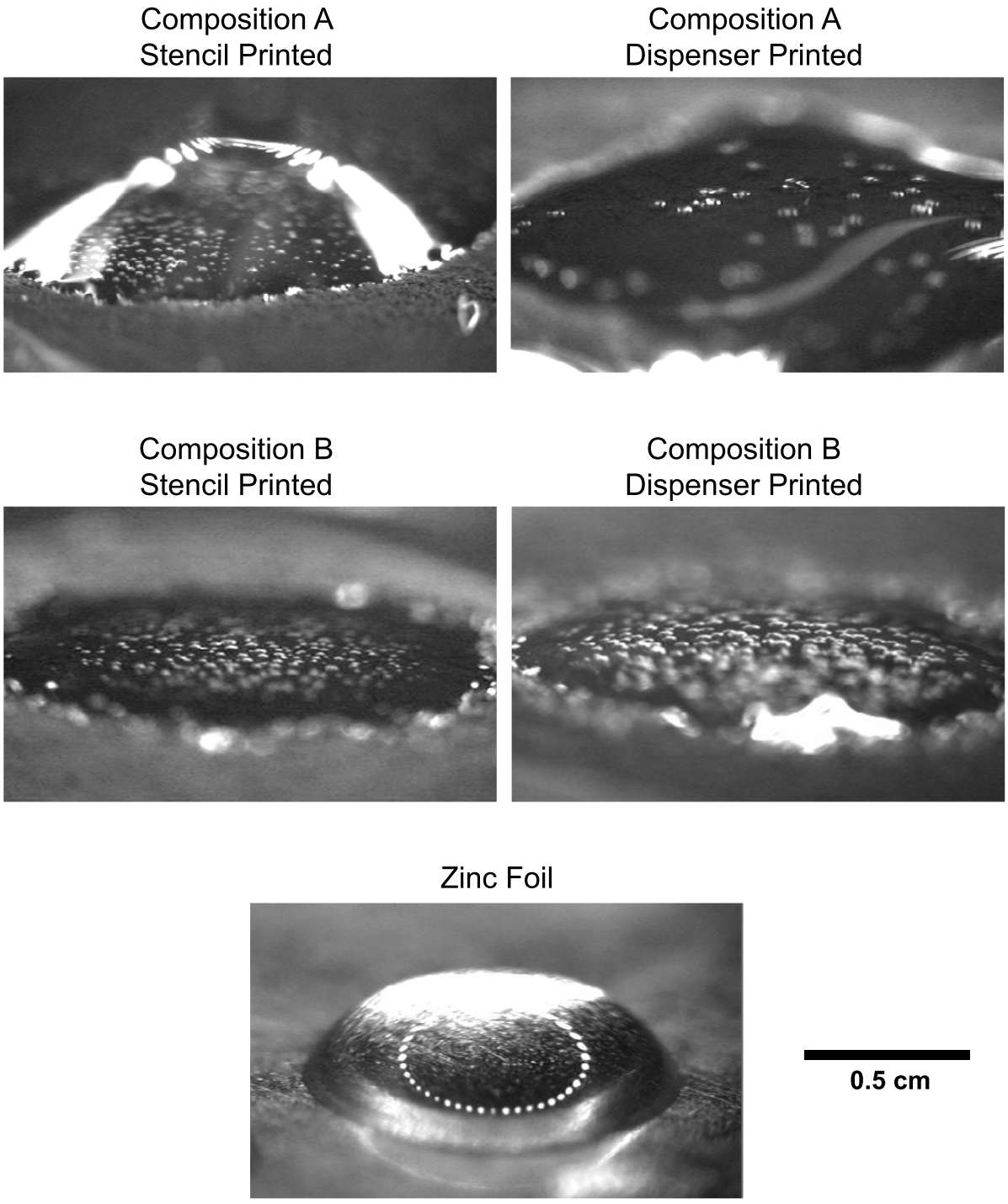


Figure 3.12: Droplets of gel polymer electrolyte (GPE) on zinc foil with no bubbles, and stencil and dispenser-printed electrodes of compositions A and B with air trapped at the interface.

Table 3.6: Contact angle of gel polymer electrolyte (GPE) on printed $MnO_2$ electrodes with composition B. Measurement error = ±2°

| | **Composition B** | | | | | |
|---|---|---|---|---|---|---|
| | **Stencil** | | | **Dispenser** | | |
| | **Left** | **Right** | **Average** | **Left** | **Right** | **Average** |
| 1 | 10.61° | 11.90° | 11.26° | 12.01° | 9.900° | 10.96° |
| 2 | 12.75° | 9.440° | 11.09° | 11.30° | 10.65° | 10.98° |
| 3 | 10.24° | 10.11° | 10.18° | 10.11° | 8.980° | 9.545° |

Table 3.7: Contact angle of gel polymer electrolyte (GPE) on zinc foil.

| | **Zinc Foil** | | |
|---|---|---|---|
| | **Left** | **Right** | **Average** |
| 1 | 39.47° | 45.05° | 42.45° |
| 2 | 39.11° | 37.53° | 38.32° |
| 3 | 46.74° | 42.50° | 44.62° |

Table 3.8: Contact angle of electrolyte without PVDF-HFP on zinc foil.

| | **Zinc Foil** | | |
|---|---|---|---|
| | **Left** | **Right** | **Average** |
| 1 | 56.43° | 60.79° | 58.61° |
| 2 | 66.30° | 61.86° | 64.08° |
| 3 | 56.82° | 54.73° | 55.78° |

### 3.3.4 Cell Performance

The assembly of dry stack cells with both composition A and B electrodes resulted in contact between only the peaks of the dry $MnO_2$ electrode surface and the GPE film. These cells produced an open circuit voltage (OCV) of approximately 1.2 V after assembly as measured with a handheld multimeter. They were placed on the battery cycler for testing, but were unable to be cycled. The cells produced no significant discharge capacity. The cycle discharge capacities were on the order of $2x10^{-3}$ mAh/cm$^2$, well below the capacity of any conventional battery. The voltage profile jumped immediately to 1.8 V or above upon starting the charging step and back down immediately to 1.0 V upon starting the discharging step. The high impedances at the interfaces between the electrode and GPE film were most likely the cause of the voltage spikes above and below the cycle conditions for fully charged and fully discharged respectively.

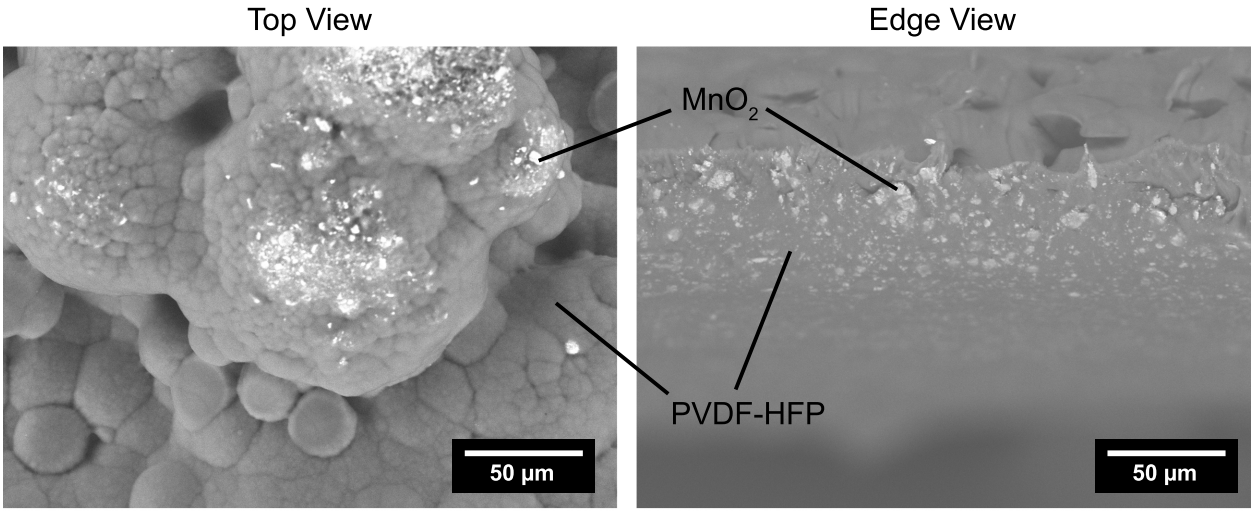


Figure 3.13: SEM images of top and edge views of a stencil-printed electrode with a layer of GPE printed on top, as noted in the print-on-print assembly method.

The discharge capacities for the print-on-print cells of both compositions were similar to the dry stack cells when cycling was attempted. Many cells could not provide an OCV in the expected 1.2 V range and sometimes produced no voltage at all. Figure 3.13 shows the electrode after printing the GPE on top. Both the electrode and GPE inks used PVDF-HFP as the binding polymer and NMP as the solvent. After printing the GPE, the NMP present in it saturated the electrode, thus causing it to become fluid once again. The two layers became highly mixed, coating the functional material with additional polymer and insulating the majority of the electrode.

The cells produced with composition A electrodes and wetted interfaces, both the wet stack and coin cells, were the only cells to cycle successfully. The cells made with composition B electrodes did not cycle because of the layer of polymer on the top surface, as hypothesized previously. An investigation of the respective current and voltage profiles for the functional composition A cells in Figure 3.14 shows how the coin cells and wet stack cell with stencil-printed $MnO_2$ electrode had smaller voltage jumps due to internal resistance when the cell began to charge than the wet stack cell with the dispenser-printed $MnO_2$ electrode. A lower jump was expected due to the use of the highly porous polyolefin separator instead of the semi-porous GPE film.

Figure 3.15 shows that the wet stack cells achieved higher discharge capacities for both electrode types than the coin cells. The wet stack cell with a dispenser-printed $MnO_2$ electrode attained a peak discharge capacity of 0.306 mAh/cm$^2$, then decayed to an average of approximately 0.175 mAh/cm$^2$ prior to failure after cycle 20. The wet stack cell with a stencil-printed $MnO_2$ electrode shows a similar improvement in discharge capacity over the first several cycles compared to the equivalent coin cell. It achieved a peak discharge

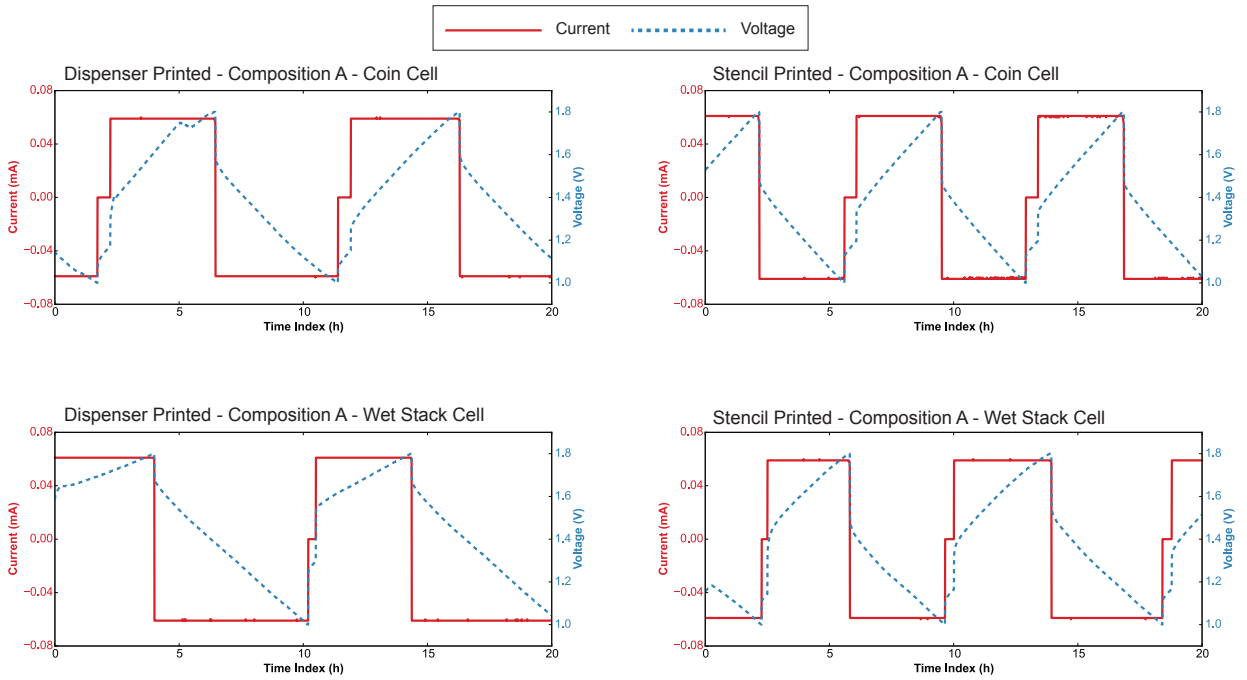


Figure 3.14: Current and voltage profiles over 20 hours of testing for the coin cell and wet stack cell types with dispenser-printed composition A electrodes.

capacity of 0.43 mAh/cm$^2$ for a single cycle before failing on cycle 8.

Conversely the coin cell with a stencil-printed $MnO_2$ electrode had a discharge capacity of 0.066 mAh/cm$^2$ for the first cycle, which then before decayed to 0.021 mAh/cm$^2$. Further cycling caused the discharge capacity to improve steadily back up to 0.054 mAh/cm$^2$. This varied dramatically from the coin cell with a dispenser-printed $MnO_2$ electrode. That cell had a discharge capacity approximately flat before failing soon after seeing a jump in discharge capacity to 0.203 mAh/cm$^2$. It also lasted only 15 cycles before failing.

## 3.4 Conclusions

This chapter investigated the manufacturing of and interactions between printed and non-printed electrodes composed of $MnO_2$, AB, and PVDF-HFP, and a gel polymer electrolyte composed of $Zn(OTf)_2$, [BMIm][OTf], PVDF-HFP, and NMP, along with the discharge capacity of the resulting cells through several optical, numerical, and electrochemical methods. Two printed electrode compositions were investigated, one with a low mass fraction of polymer and another with a high mass fraction of polymer. Cells made with each electrode composition were produced via either dispenser or stencil printing and assembled into a full cell with the GPE and zinc foil. Several different methods of producing cells were used to determine how changes in material contact affected the discharge capacity.

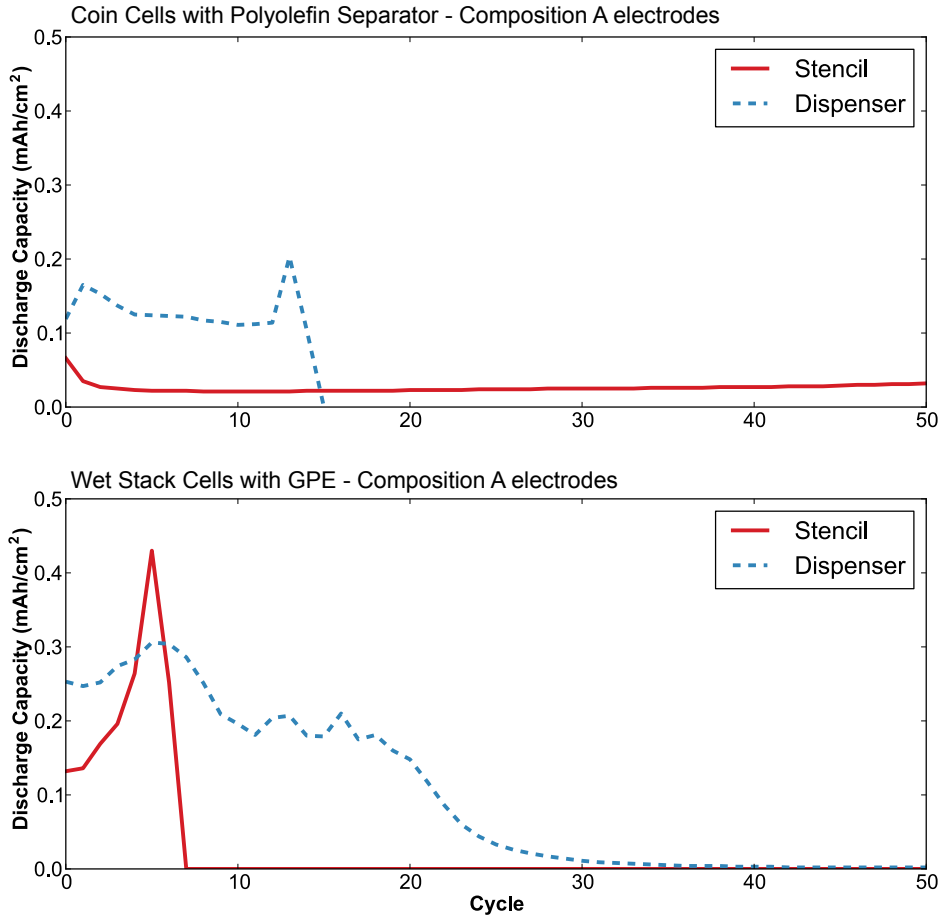


Figure 3.15: Comparison between discharge capacities for coin cells and wet stack cells assembled with stencil and dispenser-printed electrodes from composition A.

An investigation of all of the results indicates that it was not possible to create functional battery cells without having good contact between layers unless the surfaces were wet with the liquid electrolyte. This was because the voids were filled with electrolyte and virtually perfect wetting occurred, thus providing conduction pathways unavailable at a dry interface.

Not only did the roughness and waviness of the surfaces appear to have a very large influence on the formation of bubbles at the electrode-GPE interface, but the distribution of features on the electrode did as well. Additional research is required to determine adequate metrics that will take into account feature distribution of surfaces. For the functional cells produced here, the surface morphology did not appear to have a major influence on discharge capacity. A much larger subset of cells must be produced to acquire a statistically significant distribution to make any additional conclusions.

Additional research into alternative binding polymers must be conducted to rectify the mixing of the GPE with the printed electrodes. With printed electrodes and GPEs that have

low contact angles with each other and little to no mixing, cells can be produced where each successive layer can be printed on top of each other. Very thin GPE films will very quickly dry when heated in an oven. Despite the faster drying time, mixing between the layers may still occur at the interface.

# Chapter 4

# Electrolyte and Gel Polymer Composition

This chapter investigates the function, composition, and effects of several different compositions of a [BMIm][OTf]-based gel polymer electrolyte in order to improve cell discharge capacity and cell manufacturing yield. $Zn(OTf)_2$ salt was dissolved into the [BMIm][OTf] ionic liquid to form the electrolyte, which was then added to a solution with a mass ratio of 1:5 of PVDF-HFP:NMP to form the gel polymer electrolyte. Section 4.1 provides a brief overview of the fundamentals associated with copolymers, the main component that creates the gel polymer electrolyte. Section 4.2 describes the electrochemical methods used to conduct the analyses including electrochemical impedance spectroscopy and ionic conductivity. Section 4.3 discusses the methods used within this research including the design of experiments, gel polymer electrolyte manufacturing, quantification of gel drying time, and the existence of reduction-oxidation peaks indicating a functional electrolyte. Section 4.4 details and provides a discussion of the results obtained. Finally, Section 4.5 presents the conclusions obtained from the results of this chapter.

## 4.1 Materials Methods

This section overviews the basis for what a copolymer is and how they interact with solvents and other materials. The possible morphologies for copolymers are also discussed, as they provide the means to produce an ionically conductive, solid, gel polymer electrolyte.

### 4.1.1 Copolymers

A copolymer is made up of an ordered set of "mers" from different polymers. Such materials have been made in an attempt to combine beneficial properties from two materials or even discover new properties. Each mer type or unit is commonly represented by a letter, A and B for example, when describing the organization of mers within a given polymer chain. The


Figure 4.1: Alternating, statistical, periodic, block, and graft types of copolymers.

chains can have several types of organization, some of which are shown in Figure 4.1. An alternating copolymer switches between A and B mers at every junction, a statistical copolymer has a sequential distribution that obeys known statistical laws, a periodic copolymer has a regular sequence, a block copolymer has two long chains, or blocks, of each mer joined together at a junction, and a graft copolymer has chains comprised of one unit branch off a chain comprised of another unit [37].

The creation of these polymers is driven by "an unfavorable mixing enthalpy and a small mixing entropy" [49]. As a result, similar and dissimilar mers form covalent bonds with each other to create the copolymer chains. The final structure depends on the total degree of polymerization N ($= N_A + N_B$), the Flory-Huggins $\chi$-parameter, and the volume fractions of the constituent blocks ($f_A$ and $f_B$, $f_A = 1 - f_B$) [49]. The Flory-Huggins parameter is given by

$$\chi_{AB} = V_A(\delta_A - \delta_B)^2/RT \tag{4.1}$$

where $\chi_{AB}$ is the Flory-Huggins interaction parameter between the A and B blocks, $\delta_A$ and $\delta_B$ are the Hildebrand solubility parameters of the A and B blocks, $V_A$ as the volume fraction of the A block, $R$ is the gas constant, and $T$ is the temperature [49, 54]. The product of the the Flory-Huggins parameter and the degree of polymerization, $\chi N$, determines the degree of phase separation, as detailed in Table 4.1. Combining this product with the volume fraction of each mer type creates a phase diagram that determines what morphology will be obtained for the resulting polymer.

Table 4.1: Interaction regimes based on $\chi N$ product.

| Range | Regimes |
|---|---|
| $\chi N \leq 10$ | Weak-segregation limit (WSL) |
| $10 < \chi N \leq 50$ | Intermediate segregation region (ISR) |
| $50 < \chi N$ | Strong segregation limit (SSL) |

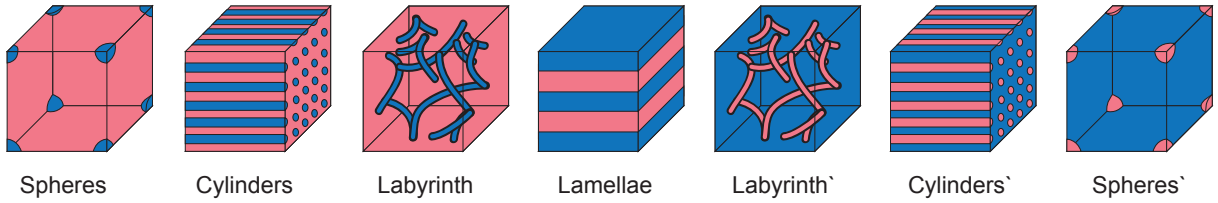


Figure 4.2: Set of possible morphologies for diblock copolymers.

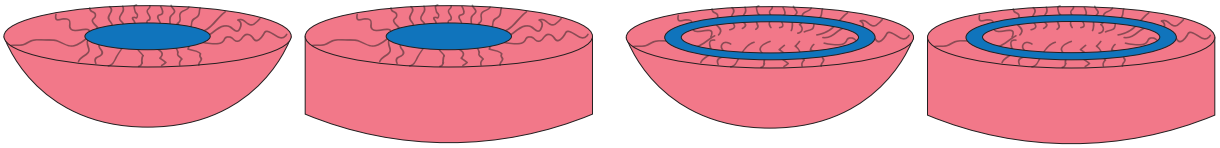

Figure 4.3: Possible morphologies for diblock copolymers that form micelles.

It is important to note that diblock copolymers, or block copolymers composed of two mer types A and B, have the ability to form micelles, or shells with different amounts of packing, as noted in Figure 4.3. These structures create volumes for other material to fill, specifically the electrolyte investigated in this research.

## 4.2 Electrochemical Methods

This section briefly covers the basis of electrochemical impedance spectroscopy and what aspects of battery components can be understood by using such a method. It also discusses the fundamentals and acquisition of the ionic conductivity of electrolytes.

### 4.2.1 Electrochemical Impedance Spectroscopy

No known electrochemical system is ideal. Each has attributes that impede the flow of current that can be qualified as resistive, capacitive, and inductive. The contributions of each of these components make up the impedance of an electrochemical system.

Electrochemical impedance spectroscopy (EIS) is a method of determining the impedance of a subject, be it an electrochemical cell or electrochemical component, at a set of predefined frequencies. It is a non-destructive method and can provide insight into the state and function of a cell and its components. The experiment applies an input voltage in the time domain to the subject that in turn produces an AC current response that can be analyzed as a sum of sinusoidal functions, also known as a Fourier series. [63, 25].

For a given electrochemical system of inspection, an input signal can be represented by

$$E_t = E_0 sin(\omega t) \tag{4.2}$$

where $E_t$ is the potential at time $t$, $E_0$ is the amplitude of the signal, and $\omega$ is the radial frequency that can be described by $\omega = 2\pi f$. The input signal is typically small, usually from -10 mV to 10 mV, in order to produce a response that is pseudo-linear such that it has the same frequency and is only shifted in phase such that the current response signal can be described by

$$I_t = I_0 sin(\omega t + \phi) \tag{4.3}$$

where, for a linear system, $I_t$ is the response signal, $I_0$ is the amplitude, and $\phi$ is the phase shift. To determine the impedance, the equation analogous to Ohm's Law for impedance is described by

$$Z = \frac{E_t}{I_t} = \frac{E_0 sin(\omega t)}{I_0 sin(\omega t + \phi)} = Z_0 \frac{sin(\omega t)}{sin(\omega t + \phi)} \tag{4.4}$$

where $Z_0$ is the magnitude of the impedance and the phase is $\phi$ [25].

Using Euler's relationship, where $e^{j\phi} = cos(\phi) + jsin(\phi)$, the impedance can be expressed as a complex function represented by:

$$Z(\omega) = \frac{E}{I} = Z_0 e^{j\phi} = Z_0(cos(\phi) + jsin(\phi)) \tag{4.5}$$

Thus $Z_0$ can be determined from the Lissajous plot by

$$|Z_0| = \frac{\Delta E}{\Delta I} = \frac{OA}{OB} = \frac{\Delta Y}{\Delta X} \tag{4.6}$$

and the phase angle can be similarly determined from the Lissajous plot by

$$\phi = sin^{-1}(-\frac{OD}{OA}) \tag{4.7}$$

where the lengths are defined as shown in Figure 4.5 [63].

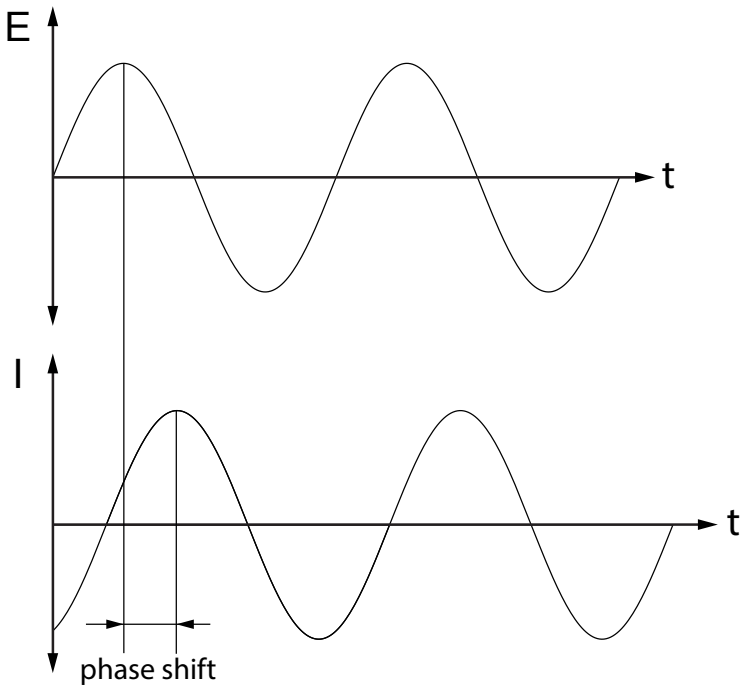


Figure 4.4: Input voltage signal and current response for an electrochemical system.

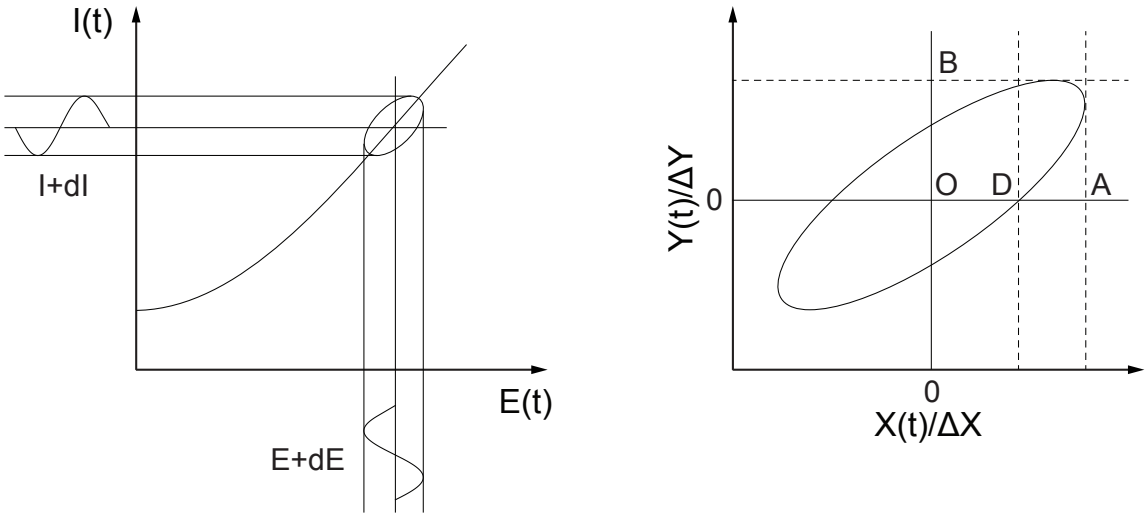


Figure 4.5: Origin and analysis of Lissajous Figure.

### 4.2.2 Ionic Conductivity

We can define a relationship for the ionic conductivity of classical electrolytes, that is electrolytes commonly composed of a salt dissolved in water, by beginning with Fick's Second Law of Diffusion given by

$$\frac{\partial \phi}{\partial t} = D\frac{\partial^2 \phi}{\partial x^2} \tag{4.8}$$

where $\phi$ is the concentration, $t$ is time, $x$ is position, and $D$ is the diffusion coefficient [19]. Mobile charge carriers, such as those in electrolytes, are related to the diffusion coefficient by the Nernst-Einstein equation:

$$\Lambda = \frac{z^2 e_0 F D}{k_B T} = \frac{z^2 N_A e_0^2 D}{k_B T} \tag{4.9}$$

where $\Lambda$ is the molar conductivity, $z$ is the valence of the charge carrier, $e_0$ is the elementary charge, $N_A$ is Avogadro's number, $k_B$ is the Boltzmann constant, and $F$ is the Faraday constant. Assuming a spherical species, though, $D$ can be defined by the Stokes-Einstein equation:

$$D = \frac{k_B T}{6\pi r \eta} \tag{4.10}$$

where $\eta$ is the viscosity of the electrolyte and $r$ is the effective radius of the idealized spherical species [24]. Thus the diffusion coefficient is dependent upon the concentration and attributes of the active species and its effect on the solution as a whole through the viscosity. Taking into account that the ionic conductivity is defined as $\sigma = \Lambda c = \Lambda n/V$, that is the product of the molar conductivity and the molar concentration, we can combine Equations 4.9 and 4.10 to define the ionic conductivity for a classical electrolyte as

$$\sigma = \frac{z^2 e_0^2}{6V\pi r}\frac{N}{\eta} \tag{4.11}$$

where $V$ is the volume of the solution and $N$ is the number of moles of the conductive species. Equation 4.11 lacks the features to fully describe the ionic conductivity of ionic liquid-based electrolytes. Unlike aqueous solutions, ionic liquids themselves are composed of cations and anions. During conduction the species of interest may come into contact with these ions and form temporary pairs or even more stable aggregates. In both cases, their function in the electrolyte changes such that the amount of conductive species, $N$, changes and cannot be easily determined at a given moment [24, 64].

The ionic conductivity can be determined empirically, though, via the EIS methods noted in Section 4.2.1. From the complex impedance the solution resistance, $R_{sol}$, can be determined at the high frequency intercept point of the real-valued axis. The ionic conductivity is then defined by

$$\sigma = \frac{t}{R_{sol}A} \tag{4.12}$$

where $t$ is the thickness of the gel polymer electrolyte or the distance between the blocking electrodes if they are submerged in a liquid electrolyte, $R_{sol}$ is the solution resistance, and $A$ is the area of contact between the blocking electrodes and with the electrolyte [46].

## 4.3 Experimental Methods

This section details the manufacturing process used to produce each gel polymer electrolyte, as well as the electrochemical methods used to analyze the behavior of the $Zn(OTf)_2$/[BMIm][OTf] electrolyte with and without the $Zn/MnO_2$ battery system. Thermal gravimetric analysis was used to determine the sufficient drying parameters of the gel polymer electrolyte. Electrochemical impedance spectroscopy and cyclic voltammetry were conducted to determine the ionic conductivity of the electrolyte and to obtain an equivalent circuit model of full cells. Cyclic voltammetry was conducted to quantify the reversibility of the reactions and determine the sufficient mass ratio of polymer binder to electrolyte.

### 4.3.1 Design of Experiments

This research investigated the effects between the amount of $Zn(OTf)_2$ salt added to [BMIm][OTf] and the ability of each composition to create solid gel polymer electrolytes when added to PVDF-HFP. Salts are typically added to ionic liquids to produce functional electrolytes [35, 67, 85]. The addition of a salt, though, has been shown to affect the viscosity of the ionic liquid as the number of charge carriers increases along with the ionic interactions [39]. When added to a gel, such as the solution of PVDF-HFP in NMP used here, the viscosity changes even to a greater degree. It then becomes important to understand how the conductivity of the electrolyte changes. Consequently, the effect of the GPE composition on the overall cell performance must also be considered.

Table 4.2 describes the salt concentrations and gel polymer electrolyte concentrations investigated. Compositions without PVDF-HFP are examined to provide a reference point for the cells with PVDF-HFP. The GPE concentration [1:1] parts by mass of electrolyte to PVDF-HFP was based on previous research [31]. A GPE concentration [2:1] was also investigated to determine how a heavily electrolyte-dominant GPE would affect cell performance and structural stability. The electrolyte concentrations [1:6.5], [1:15], and [1:30] for parts by mass of $Zn(OTf)_2$:[BMIm][OTf] were chosen based on previous research on these materials to take into account non-dilute and dilute concentrations [31, 42, 66].

### 4.3.2 Gel Polymer Electrolyte Manufacture

Each gel polymer electrolyte (GPE) was created by creating and combining two components: the gel and the electrolyte. The gel was created by adding 1 part by weight (pbw) of PVDF-

Table 4.2: Design of experiments for gel polymer electrolyte investigation.

| | | **$Zn(OTf)_2$:[BMIm][OTf] mass ratio** | | |
|---|---|---|---|---|
| | | **[1:6.5]** | **[1:15]** | **[1:30]** |
| **Electrolyte:PVDF-HFP mass ratio** | **[1:0]** | | | |
| | **[2:1]** | | | |
| | **[1:1]** | | | |

Table 4.3: Test parameters for thermal gravimetric analyzer (TGA) experiments.

| **Step No.** | **Step Name and Description** |
|---|---|
| 1 | Isothermal for 5.00 min |
| 2 | Ramp 5.00 °C/min to 80.00 °C |
| 3 | Isothermal for 360.00 min |

HFP into 5 pbw of N-methylpyrrolidone (NMP) (Alfa Aesar, ACS grade, 99.0+%). The PVDF-HFP was added to the NMP then placed in the sonicator with the heater on for at least 2 hours until fully dissolved. Upon completion of the gel, the desired amount of electrolyte was added to form the complete gel polymer electrolyte solution.

To create the solid GPEs, 24-30 drops of the desired composition were pipetted into a coin cell can that was adhered to a glass slide for handling. Large bubbles were removed by pipette. The cast solutions were then placed in an oven set to 80 °C overnight to ensure all of the solvent evaporated. Once fully dried, the outer lip of the GPE was removed either with scissors or a round punch.

### 4.3.3 Thermal Gravimetric Analysis

A thermal gravimetric analyzer (TGA) (TA Instruments, Q500 Thermogravimetric Analyzer) was used to determine the appropriate time required to fully evaporate all of the solvent in the electrolyte and obtain a solid film. The system was tared, or zeroed, with a stainless steel pan (TA Tzero Pan, 901683.901) on a platinum hanger. A sample was pipetted into the pan to fill the majority of the cavity without bulging at the surface or overflowing. The pan was then returned to the hanger and the test was initiated. The steps detailed in Table 4.3 were used to conduct the experiment.

### 4.3.4 Cyclic Voltammetry

Cyclic voltammetric tests were conducted on cells with different electrolyte compositions to ensure that the reduction and oxidation reactions at the zinc interfaces occurred. Ex-

Table 4.4: Test parameters for cyclic voltammetry (CV) experiments.

| Setting | Value | Setting | Value |
|---|---|---|---|
| Electrode Area ($cm^2$) | 1 | IRComp | None |
| Initial E (V) | 0 vs $E_OC$ | PF Corr. (ohm) | 50 |
| Scan Limit 1 (V) | 2.5 vs $E_OC$ | Equil. Time (s) | 5 |
| Scan Limit 2 (V) | -2.5 vs $E_OC$ | Init. Delay | On |
| Final E (V) | 0 vs $E_OC$ | Init. Delay Time (s) | 30 |
| Scan Rate (mV/s) | 100 | Init. Delay Stab. (mV/s) | 0 |
| Step Size (mV) | 10 | Sampling Mode | Noise Reject |
| I/E Range Mode | Fixed | Electrode Setup | On |
| Max Current (mA) | 100 | | |

Table 4.5: Test parameters for electrochemical impedance spectroscopy (EIS) experiments.

| Setting | Value | Setting | Value |
|---|---|---|---|
| Initial Freq. (Hz) | 1E6 | Conditioning | Off |
| Final Freq. (Hz) | 0.1 | Init. Delay | On |
| Points/decade | 10 | Init. Delay Time (s) | 100 |
| AC Voltage (mV rms) | 10 vs $E_OC$ | Init. Delay. Stab. (mV/s) | 0 |
| DC Voltage (V) | 0 vs $E_OC$ | Estimated Z (ohms) | 100 |
| Area ($cm^2$) | 1 | Optimize for | Normal |

periments were performed with a Gamry Reference 600, with the cyclic voltammetry (CV) experiment, and the settings listed in Table 4.4.

Cells were made by placing 50 $\mu$m-thick, 1 $cm^2$, square zinc foil electrodes on each stainless steel plate in the Swagelok cell mentioned previously. The GPE acted as the separator and ionically conducting medium between the zinc electrodes. Both interfaces were wetted with 2-4 drops of the electrolyte that matched the composition used in the GPE. After sealing the cell, a multimeter was used to ensure there were no electrical shorts. The working source and working reference were then connected to one of the electrodes, while the reference and counter source were connected to the other electrode.

### 4.3.5 Electrochemical Impedance Spectroscopy

To determine the ionic conductivity of each GPE or electrolyte and the impedance of full cells in coin cell packaging, electrochemical impedance spectroscopy (EIS) was performed. Impedance tests of for both electrolytes and full cells used a Gamry Reference 600 with the Potentiostat EIS experiment and the settings listed in Table 4.5.

To perform the analysis of GPEs, each solid film was placed in a Swagelok cell. The cell was made of flat, round, stainless steel plates that acted as blocking electrodes and were electrically isolated from each other, thus guaranteeing that only the impedance of the GPE would be measured. One plate was connected to a spring that applied a small amount of force to ensure contact. A teflon gasket insulated the plates from the large nut that secured the two halves together. To ensure there were no electrical shorts, the resistance between the electrodes was measured with a multimeter. A result of kOhms or higher indicated there were no electrical shorts. The working source and working sense leads were then connected to one of the electrodes while the reference and counter source were connected to the other.

### 4.3.6 Cell Cycling

It was required to charge and discharge, or cycle, each produced cell many times in order to sufficiently characterize its charge capacity, discharge capacity, energy density, efficiency, and degradation per cycle. Two Neware Battery Testing Systems (Model T1403-064242) with maximum voltages of 5 V and maximum currents of 10 mA were used to perform the cycling.

Each cell was charged to 1.8 V with a constant current of 60 $\mu$A. Upon reaching 1.8 V, the cell was held at a constant 1.8 V for 3 minutes with a decreasing current. Next, the cell was discharged at a constant 60 $\mu$A until it reached 1.0 V. Finally, the cell rested for 3 minutes until the next charging period began. Each cell was cycled for either 50 cycles or until failure, whichever occurred first.

## 4.4 Results and Discussion

### 4.4.1 Film Drying

As shown in Figure 4.6, each GPE composition was tested in a TGA using the procedure noted previously. There were no significant differences in drying of the GPEs based on their electrolyte composition. The drying rate was expected to plateau because evaporation occurred at the surface of the pan. The results indicated that the majority of NMP had evaporated out of the films after approximately 4.5 hours, thus drying overnight was sufficient. It is important to note that the time required to evaporate all of the NMP from the GPEs was on the order of hours, even at 80 °C. NMP was found to have a vapor pressure of 1.0 Torr at 20 °C, lower than that of water at 17.5 Torr at 20 °C [13]. Printing sufficiently thick films directly onto electrodes, as shown previously, resulted in the mixing of layers because the NMP had enough time during drying to dissolve the electrode. Increasing the temperature could provide a solution. [BMIm][OTf] begins to break down at 340 °C [20], while the PVDF-HFP begins to break down at 375 °C [48], thus the [BMIm][OTf] will provide the limiting temperature but the effect on the film structure has not yet been determined.

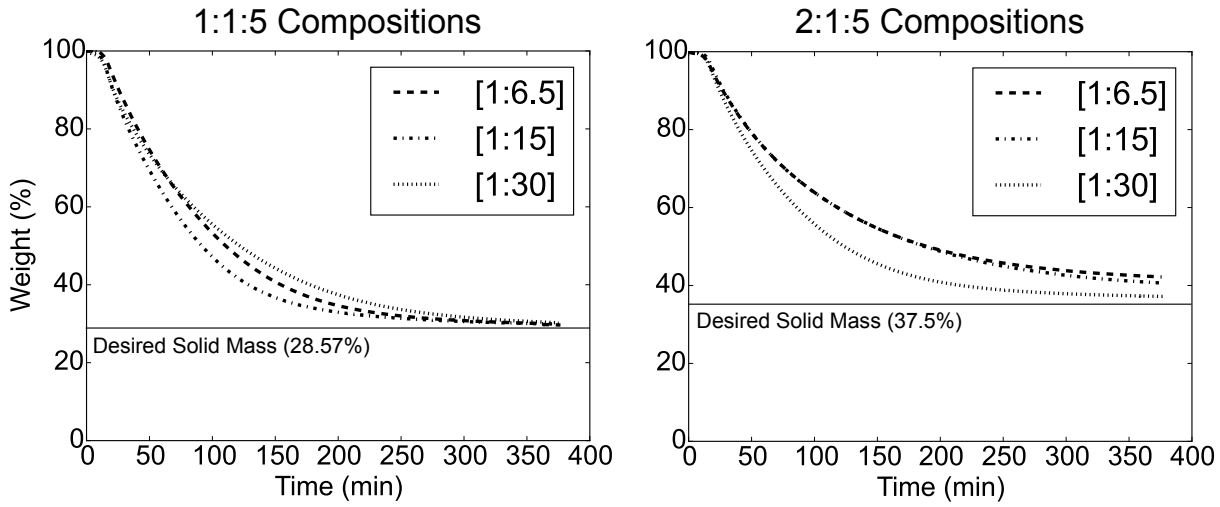


Figure 4.6: Change in weight during drying at 80 °C for gel polymer electrolyte 1:1:5 and 2:1:5 compositions of electrolyte:PVDF-HFP:NMP, respectively.

After manufacturing and drying each GPE film, it was removed from the oven and inspected. As the films cooled to room temperature, each began to "sweat" and release some of the electrolyte contained within the film, as shown in Figure 4.7. The droplets formed directly over the round, spherulite-like structures that comprised the film because of the different coefficients of thermal expansion. [BMIm][OTf] was found to have a coefficient of thermal expansion of $2.35\times10^{-4}$ °C$^{-1}$ [72] while bulk PVDF-HFP had a coefficient of thermal expansion of 1.53-1.9$\times10^{-4}$ °C$^{-1}$ [1]. This difference was significant enough to cause volume changes within the electrolyte as the films cooled from approximately 80 $°C$ to a room temperature of approximately 20 $°C$.

### 4.4.2 Gel Polymer Electrolyte Morphology

Each GPE composition was cast, dried, and allowed to cool to room temperature before being investigated under a microscope. As shown in Figure 4.8, all solutions formed spherulite-like structures. The size of those structures was heavily dependent on the amount of electrolyte added to the PVDF-HFP solution. All of the compositions with a ratio of 1:1 electrolyte:PVDF-HFP parts by mass had average sphere diameters on the order of 20 to 25 $\mu$m. The compositions with 2:1 electrolyte:PVDF-HFP parts by mass had average sphere diameters on the order of 10 $\mu$m.

The films were unable to be investigated with the laser confocal microscope because they were transparent, but the microscope images showed how the surfaces were very wavy as a result of the spheres. With the propensity of the GPE to form such structures, an unwetted film on printed electrodes would have high interfacial resistance, as noted previously for cells assembled without having electrolyte-wetted interfaces.

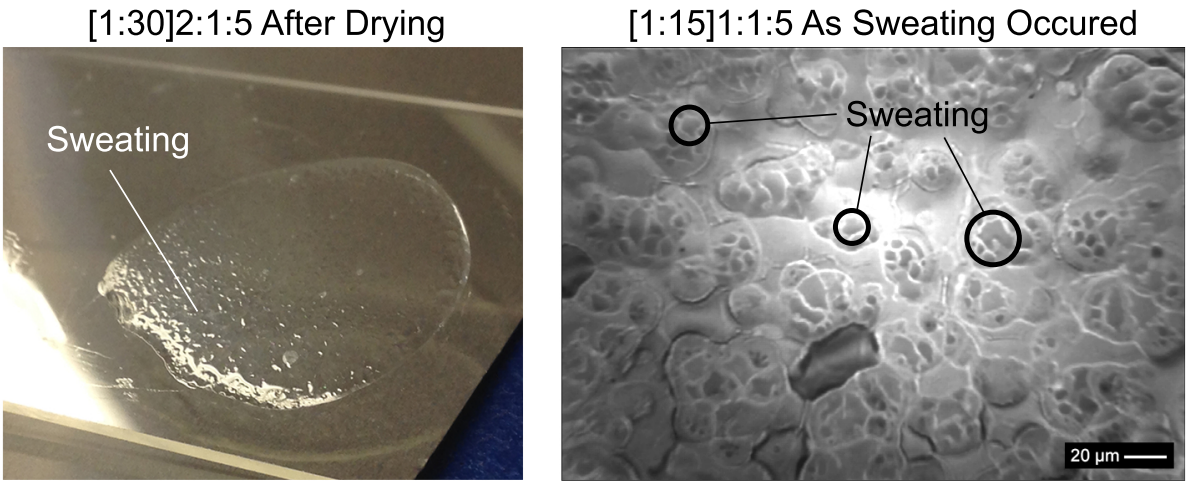


Figure 4.7: Left: Sweating on a cast GPE film of [1:30]2:1:5 after drying. Right: Microscope image at 40× magnification of [1:15]1:1:5 cast GPE film after drying as sweating began to occur.

### 4.4.3 Ionic Conductivity

Each GPE composition noted in Table 4.2 was cast and placed in a clean Swagelok cell to run EIS. Each EIS experiment resulted in a Nyquist plot of the real and imaginary impedance measured. A sample Nyquist plot is shown in Figure 4.9. Note that the Y-axis was plotted as the negative of the imaginary impedance. Of the measured data points, the solution resistance $R_S$ was determined from the points where the curve crossed the real axis or the point where the contribution of imaginary impedance was minimized. The resulting ionic conductivities were then calculated and plotted, as shown in Figure 4.10. Each bar represents a single sample. Four samples of each composition were tested to determine reproducibility and consistency of results.

As expected the GPE compositions with the highest mass ratio of electrolyte to PVDF-HFP attained the highest ionic conductivities. When examined in groups based on the ratio of electrolyte to PVDF-HFP, both the [1:30]1:1:5 and [1:30]2:1:5 compositions achieved the highest measured conductivities of their respective groups. The [1:30]1:1:5 composition achieved 0.077 mS/cm$^2$ with an average conductivity of 0.058 mS/cm$^2$. The [1:30]2:1:5 composition achieved 0.552 mS/cm$^2$ for a single sample and had an average conductivity of 0.399 mS/cm$^2$. Again in both groups, the [1:6.5]1:1:5 and [1:6.5]2:1:5 compositions had the lowest conductivities for a single sample and on average. The lowest measured [1:6.5]1:1:5 GPE was 0.019 mS/cm$^2$ and the set of samples had an average of 0.028 mS/cm$^2$. The lowest measured [1:6.5]2:1:5 GPE was 0.225 mS/cm$^2$ and the set of samples had an average of 0.288 mS/cm$^2$. Again in both cases, the [1:15]1:1:5 and [1:15]2:1:5 compositions had neither the highest nor the lowest performers, with averages of 0.042 mS/cm$^2$ and 0.326 mS/cm$^2$

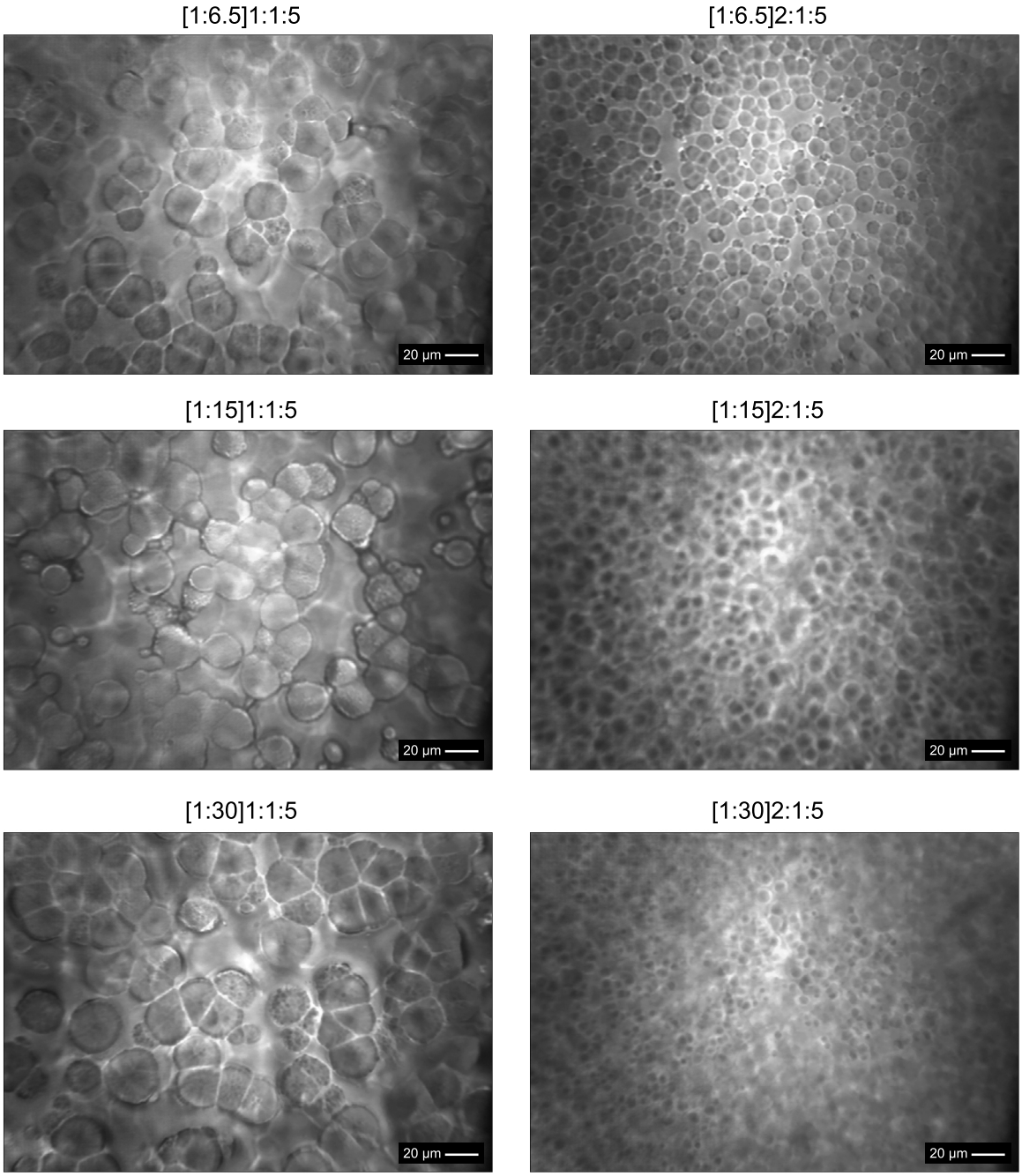


Figure 4.8: Microscope images of cast GPE films at 40× magnification. Note that the images were adjusted for clarity.

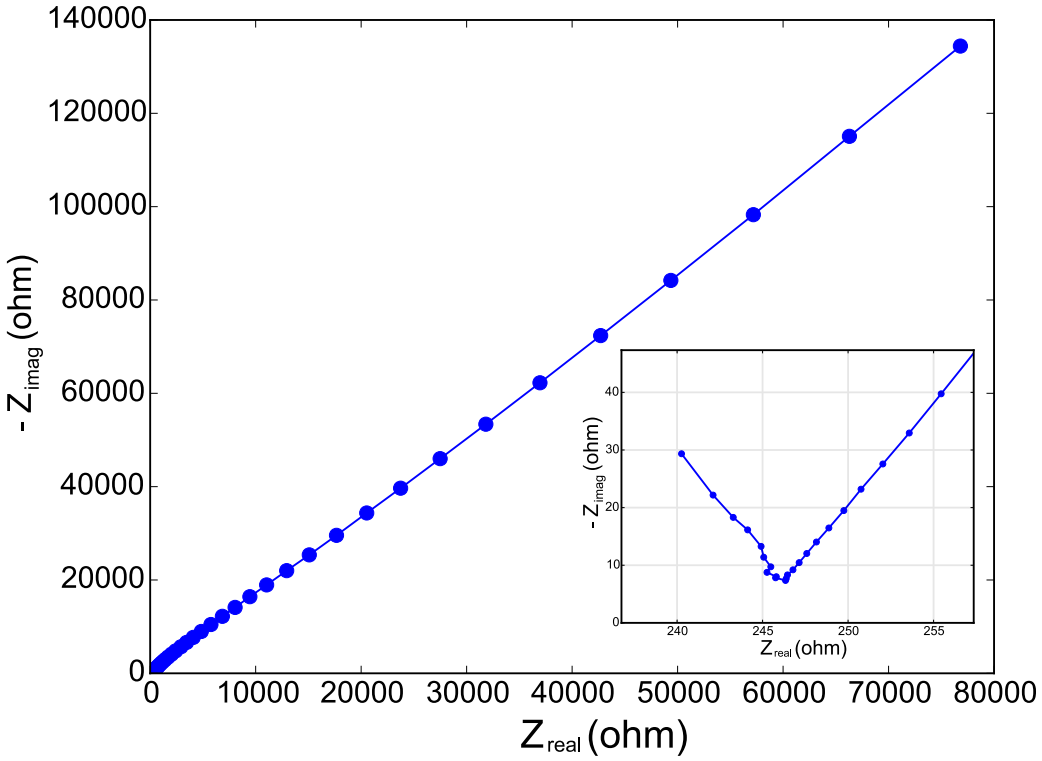


Figure 4.9: Nyquist plot for one sample of [1:30]1:1:5 GPE composition with inset of points closest to the origin.

respectively.

Considering that the ionically conductive medium was the electrolyte, increasing the amount present relative to the amount of PVDF-HFP was expected to increase the ionic conductivity, as shown here. In both groups of results the electrolyte with the most dilute composition, [1:30], had the highest conductivity on average across the four replicates. However there were no significant differences in conductivity on average within each group. The improvement in conductivity with the more dilute electrolytes was the result of the balance between the number of charge carriers and their interactions with other particles in solution [52]. Previous work showed that [BMIm][OTf] is not ionically conductive without the addition of a salt [42] and that an upper limit exists for the achievable conductivity relative to the amount of dissolved salt [47]. Additional experiments to determine those limits are recommended to find that limit.

These conductivity results helped elucidate which compositions might be good candidates for use in full cells. Unfortunately models did not exist to correlate the conductivity of ionic liquid-based electrolytes with their function in full cells. As a result, additional experiments with full cells made from the total set of compositions had to be conducted.

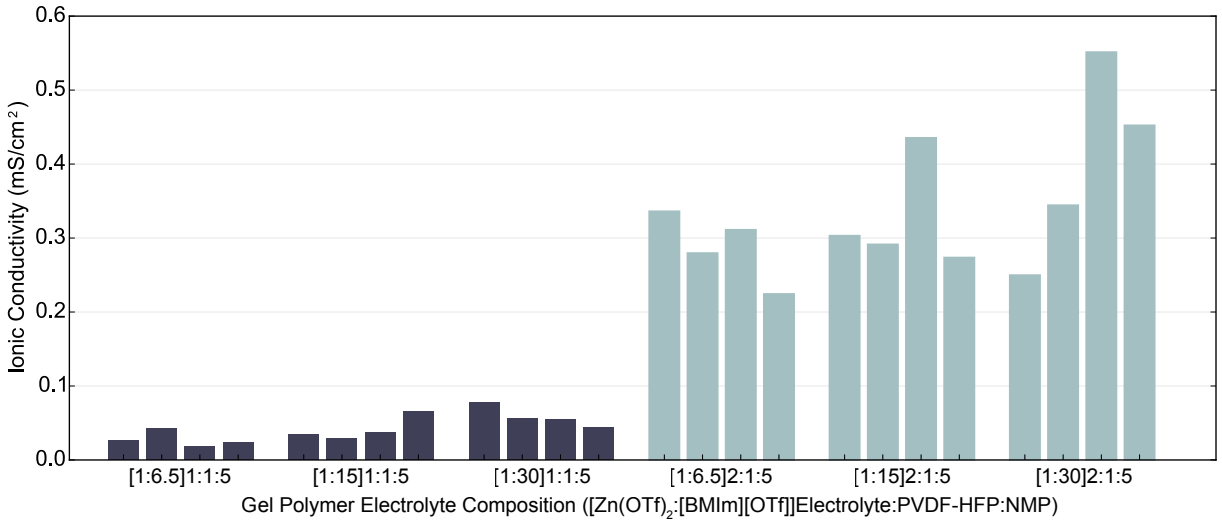


Figure 4.10: Effect of composition on ionic conductivity.

### 4.4.4 Cyclic Voltammetry

As discussed by Bard and Faulkner for compatible materials and chemistries, sweeping the potential to negative values results in reduction. As the applied potential approaches the reduction potential, current begins to flow as ions in vicinity of the electrode reduce and additional ions move via diffusion to that surface. A peak of current occurs when all ions on the surface have been reduced. As the applied potential passes the reduction potential, a depletion area occurs on the electrode surface because the additional reduction reactions are limited by how quickly the ions can diffuse to the surface. This causes the current to drop, resulting in the characteristic peak. Oxidation occurs similarly with a limit in the rate that ions can diffuse away from the surface [2]. Note that the experiments conducted here used symmetric cells where both electrodes were zinc foil. Thus the voltammograms were also expected to be symmetric.

Each electrolyte composition exhibited reduction-oxidation (redox) peaks and axis symmetry about the origin indicating a reversible reaction, as shown in Figure 4.11. Note that the results shown in the figure are for the sixth cycle of each test cell. The oxidation of zinc to a $Zn^{2+}$ ion and two electrons has been shown to occur at -0.76 V vs. $Zn^{2+}$/Zn. With non-idealities in the system, the peaks were expected to appear at that potential or one that was slightly more negative. In each case, the compositions with the [1:6.5] salt concentrations exhibited the highest current densities, with the composition [1:6.5]1:1:5 achieving the highest measured discharge current of 14.43 mA/cm$^2$.

The peaks corresponded to the reduction and oxidation of zinc at the interfaces, as noted previously. Thus it was expected that higher concentrations of salt would yield higher current

Table 4.6: Design of experiments for gel polymer electrolyte investigation.

| | | **$Zn(OTf)_2$:[BMIm][OTf] mass ratio** | | |
|---|---|---|---|---|
| | | **[1:6.5]** | **[1:15]** | **[1:30]** |
| **Electrolyte:PVDF-HFP mass ratio** | **[1:0]** | | | |
| | **[2:1]** | | | |
| | **[1:1]** | | | |

densities. It is interesting, though, that both the [1:6.5]1:1:5 and [1:15]1:1:5 compositions achieved higher current densities than [1:6.5]2:1:5 and [1:15]2:1:5 which had more electrolyte. The PVDF-HFP may have introduced impurities into the electrolyte causing additional side reactions and an increase in current density. If that was the case, then it would be plausible that the further dilution of those impurities with more electrolyte would reduce the current density. The difference in size of the spherulite-like structures may have also played a role. In addition, the presence of PVDF-HFP caused an overall increase in the current density, and at higher loadings may have also contributed to the drift of the redox peaks to potentials farther from zero.

It was observed from the curves that each composition responded differently to the cycling, where the redox peaks tended to either increase with each successive cycle, increase immediately after the first cycle then decrease with each successive cycle, or increase after the first cycle to a value and then remain approximately at that current density without any clear directional trend. Figure 4.12 shows an example of the phenomena, which indicated how the $Zn^{2+}$ concentration changed in the electrolyte with each cycle and potentially full cell cycle life. Stable cells are more desirable, like that shown for composition [1:6.5]1:1:5.

### 4.4.5 Cycle Capacity

As detailed in the design of experiments, the compositions investigated herein are outlined in Table 4.6.

Each electrolyte and GPE composition was cast, dried, and assembled into a wet stack coin cell with a 1 $cm^2$ stencil-printed composition A electrode and a 1 $cm^2$ piece of zinc foil as previously noted. Each composition was run until failure or completion of 50 charge and discharge cycles, whichever occurred first. The OCV of each cell was checked upon creation. Each cell had an OCV between 1.1 V and 1.3 V. The results of the cycle tests are presented in Figure 4.13.

Relative to the other compositions, the cells with an electrolyte composition [1:6.5] achieved the highest discharge capacity. As the salt concentration became more dilute, the average discharge capacity decreased. These results ran counter to those achieved from the ionic conductivity experiments: the more dilute compositions had higher ionic conductivities whereas the more concentrated compositions had higher discharge capacities. As

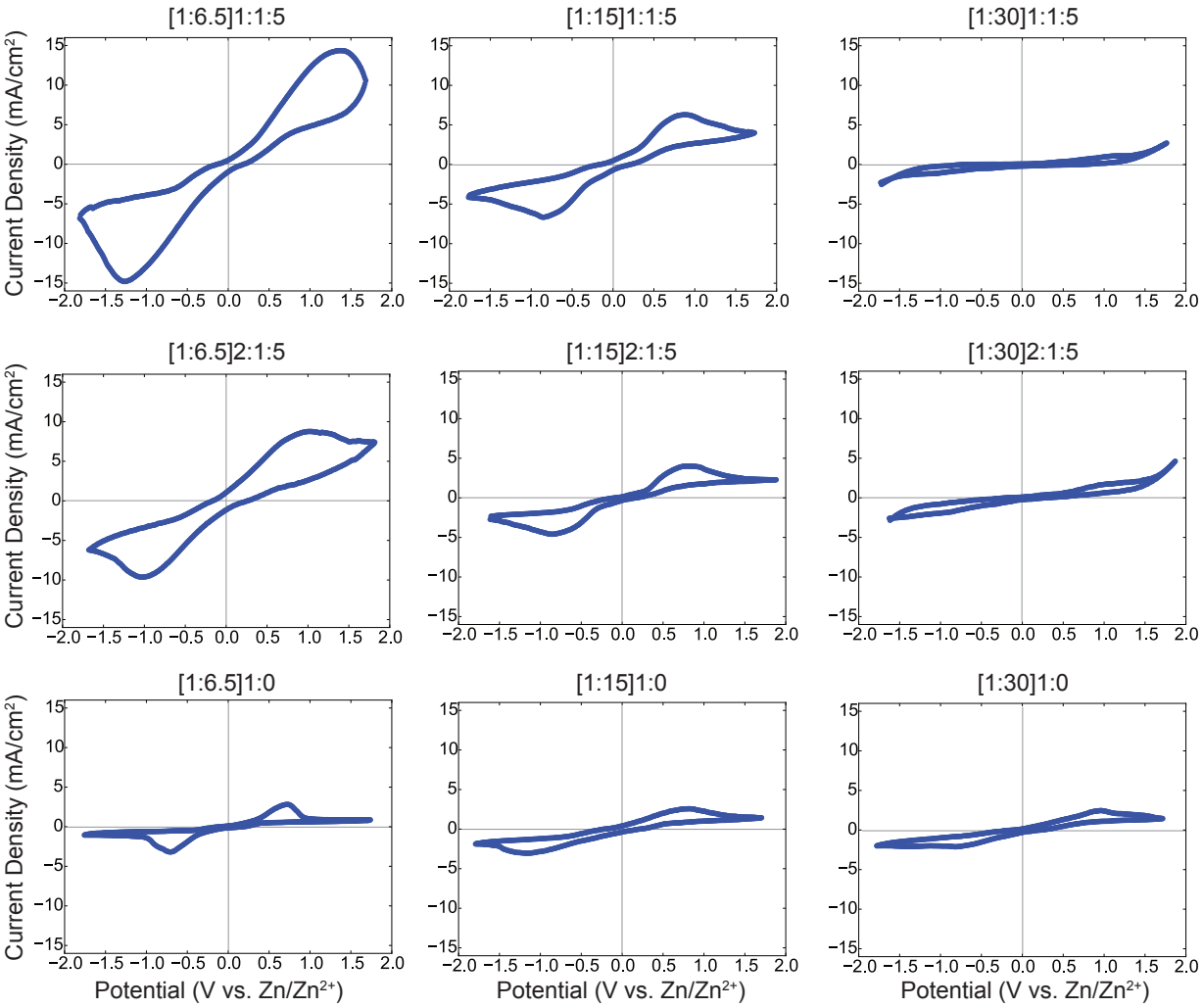


Figure 4.11: Reduction-oxidation peaks associated with each electrolyte composition on cycle 6.

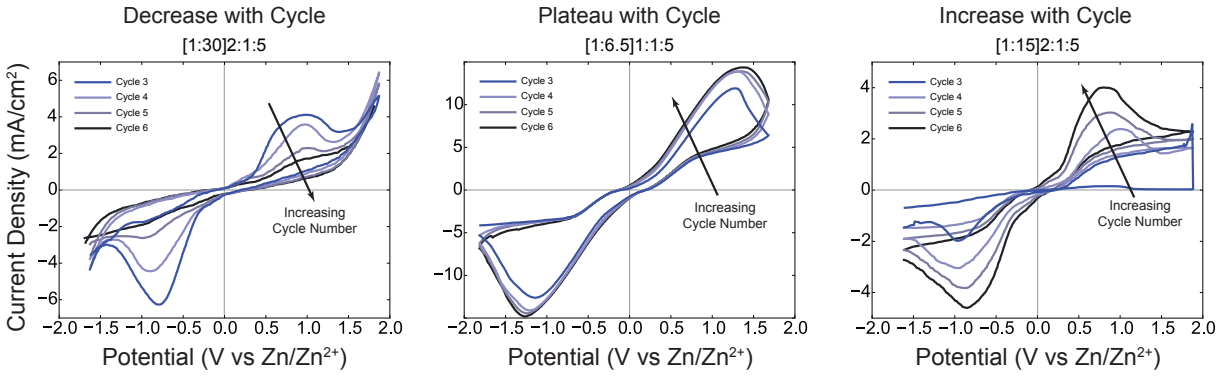


Figure 4.12: Comparison of [1:6.5]1:1:5 an [1:30]2:1:5 gel polymer electrolyte compositions over cycles 3 through 6 for cyclic voltammetry. Note the difference in scales.

noted previously, a balance between the number of charge carriers and the interactions that occur in solution can affect ionic conductivity [52]. During cell discharge, however, reactions did occur at the interfaces of the working and counter electrodes whereas no interfacial reactions occurred when measuring ionic conductivity because blocking electrodes were used. The results here indicate that a higher density of charge carriers had a beneficial impact on discharge capacity. Despite this a saturation limit of $Zn(OTf)_2$ in [BMIm][OTf] has not yet been experimentally quantified.

Upon investigating the cycle lives of the the cells, the cells created with the compositions without PVDF-HFP had much lower cycle lives. The single [1:6.5]1:0 cell that had the longest life also had the lowest discharge capacity of the four tested for that composition. Across the entire experimental set, enough outliers existed that no definitive trend for capacity versus GPE composition could be determined by looking at these data. What was visible, though, was that many cells with low discharge capacities achieved higher numbers of cycles or completed the full set of 50 cycles before being taken off the tester. Also the total accumulated discharge capacity, that is the sum of the discharge capacity per cycle, showed that the majority of the cells produced ended up providing around 2 $mAh/cm^2$ over their lives despite variations in cycle life and capacity, excluding the cells with any of the [1:30]1:0 compositions.

Figures 4.14 and 4.15 show the charge and discharge capacities and the cycle efficiency, respectively, for the cells that attained the highest average discharge capacities for each electrolyte composition. It is worthwhile to note how the cells without PVDF-HFP in their electrolyte were much less stable than their counterparts with PVDF-HFP. Overall the capacity tended to decrease for each cycle as indicated by efficiencies higher than 100%. More charge was being produced than was being put into the cells, thus it was likely that side reactions occurred during discharge to produce more current. The capacity could also have decreased as a result of irreversible replating of zinc onto the zinc foil. This would account for efficiencies lower than 100%. Contrary to the other results, the [1:30]2:1:5 cell showed an

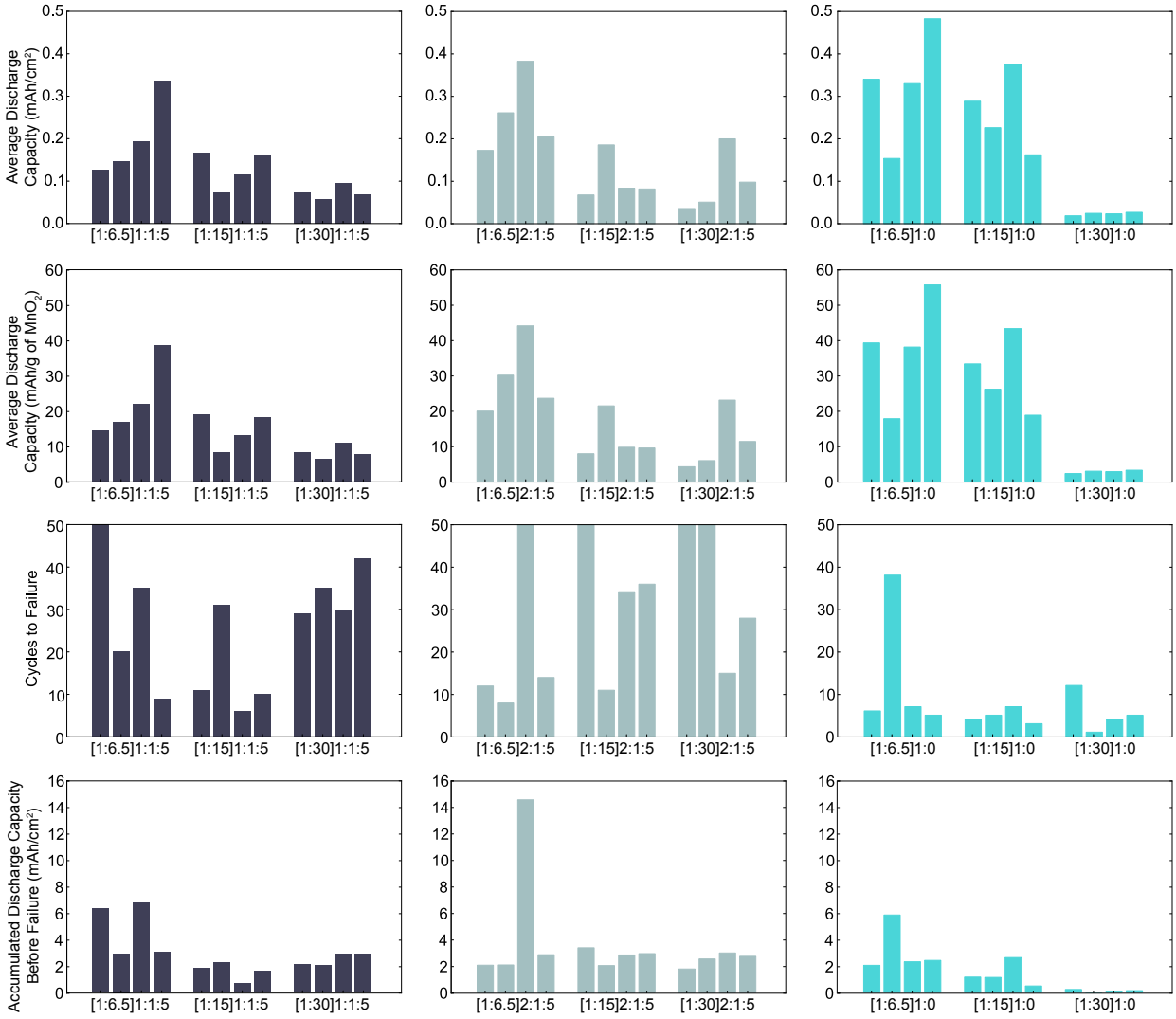


Figure 4.13: Comparison of average discharge capacity per unit area, average discharge capacity per gram of $MnO_2$, cycles to failure, and accumulated discharge capacity per unit area for 4 samples of each electrolyte and GPE composition.

improvement in discharge capacity from 0.118 mAh/cm$^2$ on cycle 1 to 0.240 mAh/cm$^2$ at cycle 9 before decreasing to 0.202 mAh/cm$^2$ on the final cycle. While this may have been attributable to structural changes during the first several discharge cycles, further investigation is required to understand why this occurred.

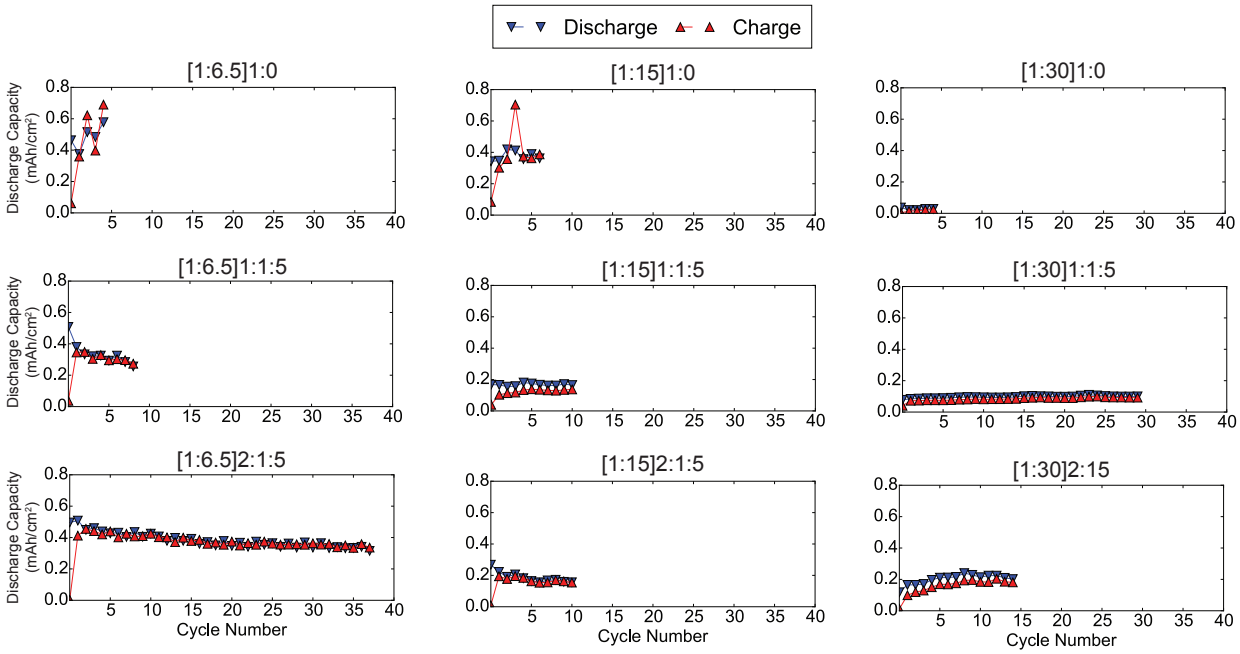


Figure 4.14: Per-cycle performance for the cells that attained the highest discharge capacities for each electrolyte composition.

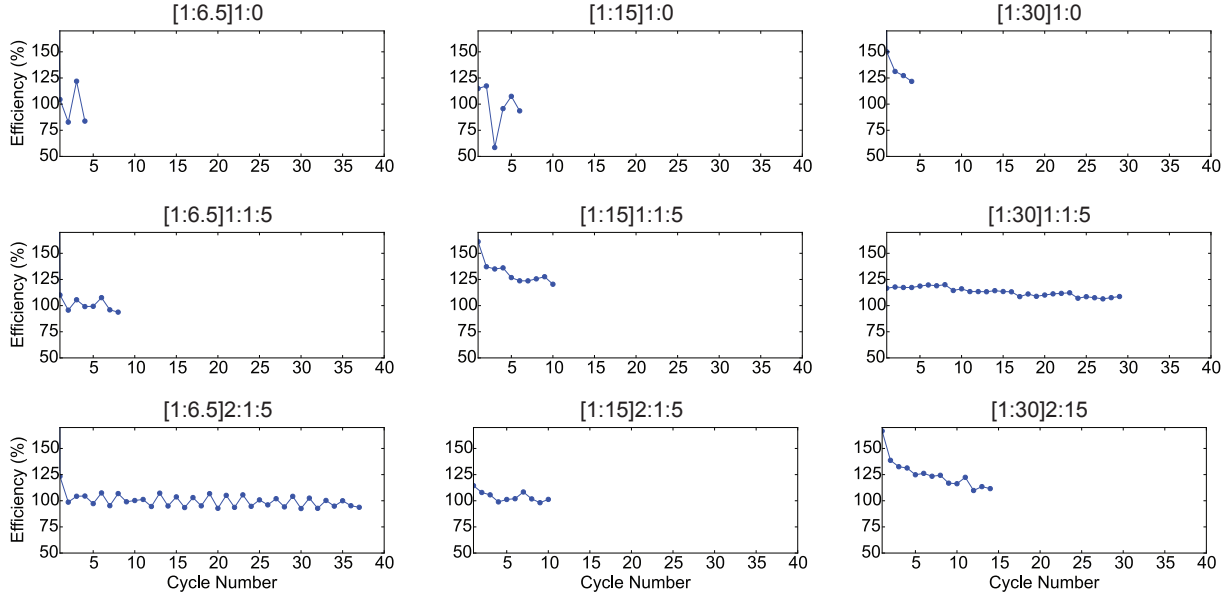


Figure 4.15: Coulombic efficiencies (100 × charge out/charge in) for cells that attained the highest discharge capacities for each electrolyte composition.

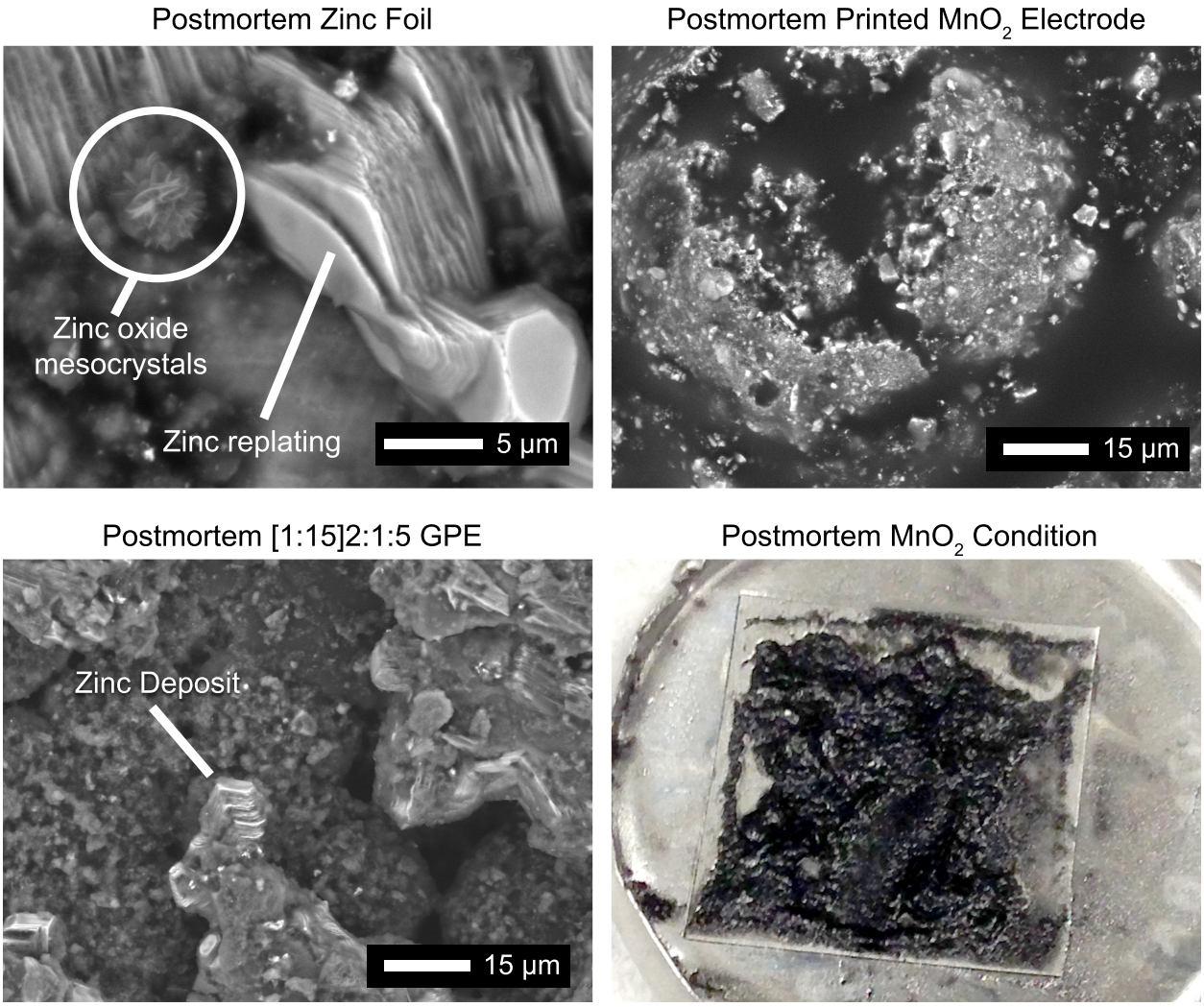


Figure 4.16: SEM images of zinc foil, a printed $MnO_2$ electrode, and a [1:15]2:1:5 GPE from a cell after cycling. A photograph of the printed $MnO_2$ electrode condition is included for reference.

### 4.4.6 Postmortem Analysis

It was important to investigate the system components after cycling to identify any potential causes for short cycle lives or low capacity. Figure 4.16 shows SEM images from a zinc foil electrode and a printed $MnO_2$ electrode after cycling. Several important phenomena were visible. First was that zinc replated into its common hexagonal close-packed structure, although many of the crystals grew orthogonal to the surface of the foil. This has been observed for electrochemical systems with $Zn(OTf)_2$ dissolved in [BMIm][OTf] [42]. Adjacent to the hexagonal crystals, though, ZnO mesocrystals were found. These have been shown to form in room-temperature environments with an abundance of $OH^-$ ions, commonly with $Zn^{2+}$:$OH^-$ ratios of 1:2 to 1:8 [79]. No additional materials were dissolved into the electrolyte aside from the $Zn(OTf)_2$, so side reactions most likely occurred to form $Zn(OH)^-$ and/or free $OH^-$ ions that in turn reacted to form ZnO. These materials are considered to be undesirable in zinc batteries because they form ZnO that passivates the elemental zinc surface and removes $Zn^{2+}$ ions from the desired set of electrochemical reactions.

Conversely the printed $MnO_2$ electrode seemed to breakdown during cycling, as visible in Figure 4.16. This phenomenon has been noted by other researchers working with $Zn/MnO_2$ cells with a KOH electrolyte [58]. For the chemistry noted here, this could have been attributable to the low mass of PVDF-HFP in the ink resulting in a structurally weak film. On discharge, the $MnO_2$ electrode has been hypothesized to allow zinc to intercalate into its crystal lattice, thus it would have to swell as it absorbed the additional material. It was likely that at some critical saturation point, then, the film would begin to break apart. This could be counteracted by using additional PVDF-HFP in the electrode recipe, but as mentioned previously, too much could coat the majority of the reactive material and render the electrode electrochemically inactive.

It was difficult to separate the GPE from the zinc electrode because, as the cell cycled and zinc dissolved and replated, it began to grow into the GPE layer, as shown in Figure 4.16. While this result was beneficial because it suggested that the $Zn^{2+}$ ions were mobile through the polymer and not simply in the pores between the spherulites, it could have ramifications for the limits with which the cells could cycle. If the zinc foil did not fully reform on the charge cycle, it could, for all intents and purposes, be losing active material and result in a reduced capacity as the number of cycles grew.

Zinc dendrites, were not found on either the zinc surface or in the GPE. This has been shown previously for dried, [BMIm][OTf]-based electrolytes [42], but not for the same materials prepared in ambient conditions, as investigated herein. While the presence of the ZnO mesocrystals indicated that side reactions with oxygen were likely, their presence was rare on the investigated surfaces.

## 4.5 Conclusions

This chapter investigated the function and effect of the electrolyte and GPE composition in affecting the performance of $Zn/MnO_2$ cells. The rate of drying, film morphology, ionic conductivity, cell capacity and postmortem cell conditions were investigated using thermal, electrical, and optical methods. Three compositions of electrolyte with three compositions of gel were produced, cast, and implemented to better understand the limitations of the system and materials used within this research.

The results presented here indicate that the ionic conductivity, a metric traditionally used to determine the quality of an electrolyte, was not a good indicator of overall cell capacity. Conversely, electrolytes with higher concentrations of salt had, on average, low conductivities but also higher capacities. The development of an optimal ratio of $Zn(OTf)_2$:[BMIm][OTf] should be a focus of additional experiments moving forward, whereby the saturation limit of $Zn(OTf)_2$ in [BMIm][OTf] can be found.

Depending on the amount of electrolyte present, the GPEs had different morphologies. Inspection of the films showed that, while GPEs with more electrolyte yielded greater conductivity, they were much weaker than their lower concentration counterparts. While using the punch to cut out a disc, the 2:1:5 compositions sometimes broke apart and were very easy to cut, while the 1:1:5 compositions were very tough and often required the additional use of scissors to cut out the disc. There was no direct indication that the cell performance was affected by the size of the spherulite-like structures or a higher concentration of electrolyte from the number of samples for each composition presented here. A large number of cells for a single composition is recommended to illuminate the issues presented here.

From the postmortem results, the breakdown of the $MnO_2$ electrode was a likely cause of cell failure. As such, alternative compositions with additional PVDF-HFP are recommended to provide additional structural stability and flexibility during cell cycling. The deposition of zinc within the GPE could also have caused a reduction in capacity.

A greater interest must be taken in the interfacial mass transport and reactions to determine both an optimal electrolyte composition and optimal GPE morphology. Drying time and temperature may also heavily affect these qualities, but special care to observe the thermal limits for PVDF-HFP must be observed to prevent the production of HF vapor.

Overall the results presented in this chapter indicate that a higher concentration of salt, that is the [1:6.5] electrolyte compositions, have the best performance for cycle life, discharge capacity, and current density.

# Chapter 5

# Water-Electrolyte Interactions

## 5.1 Introduction

This chapter investigates and quantifies the function, composition, and effects of the presence of water within [BMIm][OTf]-based electrolytes at different concentrations in order to improve cell capacity and manufacturing yield. Different quantities of $Zn(OTf)_2$ salt were dissolved into the [BMIm][OTf] ionic liquid to form the electrolytes and acquire initial saturation data. Focus was given to the mass ratio of [1:15] for $Zn(OTf)_2$:[BMIm][OTf] to reduce the number of compositional variables to investigate. Section 5.2 provides a brief overview of Karl Fischer titration, the main method used to determine the amount of water present within each electrolyte. Section 5.3 provides an overview of the methods used to conduct this research include the design of experiments, gel polymer electrolyte manufacturing, and Karl Fischer titration. Section 5.4 discusses the results acquired for Karl Fischer titration, cyclic voltammetry, cell cyclability, and postmortem analyses. Finally, Section 5.5 details the final conclusions that can be discerned from the results presented herein.

## 5.2 Electrochemical Methods

This section presents the fundamentals associated with Karl Fischer titration and the chemistry used to determine how much water is present in a tested material.

### 5.2.1 Karl Fischer Titration

Karl Fischer titration is a robust, rapid way of determining the amount of water contained within a given sample. The method uses a methanolic solution to react with water in specific molar quantities, given by

$$H_2O + I_2 + [RNH]SO_3CH_3 + 2\,RN \longrightarrow [RNH]SO_4CH_3 + 2\,[RNH]I \tag{5.1}$$

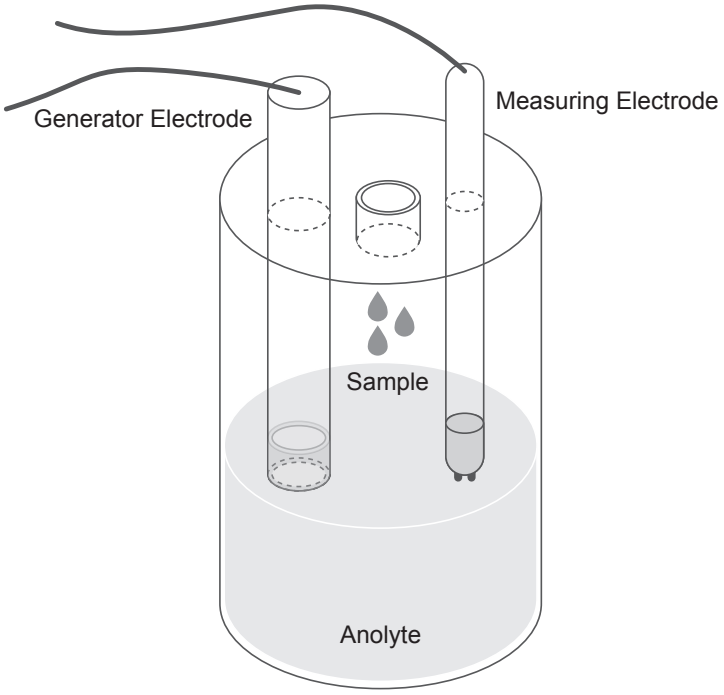


Figure 5.1: Common coulometric titrator equipment setup.

where RN is a base. A basic requirement of all Karl Fischer reactions is the reaction of sulfur dioxide with the alcohol producing a monoalkyl ester of the sulfurous acid [70].

Coulometric titration is a common way of measuring water in a sample via the Karl Fischer reaction. A direct current must be applied to generate iodine from iodide dissolved in the system. This system then "counts" the amount of current required to produce the iodide which is directly proportional to amount of water in the sample [15].

The system is commonly setup with a titration cell containing the anolyte. For a diaphragm-less generator electrode, as is used in this research, the cathode is small and placed in such a way so that the iodine will react with the water before reaching it. A measuring electrode is present to measure the voltage in the cell as the reactions are taking place [29]. The typical coulometric titrator setup is shown in Figure 5.1.

## 5.3 Experimental Methods

This section details the manufacturing process used to produce each ionic liquid-based electrolyte and the analytical methods implemented to analyze said electrolytes.

Table 5.1: Design of experiments to investigate the effect of water on the [1:15] electrolyte composition.

| | | **Water concentration** | | |
|---|---|---|---|---|
| | | **Dry** | **+0.5% Water** | **+3.0% Water** |
| **Electrolyte:PVDF-HFP mass ratio** | **[1:0]** | | | |
| | **[2:1]** | | | |
| | **[1:1]** | | | |

### 5.3.1 Design of Experiments

This research investigated the effects of water saturation relative to the amount of $Zn(OTf)_2$ salt dissolved within [BMIm][OTf], the ability of each composition to create solid gel polymer electrolytes when added to PVDF-HFP, and cell performance as affected by the presence of water. Salts are typically added to ionic liquids to produce functional electrolytes [35, 67, 85]. Three concentrations of salt were chosen with $Zn(OTf)_2$:[BMIm][OTf] mass ratios of [1:6.5], [1:15], and [1:30] to determine how pronounced an effect the salt had on the saturation of water. Because so little was known about the interactions of such salts, ionic liquids, and water the [1:15] composition was chosen to be investigated in greater detail. That composition of electrolyte was dried and saturated to acquire specific quantities of water.

Table 5.1 describes the water concentrations and gel polymer electrolyte concentrations investigated for the [1:15] electrolyte. Compositions without PVDF-HFP are examined to provide a reference point for the cells with PVDF-HFP. The GPE concentration [1:1] parts by mass of electrolyte to PVDF-HFP was based on previous research [31]. A GPE concentration [2:1] was also investigated to determine how a heavily electrolyte-dominant GPE would affect cell performance and structural stability. Dry materials were used to provide a basis of comparison to compositions as additional water was added. Deionized (DI) water was then added as a percent of the initial electrolyte weight to produce solutions with 0.5% and 3.0% additional water. Thus for 1 g of electrolyte the addition of 3% of DI water represented a total of 1.03 g of solution. These values were chosen to provide a spread of concentration values relative to the maximum saturation limit of 4.69% as shown in the literature for [BMIm][OTf] [10].

### 5.3.2 Electrolyte Manufacture

To produce each electrolyte, the [BMIm][OTf] ionic liquid was first pipetted into a bottle with the desired mass. Then, the desired mass of $Zn(OTf)_2$ was measured on weigh paper before being added to the ionic liquid. Upon adding the salt to the ionic liquid, the mixture was placed on a hot plate between 80-90 °C for approximately 24 hours to allow the salt to dissolve. Upon completion, no salt remained at the bottom of the bottle, and the solution

was transparent but exhibited a slight amber color.

Deionized (DI) water was added to the electrolytes by using the electrolyte solution as a reference. The mass percentage of DI water added was the corresponding mass percent of the solution.

### 5.3.3 Electrolyte Drying and Saturation

To dry the electrolytes, each was placed in a vacuum oven (Jeio Tech, OV-11) at 100 °C with the pressure reduced to approximately -0.09 MPa gage for 48 hours. Upon completion, the temperature was allowed to slowly return to room temperature. The oven was then refilled with argon (Praxair, 5.0 Ultra High Purity) to return the chamber to ambient pressure. The electrolytes were then immediately moved into the glovebox containing a dry (-78 to -79 °C dew point, 0.1 to 0.0% relative humidity) argon environment with between 0.17 and 0.25 parts per million (ppm) of oxygen. Test quantities were then removed from the glovebox via pipette in order to perform Karl Fischer titration.

The $Zn(OTf)_2$ salt was also dried under the same conditions before being transferred into the dry glovebox. The dried salt was then added to [BMIm][OTf] that was only opened in the dry, argon environment of the glovebox to ensure low quantities of water.

### 5.3.4 Karl Fischer Titration

The mg of water/g of solution in each electrolyte was determined with a Mettler Toledo DL39 Karl Fischer Coulometer with a diaphragm-less electrode located in an argon-filled glovebox. The titration cell was filled with 100 mL of AQUASTAR CombiCoulomat Fritless Reagent (EMD Millipore, 1.09257).

After turning on the system, the standard startup procedure with code 911 was used. This procedure first reacted with any water absorbed from the environment to obtain a steady-state value. Then the system calibrated itself by measuring the amount of water absorbed into the anolyte per minute. The solution was allowed to equilibrate until the drift from absorption of water within the glovebox atmosphere was less than 10 $\mu$g/min. The bottle containing the electrolyte to be analyzed was then placed on the scale and used as the tare weight. A sample of material was drawn into a pipette, the button labeled “Sample” was pressed, and the material was added to the titrator solution under the white stopper. The pipette was placed back on the scale to obtain an exact weight of mass added to the titrator solution. The negative value on the scale was then entered on the titrator for the system to calculate the mg/g of water in the sample.

Table 5.2: Amount of water present in electrolyte compositions with $Zn(OTf)_2$:[BMIm][OTf] mass ratios of [1:6.5], [1:15], and [1:30] as determined by Karl Fischer titration after drying in a vacuum oven. Note that the units are mg of $H_2O$ per gram of solution.

| Composition | Sample 1 | Sample 2 | Average |
|---|---|---|---|
| [1:6.5] Dried | 9.172 | 9.231 | 9.202 |
| [1:15] Dried | 5.739 | 5.696 | 5.717 |
| [1:30] Dried | 3.196 | 3.196 | 3.196 |

Table 5.3: Amount of water present in electrolyte compositions with $Zn(OTf)_2$:[BMIm][OTf] mass ratios of [1:6.5], [1:15], and [1:30] as determined by Karl Fischer titration after being mixed in ambient conditions for 24 h. Note that the units are mg of $H_2O$ per gram of solution.

| Composition | Sample 1 | Sample 2 | Average |
|---|---|---|---|
| [1:6.5] Saturated | 89.24 | 88.56 | 88.90 |
| [1:15] Saturated | 64.54 | 54.49 | 59.51 |
| [1:30] Saturated | 57.13 | 56.04 | 56.58 |

## 5.4 Results and Discussion

### 5.4.1 Water Absorptivity

The water sensitivity of the electrolyte was first examined by creating several electrolyte compositions with varying masses of dissolved salt. Electrolyte compositions of [1:6.5], [1:15], and [1:30] mass ratios of $Zn(OTf)_2$:[BMIM][OTf] were produced in ambient conditions with a temperature of 22-24 °C and relative humidity of approximately 40% for investigation. They were then dried according to the procedure described previously. Samples of each composition were also allowed to mix on a vortex mixer at 800 revolutions per minute (rpm) for 24 hours to determine upper limits of saturation from humidity.

As expected the electrolytes with the higher salt concentrations were able to absorb more water, as shown in Tables 5.2. Research has shown that the anion plays a major role in water sorption into ILs [10], and the system is being flooded with anions with the addition of $Zn(OTf)_2$ to [BMIm][OTf]. Importantly, though, solubility of water was also found to depend on hydrogen bonding with the cation [21]. Apparently this influence allowed the electrolytes to retain large quantities of water after drying, between 0.31% and 0.92% depending on the salt concentration. This finding is important because it means that high heat and low pressure are insufficient mechanisms to completely remove water from these materials once they have absorbed it.

The amount of water absorbed by the electrolytes from ambient conditions is described

Table 5.4: Amount of water in an electrolyte composition with a $Zn(OTf)_2$:[BMIm][OTf] mass ratio of [1:15] as determined by Karl Fischer titration with different amounts of deionized water added. The ionic liquid [BMIm][OTf] was tested without any $Zn(OTf)_2$ salt as a reference. Note that the units are mg of $H_2O$ per gram of solution.

| **Composition** | **Sample 1** | **Sample 2** | **Average** |
|---|---|---|---|
| [BMIm][OTf] Only | 0.0447 | 0.0437 | 0.0442 |
| [1:15] Unexposed to ambient | 1.3786 | 1.6283 | 1.5035 |
| [1:15] + 0.5% of solution | 13.9084 | 14.6939 | 14.3012 |
| [1:15] + 3.0% of solution | 26.3974 | 25.5406 | 25.9690 |

in Table 5.3. As stated previously, the saturation limit determined by Cao *et al.* for [BMIm][OTf] was 4.69% of water [10]. With the addition of salt, though, that value has nearly doubled for the electrolyte with the highest concentration of salt. In all cases, after 24 h of mixing in ambient conditions, the electrolytes had absorbed more water than pure [BMIm][OTf]. The highest observed saturation was the [1:6.5] composition where approximately 8.9% of its mass was water.

Xu *et al.* observed that the addition of water up to 0.5% to 1-butyl-1-methylpyrrolidinium bis(trifluoromethanesulfonyl)imide (BMP-TFSI) approximately doubled the diffusion coefficient for $Zn^{2+}$ ions while 2.0% added water improved the reversibility of zinc redox reactions [86]. Despite the material used in the study, this result seems to encourage the addition of water within ionic liquid-based electrolytes although the quantity added must be tightly controlled.

The [1:15] electrolyte composition was chosen to be focused on because of its mid-range propensity for retaining water from the salt concentrations already investigated. The results from the addition of different quantities of water are presented in Table 5.4 including the results for dry [BMIm][OTf] that had not been exposed to an ambient atmosphere and was packed in argon. As expected, the pure [BMIm][OTf] was incredibly dry with a composition of only 0.004% water. Despite being dried at an elevated temperature and low pressure, the $Zn(OTf)_2$ salt seemed to retain a large quantity of water. When it was added to the dry [BMIm][OTf] it increased the water content to 0.15%. The other electrolytes with 0.5% and 3.0% water added were created simultaneously with the same container of [BMIm][OTf]. Interestingly the electrolyte with the 0.5% water added yielded a composition with approximately 1.4% water in total, and the electrolyte with 3.0% water added yielded a composition with approximately 2.6% water in total. The result of this discrepancy from the additional water is unknown, although the environment, salt, and exposure may have played roles. It should be noted that in order to conduct Karl Fischer titration measurements the containers had to be opened when placed in the transfer chamber during pump down for insertion into the glovebox. It is also unknown if this had any significant effect.

### 5.4.2 Ionic Conductivity

Each GPE composition noted in Table 5.1 was cast and placed in a clean Swagelok cell to run EIS using the previously discussed settings and conditions. It is interesting to note that the addition of water did not have a pronounced effect on the conductivity of the GPEs. For the 1:1:5 compositions, samples with 0.5% water and 3% water added had average ionic conductivities of 0.0297 mS/cm and 0.0286 mS/cm respectively. For the 2:1:5 compositions, the 0.5% water and 3% water added samples had average ionic conductivities of 0.318 mS/cm and 0.324 mS/cm respectively. Inspection shows no significant difference between the data for the +0.5% and +3.0% water samples. As expected, the addition of more electrolyte provided the greatest benefit to the ionic conductivity with a 10× increase in value.

Importantly the GPEs produced within the glovebox did not sweat. As shown by previous researchers, ILs have the propensity to absorb water at elevated temperatures [9]. Within the glovebox, though, very little water was present as the dew point was measured between -79 and -80 °C. Thus it seemed that the sweating was at least partially related to the presence of water in the environment. It should be noted that each EIS experiment was conducted without the addition of electrolyte at the interfaces of the GPE and the blocking electrodes. This along with the lack of sweating to produce a decent interface may account for the difference in ionic conductivity between the dry [1:15]2:1:5 sample and the others that were produced in ambient conditions with additional water.

It should also be noted that there was a significant color change. Inside the glovebox, the dried GPEs remained transparent or whitish, while those dried in air became yellowish or amber, especially at the corners of the coin cell can they were cast in. This may be due to the presence or creation of ZnO that is known to have a yellowish to reddish color under some circumstances. Srikant and Clarke, while investigating the optical band gap of ZnO did propose that "heating ZnO in air at high temperatures could enhance the color" and that it could be related to oxygen vacancies [75]. As shown previously, the GPE was not a monolithic, perfectly smooth material, thus there could have been many locations for oxygen to adsorb and enhance the color. Both the sweating and color differences are shown in Figure 5.3.

### 5.4.3 Cyclic Voltammetry

Each composition was made with the previously discussed method where two pieces of zinc foil sandwiched a wetted GPE or pure electrolyte sample. These samples then had cyclic voltammetric tests performed on them to determine if redox peaks were present and to qualify them if found. The results of which are shown in Figure 5.4.

The cells with 0.5% additional water exhibited the tallest redox peaks between 5 mA and 8 mA. The [1:15]1:0 cell with 0.5% additional water had well defined peaks around the 0.76 V and -0.76 V expected for the oxidation and reduction of zinc. Upon adding PVDF-HFP, the peaks became less well defined as the potential window within which reactions were found to occur expanded. While the addition of PVDF-HFP may have resulted in some side reactions

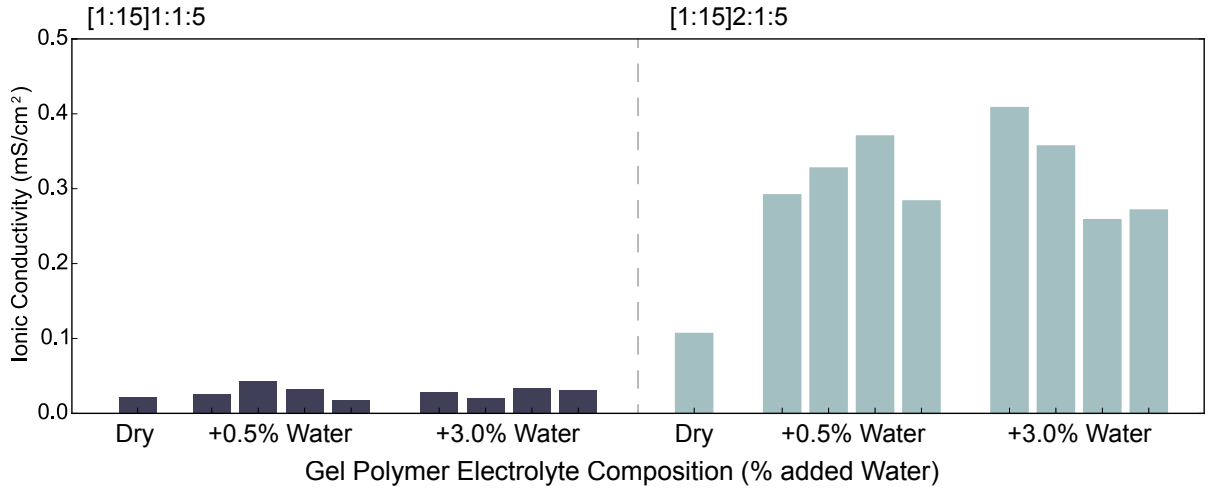


Figure 5.2: Effect of composition and water content on the ionic conductivity. Note that the composition is described as a ratio of parts by mass of Electrolyte:PVDF-HFP:NMP, where the electrolyte composition is denoted in square brackets as [$Zn(OTf)_2$:[BMIm][OTf]].

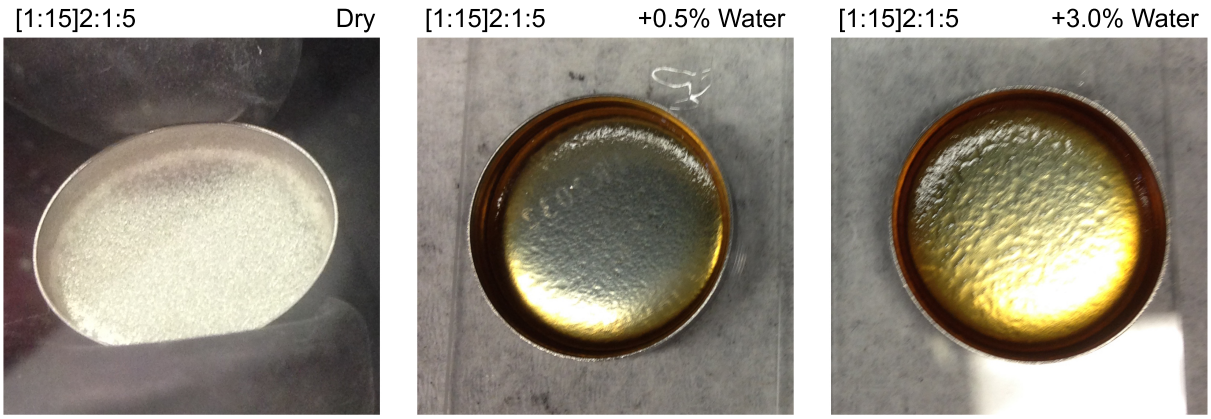


Figure 5.3: Difference in sweating for each GPE composition.

and a shift in the peaks, this phenomenon did not occur in every sample. The extrema for the [1:15]1:1:5 with 3.0% additional water sample did not shift after the PVDF-HFP was added and actually saw a reduction in the redox peak. It is unknown why this occurred but it indicated poor reaction kinetics at the interface, at least for zinc. Across all of the samples that had 3% water added the peaks were very poorly defined and could indicate that full cells with this electrolyte composition would perform poorly. The dry [1:15]1:1:5 actually saw a slight improvement in the definition of the peaks at the desired potentials when the PVDF-HFP was added. As the composition changed such that there was more electrolyte than polymer as in the 2:1:5 sample, the peaks again began to revert back to where they were in the sample with no PVDF-HFP.

Overall the results indicated that full cells produced with 0.5% additional water might have better performance than the other compositions, and that cells with PVDF-HFP, specifically [1:15]1:1:5, could be the best. The results also indicated that there is most likely an optimal amount of water that should be present within the electrolyte to enhance performance. The presence of water, though, would also result in the possibility of that it could be electrolyzed at potentials at or above 1.2 V. This was expected to be seen within the CV samples generated, but from the results was not clear. Additional experiments with intermediate amounts of dissolved water are required to determine if the electrolysis of water would show distinct peaks and/or dominate the reactions within the cell.

### 5.4.4 Cell Cyclability

Each electrolyte and GPE composition was cast, dried, and assembled into a wet stack coin cell with a 1 $cm^2$ composition A electrode and a 1 $cm^2$ piece of zinc foil as previously discussed. To reiterate composition A was composed of 90% $MnO_2$, 6% acetylene black, and 4% PVDF-HFP as mass fractions of the solid materials. Each composition was run until failure or completion of 50 charge and discharge cycles, whichever occurred first. The results of the cycle tests are presented in Figure 5.5. Note that the [1:15]1:0 dry composition yielded no cyclable cells and the [1:15]1:0 +3.0% water composition yielded only 3 cyclable cells. Despite this, spaces for each of those cells produced remain for graphical consistency and discussion. Upon cell creation, the OCV was tested for each cell. While the cells produced in air with additional water had OCVs between 1.1 V and 1.2 V, the dry compositions all had OCVs between 0.9 V and 1.1 V with the majority closer to 0.9 V.

The cells made were cycled, as noted previously, with a constant current charge of 0.060 mA up to 1.8 V, followed by 3 minutes being held at 1.8 V with a decreasing current, followed by a discharge of 0.060 mA down to 1.0 V, finally ending with a 3 minute rest after discharge. As is visible in Figure 5.5, the distribution of performance among the cells with electrolyte and GPE compositions that had water added was very high, from average discharge capacity to cycles to failure and accumulated discharge capacity. For the [1:15]2:1:5 and [1:15]1:0 compositions, the samples with 3.0% additional water achieved the highest discharge capacities of 0.289 mAh/$cm^2$ and 0.399 mAh/$cm^2$, respectively. The samples with 0.5% additional water for those electrolyte compositions were not far behind, though. They

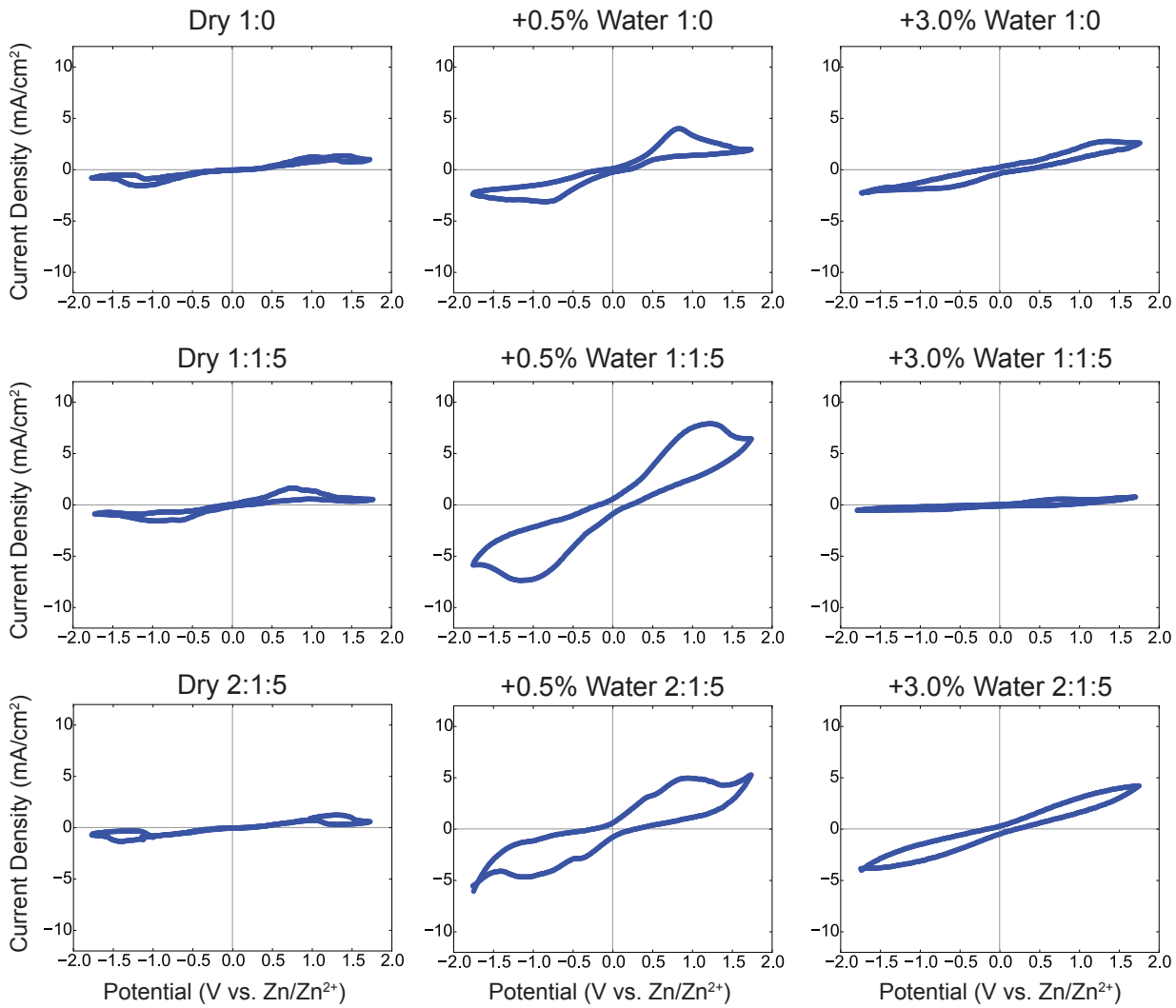


Figure 5.4: Reduction-oxidation peaks associated with each electrolyte composition with additional water on cycle 6.

achieved 0.242 mAh/cm$^2$ and 0.345 mAh/cm$^2$ for the [1:15]2:1:5 and [1:15]1:0 compositions respectively. The [1:15]1:1:5 samples, though, did not show the same trend. The samples with 0.5% water added showed a marked improvement in their discharge capacity, although their cycle lives were dramatically lower. Upon investigating their accumulated discharge capacity over the entire cell lifetime, each group of cells performed very similarly with around 1 mAh/cm$^2$.

The cells with the least amount of water present, despite exhibiting the lowest capacities, had the longest cycle lives and the most consistent performance across multiple cells. The dry [1:15]1:1:5 cells had an average discharge capacity of 0.0246 mAh/cm$^2$ where the maximum was 0.0296 mAh/cm$^2$ and the minimum was 0.0207 mAh/cm$^2$. The dry [1:15]2:1:5 cells achieved approximately twice discharge capacity with an average of 0.0529 mAh/cm$^2$, a maximum of 0.0573 mAh/cm$^2$, and a minimum of 0.0442 cm$^2$. All of these cells lasted through 50 cycles and, as visible in Figures 5.6 and 5.7, had virtually no drop in capacity and very stable efficiencies over the number of cycles tested.

As mentioned previously, not a single dry [1:15]1:0 cell could be cycled at all. None could be charged at the start of cycling to attain the 1.8 V like all of the other samples. The same cathode material was used for all of the cells and every dry sample for the dry [1:15]1:0, dry [1:15]1:1:5, and dry [1:15]2:1:5 compositions was produced within the same 24 h period. It is unknown whether this was a function of the polyolefin separator material, the lack of water, or unforeseen problems with the electrodes.

When investigating the best performers for each composition in Figures 5.6 and 5.7, the most visible trend was that cells with the highest capacities lasted the fewest number of cycles. They also tended not to have stable efficiencies over their lifetimes. Conversely the lowest capacity cells lasted the greatest number of cycles and had much more stable efficiencies. While not necessarily common throughout all of the best performers, when the capacity changed dramatically from cycle to cycle it seemed to indicate that the cell would soon fail. This was the case for the best samples for the [1:15]1:0 sample with 0.5% additional water and [1:15]2:1:5 sample with 3.0% additional water.

### 5.4.5 Postmortem Cell Analysis

After conducting cycling tests, several cells were opened and the Zn foil within was investigated with an SEM as shown in Figure 5.8. Note that each piece of foil was dabbed dry with a Kimwipe before imaging because the ionic liquid on the surface would not reflect electrons to produce an image in the SEM.

The foil from the cell with a [1:15]2:1:5 GPE and 3.0% additional water had a very rough surface with many zinc oxide mesocrystals. With the cells operating between 1.8 V and 1.0 V, it is possible that some amount of the water electrolyzed releasing hydrogen and oxygen. The generation of zincate and zinc oxide from the hydrogen and oxygen could explain the appearance of these structures, although they were not visible in any of the other samples investigated. At such a high density, the impedance of the cell could have risen to the point where the oxidation of zinc would become unfavorable. Conducting EIS as the cells cycle

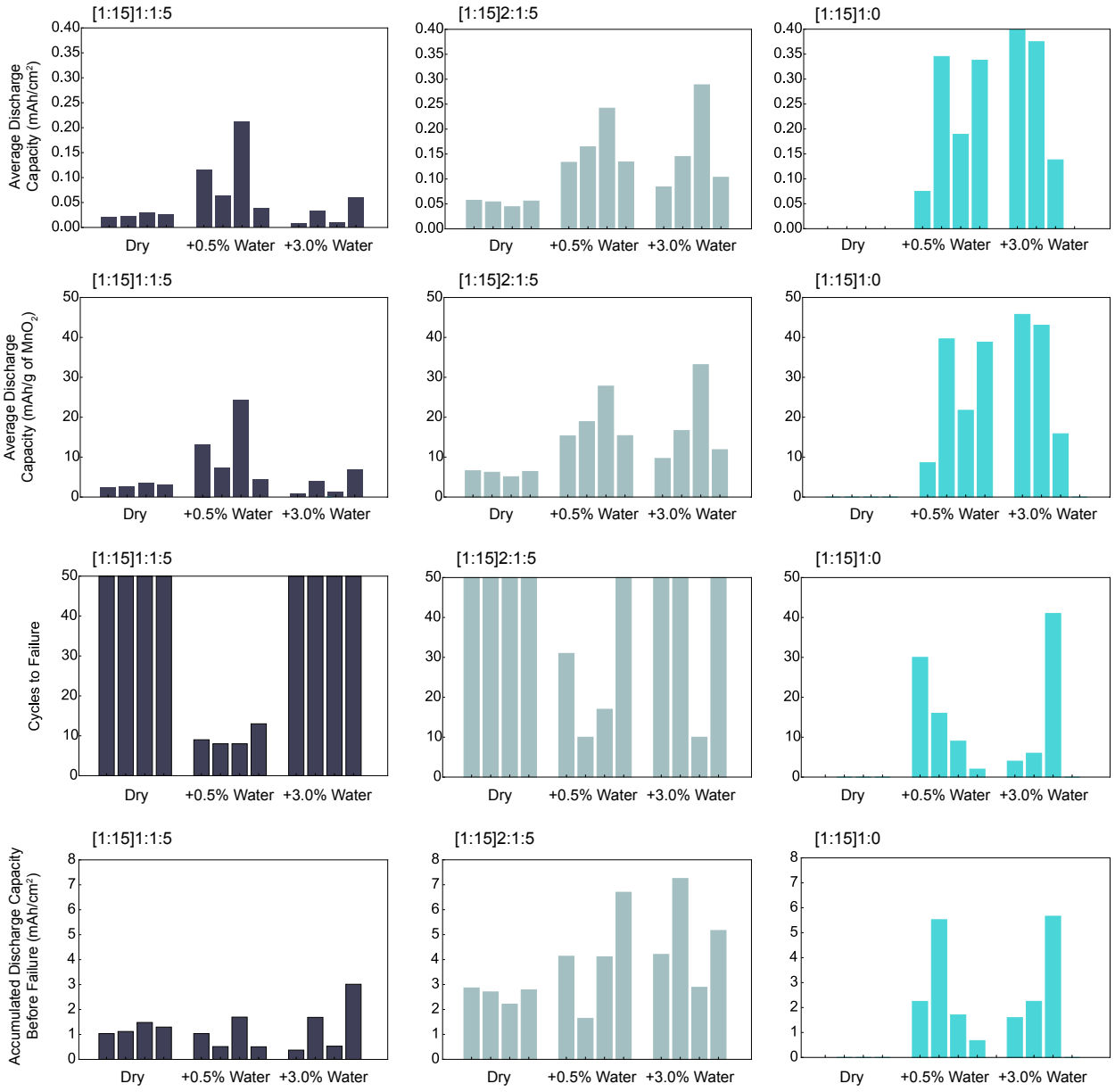


Figure 5.5: Comparison of average discharge capacity per unit area, average discharge capacity per gram of $MnO_2$, cycles to failure, and accumulated discharge capacity per unit area for 4 samples of each electrolyte and GPE composition with varying water content.

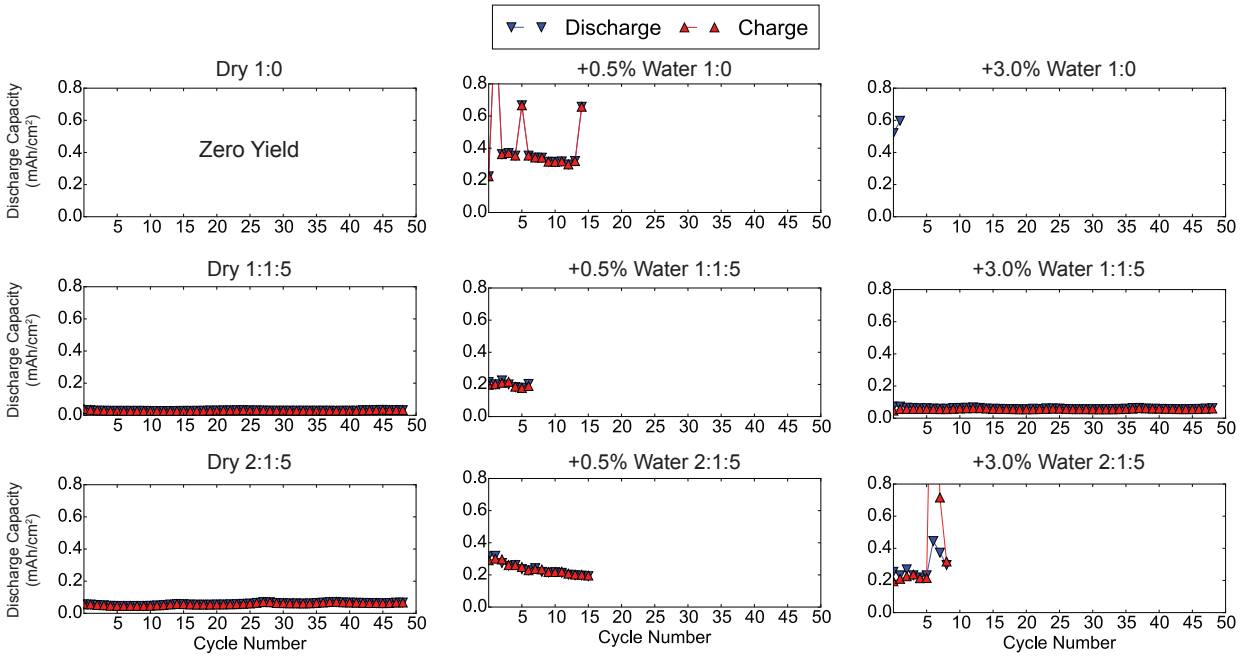


Figure 5.6: Per-cycle performance for the cells that attained the highest discharge capacities for each electrolyte composition with additional water.

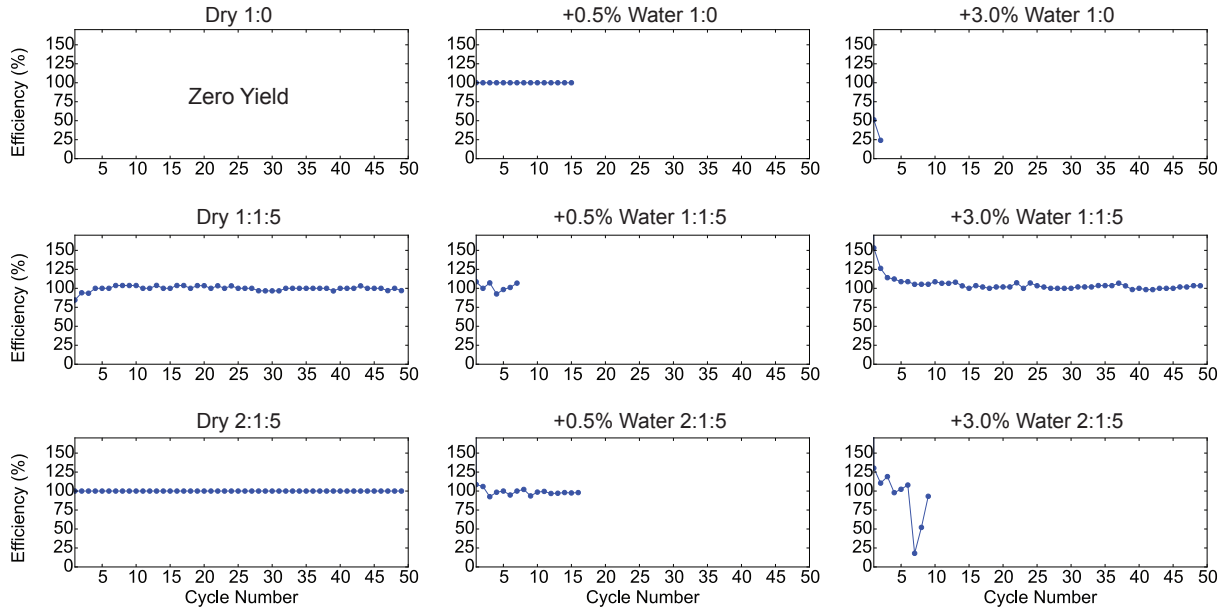


Figure 5.7: Coulombic efficiencies (charge out/charge in) for cells that attained the highest discharge capacities for each electrolyte composition with additional water.

would confirm this hypothesis. As discussed previously, the cells with 3.0% additional water in the electrolytes attained the highest discharge capacities. If the reactions that produced zincate and zinc oxide also produced electrons, whether directly or through additional side reactions, then that could account for the better performance.

The foil from the cell with the GPE composition of [1:15]2:1:5 but with only a minimal amount of water had the surface with the fewest features that would indicate reactions. The striations within the foil due to zinc dissolving and replating are plainly visible and did not appear to have undergone any significant changes. The blemishes were likely to be ionic liquid that, as previously stated, did not reflect sufficient electrons to produce a clear image. Due to being a liquid they would appear cloudy in the image, as was likely the case here. There was the appearance of particulates on the surface, though. It is unknown whether these were from the Kimwipe or not but they were plainly visible and in locations without the blemishes. The low discharge capacity for all cells using this GPE composition would indicate few reactions of the zinc foil and these images seem to confirm that.

The surface of the zinc foil for the [1:15]1:0 composition with 0.5% water added had the largest change in the surface features. It appeared that either grains within the metal were exposed or new grains formed as the zinc replated. This created a unique pattern all across the surface of the foil. The surface was also very rough, and as a result many pockets of electrolyte were trapped, hence the plethora of cloudy, black spots. Among all of the samples investigated, this exhibited the clearest proof that reactions did occur on the foil as desired.

Finally the surface of the [1:15]1:1:5 composition with 0.5% water added appeared to have the most fouling despite drying with the Kimwipe. A great deal of the surface was dark as a result of some non-reflective substance, potentially electrolyte. This fouling could have been the cause of the low cycle life as shown by all of the cells with this GPE composition. A spectroscopic analysis of the surface is recommended to identify what exactly the substance or substances are.

The other main failure mechanism visible in the cells was the breakdown of the printed $MnO_2$ electrode, as noted previously. Figure 5.9 shows SEM images of two electrodes after cycling. The $MnO_2$ electrode in this figure and the zinc foil in Figure 5.8 were both from the cell with a [1:15]2:1:5 dry composition. The printed electrode did not appear to break down even after 50 cycles.

Conversely, the printed $MnO_2$ electrode from the cell with the [1:15]1:0 + 0.5% additional water GPE began to show some breakdown, as the spherulite-like structures were not as well defined. Again, this correlated well with the zinc foil it was paired with in that the zinc was likely plating and deplating during cycling. Additional experiments with XRD are recommended to identify whether intercalation of $Zn^{2+}$ occurred because such a mechanism could cause significant shape change and breakdown of the electrode.

Electrode breakdown was very prevalent in the cells that contained [1:15]1:1:5 + 0.5% water GPE and the [1:15]2:1:5 dry GPE, as shown in Figure 5.10. The $MnO_2$ electrode in the cell with the [1:15]1:1:5 + 0.5% water GPE almost completely dissolved. This could have been the reason for the fouling on the zinc foil surface. It is interesting to note that not all electrodes experienced this, so the electrolyte, which was common in all of the cells,

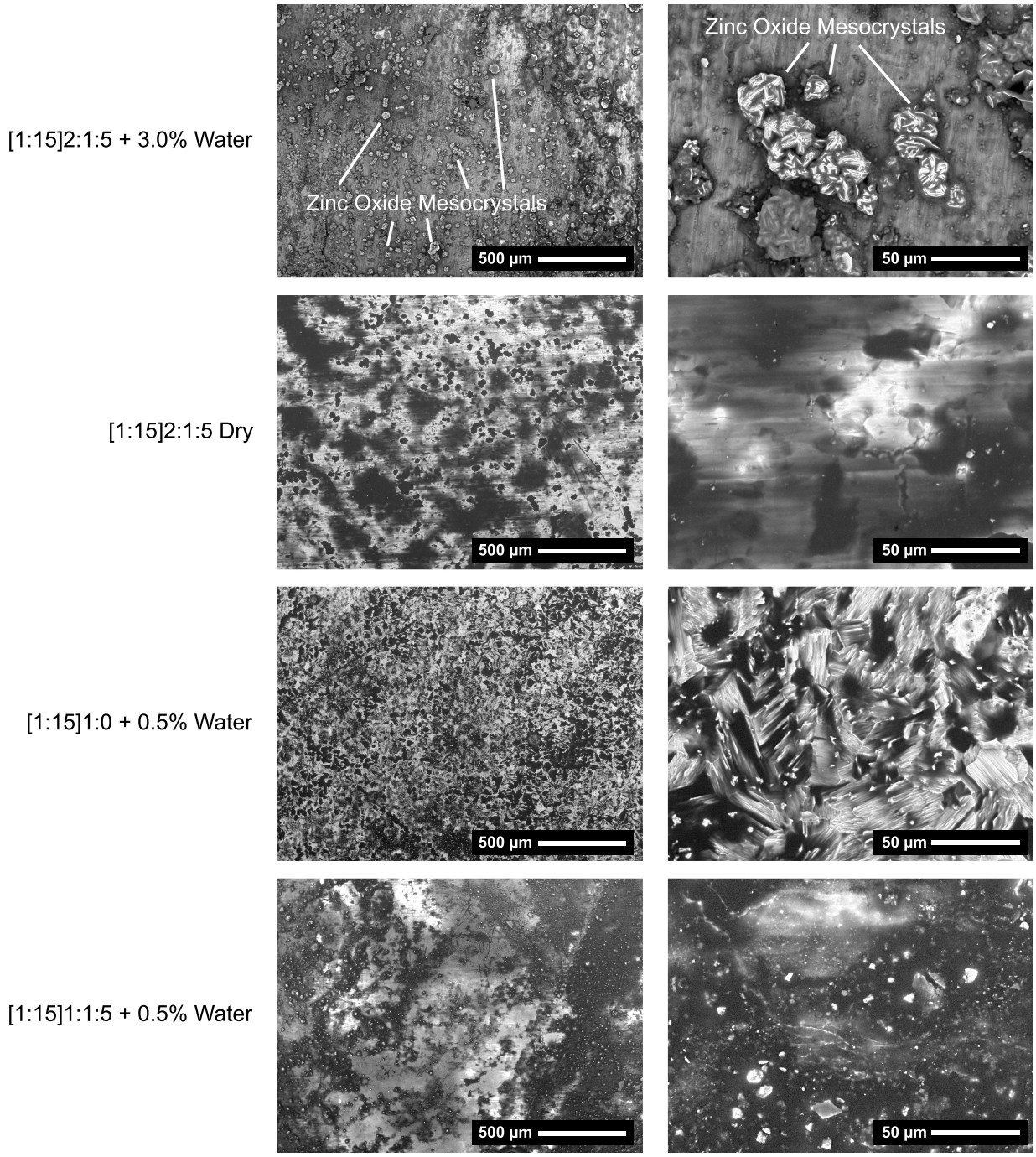


Figure 5.8: SEM images of Zn foil surface from several cells after cycling.

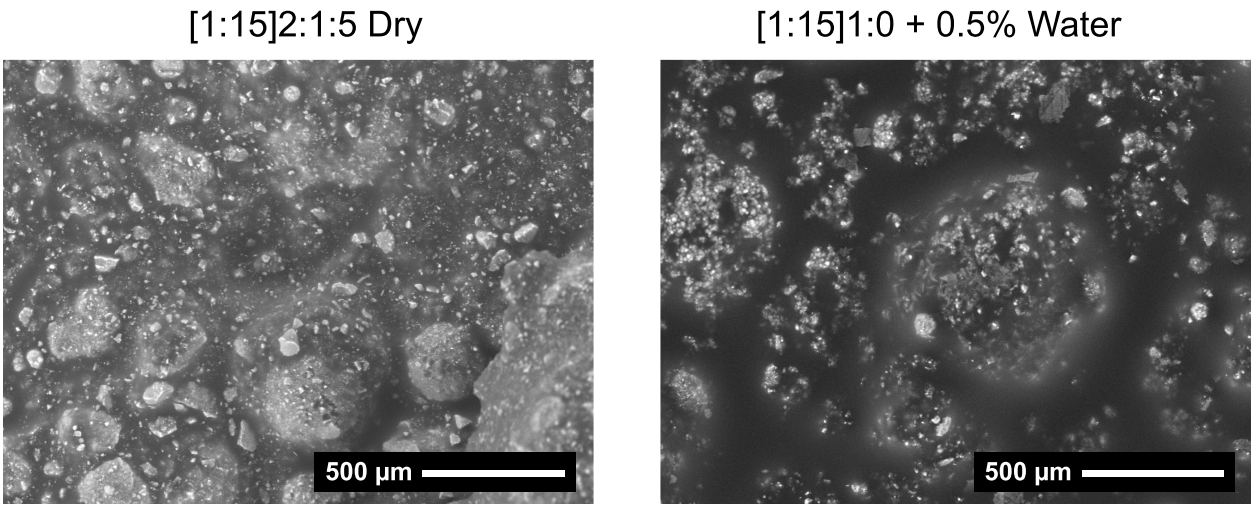


Figure 5.9: SEM images of $MnO_2$ electrode from several cells after cycling.

was likely not the main contributor to the breakdown.

## 5.5 Conclusions

From the results presented, the presence of water did have an impact on cell performance and discharge capacity, although the mechanisms through which it acted are not completely clear. The electrolyte itself is clearly very sensitive to water and has the ability to absorb a great deal of it from the ambient environment. This is exacerbated by the addition of salt to the IL which also affects how much water is absorbed.

Previous research indicated that the presence of water would improve the diffusion coefficient of the electrolyte [86]. Despite this no significant change was present with the ionic conductivity experiments between cells with +0.5% water or +3.0% water. This along with the low ionic conductivity for the dry compositions could have been the result of poor interfaces and differences in sweating. The addition of electrolyte at the interfaces in the conventional Swagelok cell used here could provide conduction pathways outside of the GPE as the electrolyte spreads out over the surfaces. To accurately test the ionic conductivity with wetted interfaces, a new apparatus should be developed that ensures that the electrolyte will not leak out around the edges of the GPE. The results can then be compared with those here to determine the influence of composition and concentration of water on the ionic conductivity.

The results from cyclic voltammetry do clearly indicate that an optimal concentration of water in the electrolyte should exist where the redox peaks are highest. The electrolytes with +0.5% water had the highest peaks overall, but this may not be the optimal composition. Additional points between full saturation and the dry compositions must be created to

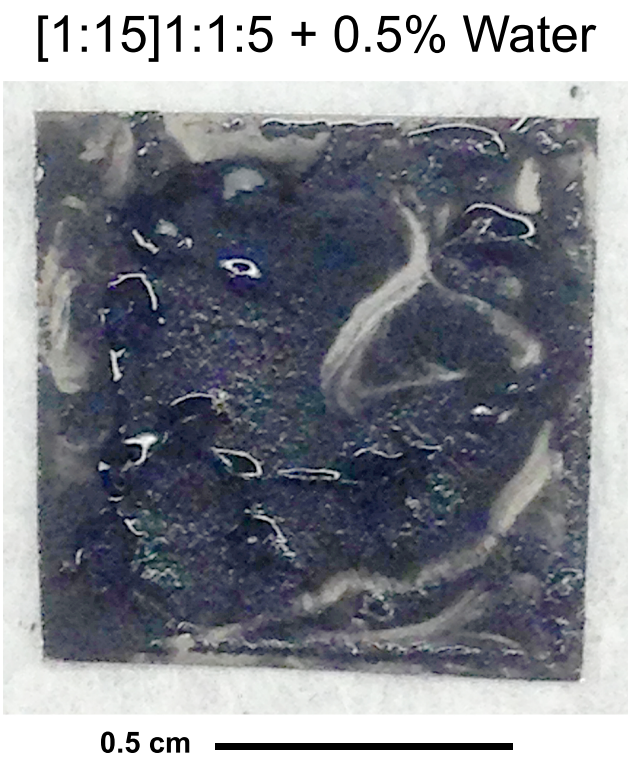


Figure 5.10: Photograph of $MnO_2$ electrode from cell with [1:15]1:1:5 + 0.5% water GPE after cycling.

optimize the GPE composition.

For cell cyclability, the presence of water and the use of a GPE or polyimide separator had the largest effect on discharge capacity and cycle life. When very little water was present in the electrolyte and no PVDF-HFP was used, not a single cell would cycle. With the same dry electrolyte composition but with PVDF-HFP added, cells did cycle and had very consistent capacities. The cells with additional water, though, did not have consistent performance among the number of samples tested. Much larger data sets for each group are recommended to determine variability within a composition.

Overall it is highly recommended to continue investigating the effect of producing cells within an ambient laboratory environment. An optimal electrolyte composition should be determined before conducting other experiments to determine variability within groups of cells.

# Chapter 6

# Component Optimization and Integration

## 6.1 Introduction

## 6.2 Material Selection

### 6.2.1 $MnO_2$ Electrode Ink Composition and Manufacture

The breakdown of the printed $MnO_2$ electrodes made from a composition A ink, as shown in the postmortem analyses, likely indicated that there was too little PVDF-HFP to keep the material together during cycling. Thus a new ink, composition C, was produced in the hopes of improving cell stability and cyclability. As a first pass at empirical optimization, the amount of PVDF-HFP was doubled from 4% to 8% while maintaining the 15:1 mass ratio between the $MnO_2$ and AB with the knowledge that composition B with 30% PVDF-HFP could not produce any usable cells, most likely because there was too much polymer present. The final composition is presented in Table 6.1. Composition C was then made using the same methods of weighing, vortex mixing, sonication, and gel production as noted in Section 3.2.1. Upon completion of the ink, it was printed on 25.4 $\mu$m-thick stainless steel foil using the method of stencil casing detailed in Section 3.2.3. Stencil casting was used for manufacturing because of the consistent surface features it produced.

### 6.2.2 Electrolyte Composition and Manufacture

The [1:6.5] mass ratio of $Zn(OTf)_2$:[BMIm][OTf] was found to have the highest redox peaks and contributed to the highest capacity cells of all of the electrolyte and GPE compositions investigated. GPEs with a mass ratio of 2:1:5 for electrolyte:PVDF-HFP:NMP also consistently produced cells with higher discharge capacities, cycle lives, and ionic conductivities than the 1:1:5 samples or even those without any PVDF-HFP. Thus to investigate a large

Table 6.1: Ratio of all solid materials for first pass optimization of $MnO_2$ printed electrode. NMP was added to achieve the desired rheology for printing.

| **Composition C** | |
|---|---|
| **Material** | **Mass %** |
| $MnO_2$ | 86.25% |
| AB | 5.75% |
| PVDF-HFP | 8% |

number of cells with an optimal electrolyte composition, the [1:6.5]2:1:5 GPE was selected. Taking into account the environment, the results in Chapter 5 indicated that the presence of some water within the electrolyte was beneficial, although too much would be detrimental to discharge capacity. Thus dry [BMIm][OTf] was used with $Zn(OTf)_2$ from ambient conditions. They were mixed at ambient conditions to absorb some quantity of moisture, although they were not left exposed to the laboratory air for any extended period of time to prevent full saturation. The electrolyte and GPE were manufactured using the procedure discussed in Section 4.3.2. A 15.88 mm (0.625 in.) diameter punch was then used to cut out each disc of GPE for assembly within each coin cell.

## 6.3 Design of Experiments

It was important to determine the reproducibility and distribution of performance across a large set of data after discovering a set of optimal compositions from previous investigations. Thus a set of battery components were produced at the same time with the same materials in the same environment. The two battery testers available each had 8 channels, thus at least 16 cells would have to be produced. Despite the knowledge and advancements presented in the previous chapters, many aspects of the manufacturing process still could not be controlled. Some factors include thermal gradients during drying as a result of placement within the oven, printed electrode surface morphology between prints, particulate distribution, and gel polymer morphology between casts.

In an effort to prevent bias of the results, random selection and random assignment were used. Thirty-two printed $MnO_2$ electrodes of composition C were produced from four stencil casts, each with eight 1 $cm^2$ squares. They were dried simultaneously in a sealed vacuum oven at ambient pressure at 80 °C overnight, as discussed in previous chapters. Twenty-eight casts of [1:6.5]2:1:5 were produced and also dried in a sealed vacuum oven at ambient pressure at 80 °C overnight, as discussed in previous chapters. After removal from the oven, they were allowed to cool to room temperature for several hours before assembly.

The central disc of the GPE was cut with the punch and the excess outer ring was removed. In order to reduce waste, the coin cell cans were thoroughly cleaned and dried with acetone and Kimwipes and used to produce the cells. In the can, a printed $MnO_2$

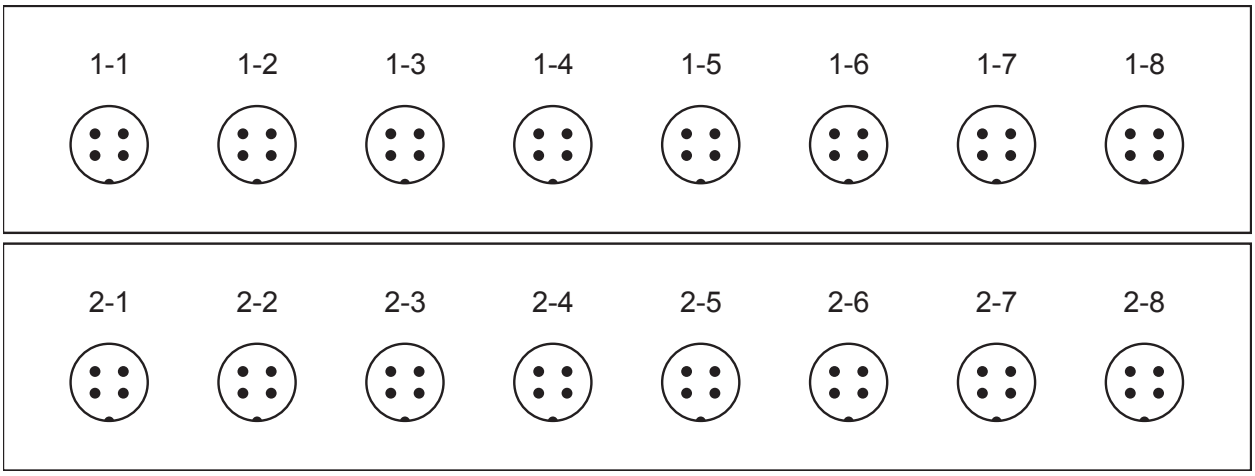


Figure 6.1: Battery tester setup and numbering convention.

electrode was randomly chosen from the set of thirty-two and wetted with 3-4 droplets of [1:6.5] electrolyte. A [1:6.5]2:1:5 GPE was then randomly selected and assigned to that printed $MnO_2$ electrode. The cell was then completed as a wet stack coin cell as per the methods discussed in previous chapters, although only one spacer was used instead of two to account for the thicker GPE.

From the resulting cells, their OCV was checked to ensure they exhibited a potential above 1.0 V. Sixteen cells were then randomly selected and assigned to channels 1-1 through 2-8 as shown in Figure 6.1. The remaining 9 were used to test the utility of this composition via integration with a commercial off-the-shelf microcontroller (Texas Instruments, MSP430G2231).

### 6.3.1 Statistical Functions

The variability within the data was captured with the mean and standard deviation. The average discharge capacity statistics were generated over the 314 cycles from all of the cells, whereas the cycles to failure and accumulated discharge capacity statistics were determined from the results of the 16 cells. Note that the standard deviation was defined by

$$s = \sqrt{\frac{1}{N-1}\sum_{i=1}^{N}(x_i - \bar{x})^2} \tag{6.1}$$

where N was the number of samples, $x_i$ was the value of the metric at index $i$, and $\bar{x}$ was the mean value of the dataset. N-1 was used instead of N because of the small number of samples within the dataset. For completeness, the mean was defined by

$$\bar{x} = \frac{x_1 + x_2 + ... + x_n}{N}. \tag{6.2}$$

## 6.4 Results and Discussion

### 6.4.1 Component and Cell Characteristics

The primary surface profiles of four stencil-printed $MnO_2$ electrodes were acquired in order to determine their surface features. The surfaces for samples 1 through 4 are shown in Figure 6.2. Despite a slight depression in sample 1, all four electrodes had randomly distributed peaks as expected from stencil printing. They also had very few holes or extreme variations across the surface as determined by visual inspection. These qualities were confirmed by the roughness and waviness metrics as described in Tables 6.2 and 6.3. Over the investigated areas, the roughness values were all within 0.56 $\mu$m of each other in both the inline and orthogonal directions, which indicated relatively smooth surfaces. The values were also lower than any of the results for compositions A or B by approximately 1 $\mu$m. The waviness values were also lower than the compositions A or B by an even larger margin of 3 to 4 $\mu$m.

Table 6.2: Arithmetic average and root mean square roughness ($R_a$, $R_q$) and waviness ($W_a$, $W_q$) of stencil-printed, composition C, $MnO_2$ electrodes inline with the scanning direction with the microscope. Note that all units are in $\mu$m.

| **Sample** | $\mathbf{R}_a$ | $\mathbf{R}_q$ | $\mathbf{W}_a$ | $\mathbf{W}_q$ |
|---|---|---|---|---|
| 1 | 2.198 | 3.373 | 18.26 | 22.51 |
| 2 | 2.504 | 3.784 | 16.36 | 20.95 |
| 3 | 2.758 | 4.090 | 17.02 | 21.38 |
| 4 | 2.311 | 3.523 | 15.16 | 19.22 |

Table 6.3: Arithmetic average and root mean square roughness ($R_a$, $R_q$) and waviness ($W_a$, $W_q$) of stencil-printed, composition C, $MnO_2$ electrodes orthogonal to the scanning direction with the microscope. Note that all units are in $\mu$m.

| **Sample** | $\mathbf{R}_a$ | $\mathbf{R}_q$ | $\mathbf{W}_a$ | $\mathbf{W}_q$ |
|---|---|---|---|---|
| 1 | 2.341 | 3.540 | 15.50 | 20.03 |
| 2 | 2.547 | 3.891 | 16.14 | 20.68 |
| 3 | 2.453 | 3.844 | 15.70 | 19.83 |
| 4 | 2.274 | 3.534 | 15.28 | 19.34 |

The electrolyte was tested on the Karl Fischer titrator to determine the amount of water that was present after manufacturing. The results shown in Table 6.4 indicated that less water was present than in the sample that was dried in the vacuum oven as discussed in Section 5.4.1. This meant that the electrolyte could not be dried using conventional heating

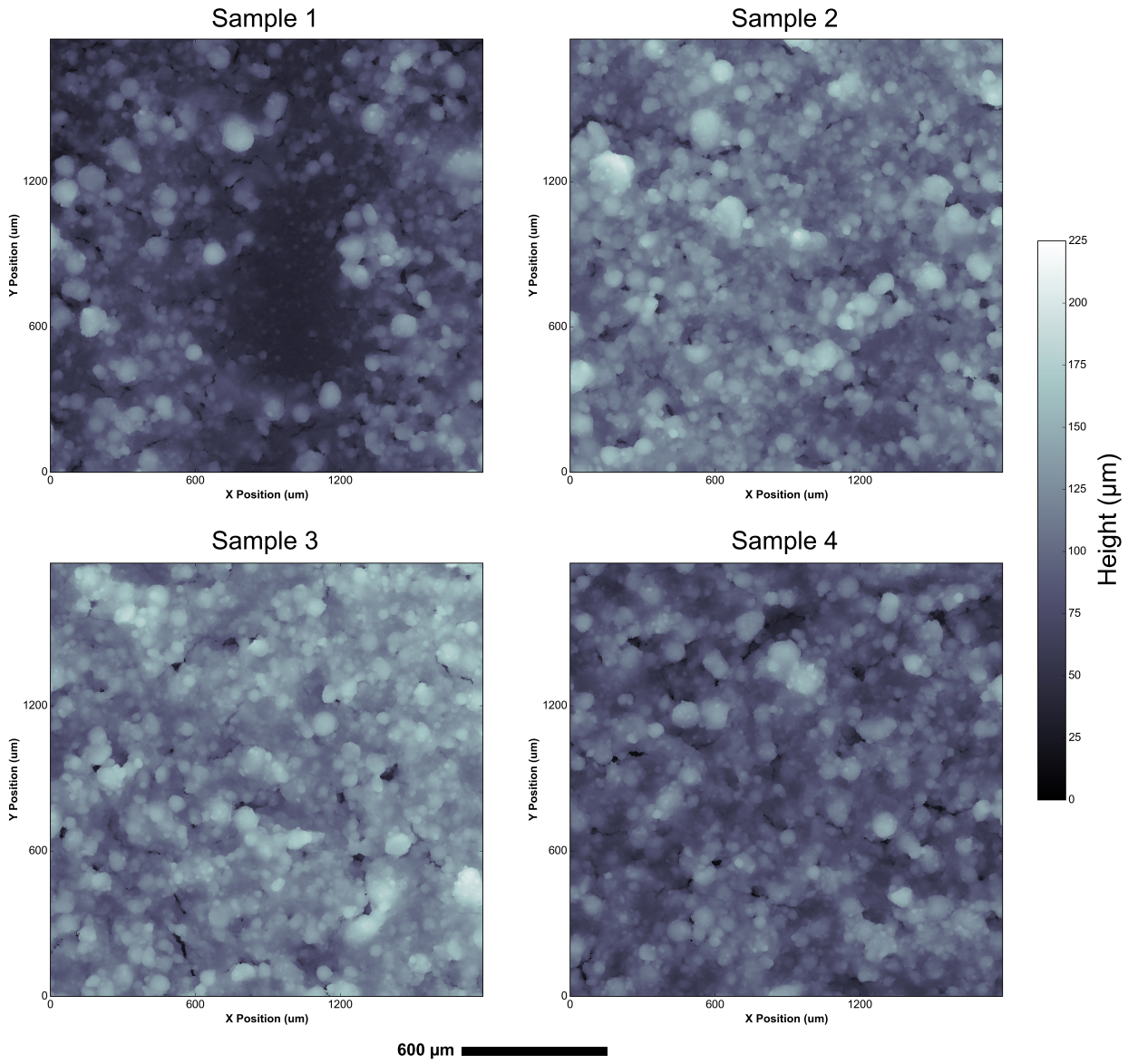


Figure 6.2: Primary surface profiles of stencil-printed $MnO_2$ electrodes with composition C.

Table 6.4: Amount of water present in the electrolyte with a $Zn(OTf)_2$:[BMIm][OTf] mass ratio of [1:6.5] produced in ambient conditions as determined by Karl Fischer titration. Note that the units are mg of $H_2O$ per gram of solution.

| Sample | Water Content |
|---|---|
| 1 | 7.6740 |
| 2 | 8.1230 |

once it passed a specific point of saturation or the vacuum within the oven was not low enough and some moist air was present to resaturate the solution.

For the cells made with these components, the OCV was found to be between 1.39 V and 1.42 V with the majority biased toward 1.4 V and above. The yield for the cells made was also 100%, that is every cell made had a high OCV and cycled on the battery testers.

### 6.4.2 Cell Cyclability

The 16 cells with the optimized components were cycled until they reached 50 cycles or failed. The printed $MnO_2$ electrodes, GPEs, and full cells were all manufactured in large batches simultaneously. Despite this the performance was expected to vary somewhat from cell to cell. The results of the cycle tests are shown in Figure 6.3. Cell 2-5 exhibited the highest average discharge capacity of 1.047 mAh/cm$^2$ over 9 cycles before failing resulting in a summed discharge capacity over all of the cycles of 9.421 mAh/cm$^2$. Cell 2-3 exhibited the lowest average discharge capacity of 0.346 mAh/cm$^2$ yet had a summed discharge capacity of 17.30 mAh/cm$^2$. As noted in previous chapters, cells with lower capacities tended to have longer cycle lives and thus higher accumulated discharge capacities like with cells 1-1 and 2-3 for example.

The cycle capacities for each individual cell are presented in Figure 6.4. As seen from experimental results in previous chapters, the cells began cycling with a high capacity only to have decreased performance as they continued. However after the first few of cycles, the capacity seemed to plateau for many of the cells that survived past those initial cycles. It is unknown what caused the outlier cycles in cells 1-1, 1-2, 1-3, and 1-5. The errant cycles in 1-2, 1-3, and 1-5 seemed to indicate that the cells would soon fail, which they did, although that was not the case for cell 1-1. After that cycle it continued along the same discharge trend as before.

In addition to the cycle capacities, the coulombic efficiencies were also generated, as shown in Figure 6.5. Aside from those few cycles noted previously, the cells all exhibited efficiencies at or nearly at 100%. This likely indicated that a mechanism other than side reactions was the cause of the failure of the cells, of which the postmortem analyses will investigate.

Figure 6.6 shows the data for each metric after being sorted to provide a clearer basis

Table 6.5: Statistics for performance data of 16 optimized cells.

| | **Mean** | **Standard Deviation** |
|---|---|---|
| Average Discharge Capacity (mAh/cm$^2$) | 0.551 | 0.180 |
| Cycles to Failure | 19.63 | 14.75 |
| Accumulated Discharge Capacity (mAh/cm$^2$) | 10.81 | 5.744 |

of discussion on the distribution of results. The majority of cells had average discharge capacities around 0.6 mAh/cm$^2$, although there were a few outliers at the upper and lower ends as noted previously. The cycle lives and thus the accumulated discharge capacities, though, tended to split into two groups: those with cycle lives above 20 cycles and those below 20 cycles. Six of the 16 cells achieved greater than 20 cycles with cells 1-1 and 2-3 achieving the full 50 cycles.

While the cells here achieved the highest capacities of all of the cells researched, the variability tended to be high as noted by the large standard deviations, as shown in Table 6.5. Again, all materials and components were produced at the same time. This variability could have been the result of many factors. Potential sources included thermal gradients within the oven, surface morphology variations, polymer deposits within the printed $MnO_2$ electrodes, or perhaps even the pressure applied when casting the electrodes with the stencil.

### 6.4.3 Postmortem Cell Analysis

As each cell failed it was taken off of the battery tester, opened, and inspected with and without an SEM. A visual inspection of the cells showed what seemed to be the same failure phenomenon. In every cell, the printed $MnO_2$ electrode delaminated off the stainless steel foil current collector and adhered to the GPE. Micrographs and photographs of this phenomenon are shown in Figures 6.9 and 6.10. This delamination could have been the result of of repeated expansion and contraction of the cathode during cell discharge and charge. By conservation of mass and the assumption that intercalation did indeed occur, the addition of $Zn^{2+}$ ions into the $MnO_2$ lattice was expected to cause a potentially significant volume change in the printed electrode material. An estimate for a 1 mAh discharge and a 100 $\mu$m thick, 1 cm-square printed $MnO_2$ electrode with full intercalation of all $Zn^{2+}$ ions requires a volume change of approximately 24%. The calculations for this estimate are provided in Appendix B. In every case, failure also occurred near the completion of cell recharge between 1.5 and 1.8 V, as shown in Figure 6.7, with the majority between to 1.7 and 1.8 V, where the printed $MnO_2$ electrode would be releasing the last intercalated ions. Thus something critical, possibly the shape change and delamination from intercalation, tended to occur at those potentials on discharge.

It should be noted that the printed $MnO_2$ electrode in the cell on channel 1-4, as shown in Figure 6.9, did not dissolve or visibly mix with the GPE, but through some other mechanism

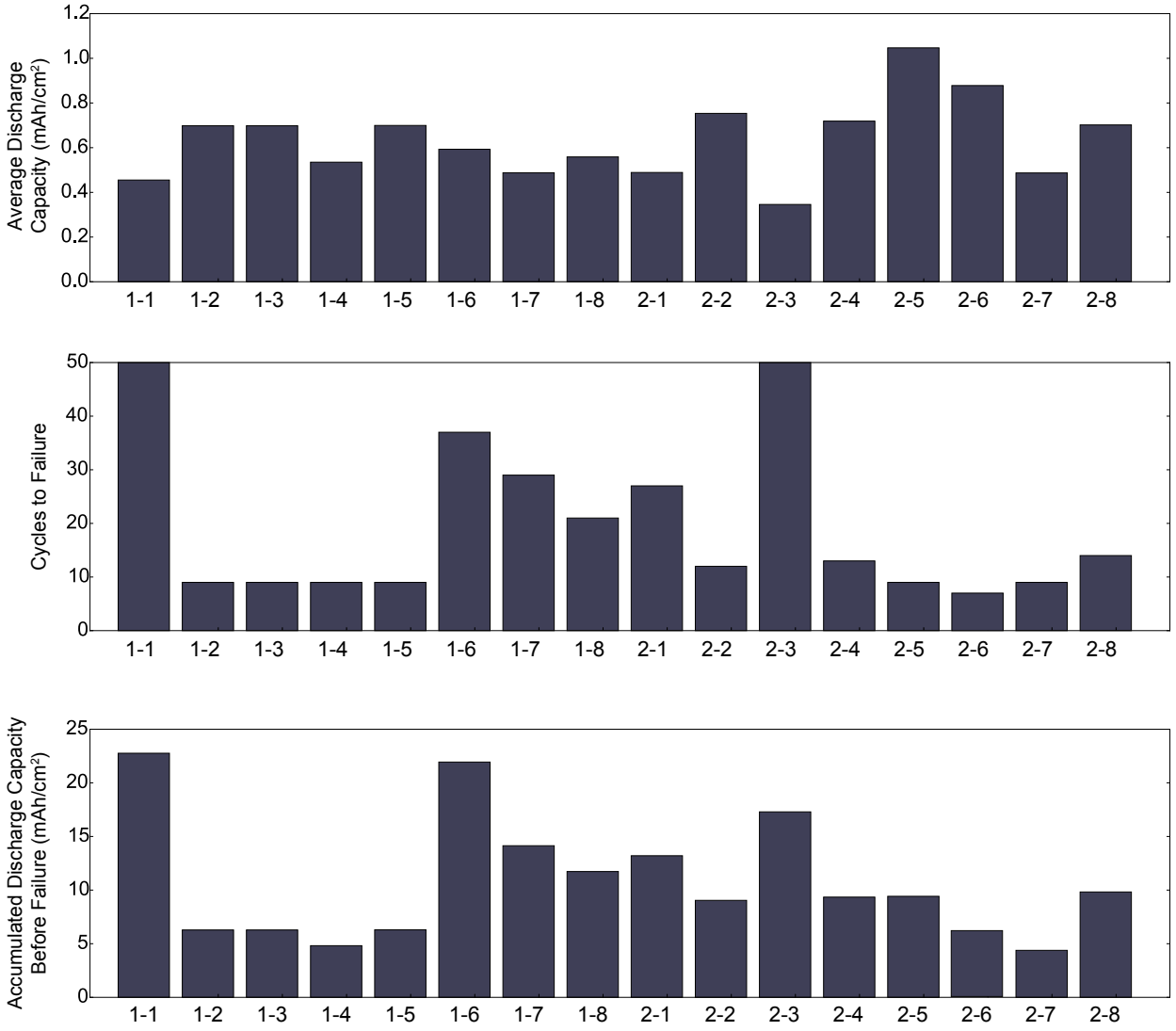


Figure 6.3: Comparison of average discharge capacity per unit area, cycles to failure, and accumulated discharge capacity per unit area for 16 cells each using the same optimized component compositions.

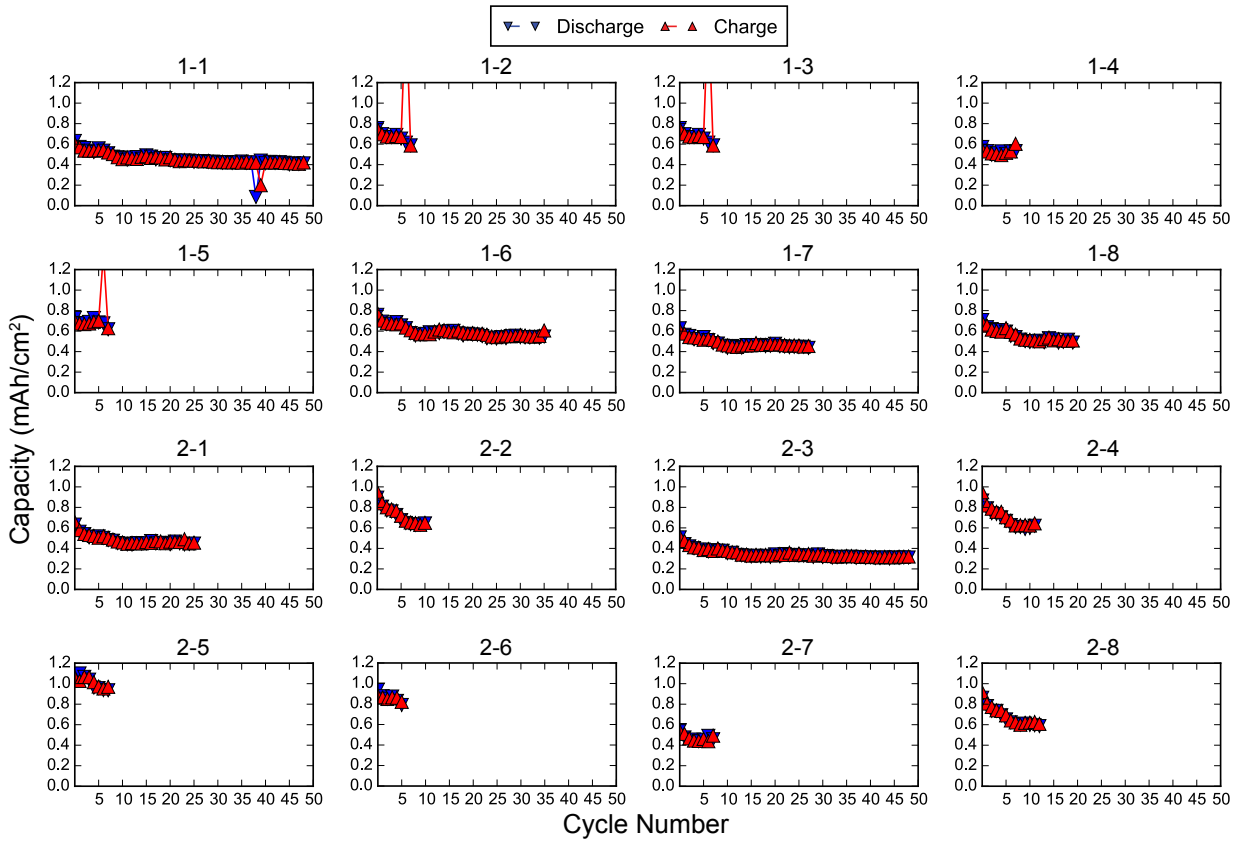


Figure 6.4: Per-cycle capacity for each cell tested.

bonded with it. Two other important things were visible in the images. First, the surface of the printed layer that was in contact with the stainless steel foil appeared to be much flatter than the other surfaces. Second, the polymer seemed to settle slightly and formed a thin layer at the interface with the current collector, noted by the lack of bright particulates at the surface. Both of these factors were likely the result of manufacturing methods, ink composition, and ink mixing. Such a layer could increase the resistance at the interface resulting in large voltage jumps at higher discharge or charge currents.

With several cells, it was difficult to remove the zinc foil from the GPE. In the case of the cell that was on channel 1-3, separating the two components could not be done without excessive force and potentially causing damage. Edge views of this bonded stack are shown in Figure 6.8. The delamination of the printed $MnO_2$ electrode is also apparent on the top of the GPE, as are changes to the surface of the zinc foil. The surface was found to no longer be smooth as the result of repeated cycling. It is also likely that as the zinc replated onto the foil that structures grew into the pores and through the GPE causing the two battery components to bond together.

Interestingly the parts of the delaminated $MnO_2$ electrode matched geometrically with

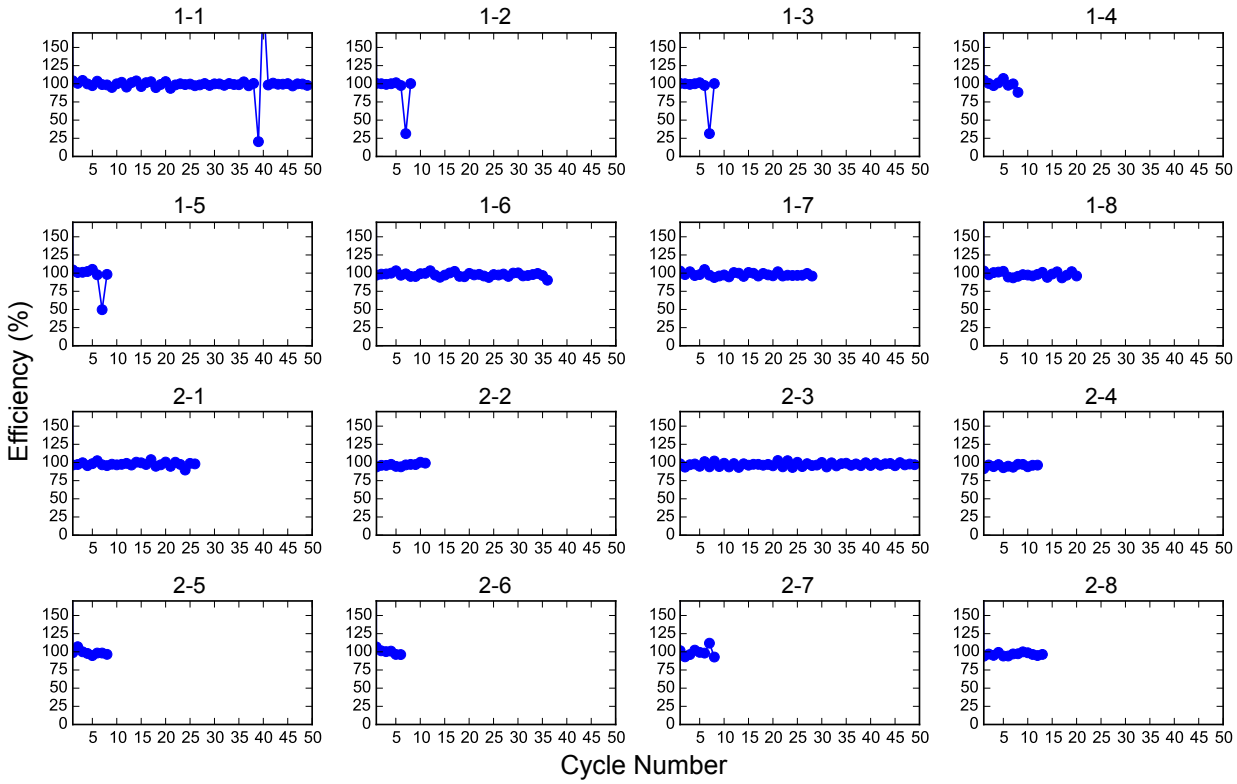


Figure 6.5: Coulombic efficiencies (charge out/charge in × 100) for each cell tested.

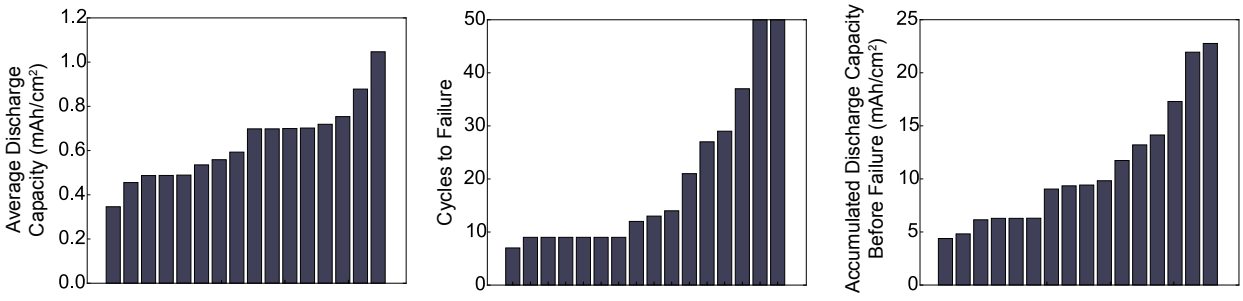


Figure 6.6: Sorted data for each metric to aid in visualization of distribution of data.

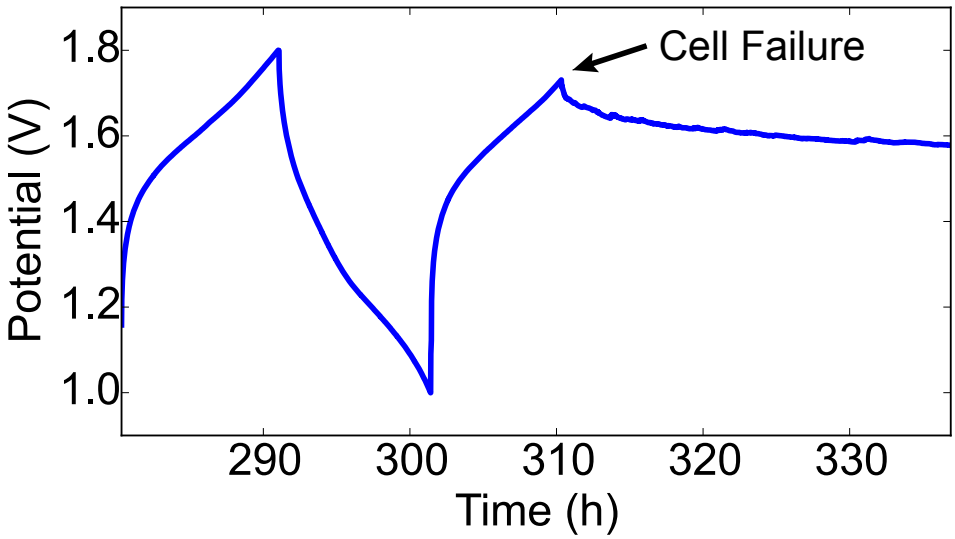


Figure 6.7: Potential during cycling as the cell on channel 2-4 failed on the final cycle.

wear patterns on the zinc foil as shown in Figure 6.10. Despite wet interfaces, reactions tended to occur at certain preferential locations in and around the center as opposed to over the entire surface. The GPEs were known not to have perfectly flat surfaces, which may account for the results shown.

While the surface of the zinc foil shown in Figure 6.9 for the cell on channel 1-4, part of the first group to fail, showed a relatively clean surface despite pitting, the foil from the cell on channel 2-5 with the highest discharge capacity exhibited very different features. Optical inspection showed a much rougher surface, while SEM images showed many different types of growths. While some ZnO mesocrystals formed predominately at the edges, the majority of the surface had bright, rough structures. They were in contact with the zinc and often adjacent to or in contact with locations where striations from replating were visible. These structures were most likely zinc in nature owing to how bright they were in the SEM image. It is possible that they were either the basis or part of dendrites that may have formed. While not tree-like in structure, their presence and structure indicated additional mechanisms at play in the cells. An investigation of the surface of the GPE showed how these structures adhered to and potentially grew into the GPE. There were many bright spots that were partially occluded and blurry, likely because the structures grew into the GPE. The edge view did not clearly show bright structures throughout the GPE, but did show how zinc plates formed on its surface. The act of separating and handling the materials to acquire these images could have removed many of the features that would be indicative of dendrite growth. Despite the appearance of these structures, the results suggested that the zinc could transport through the GPE and not only its pores, as noted by the occluded bright spots on the top view of the GPE.

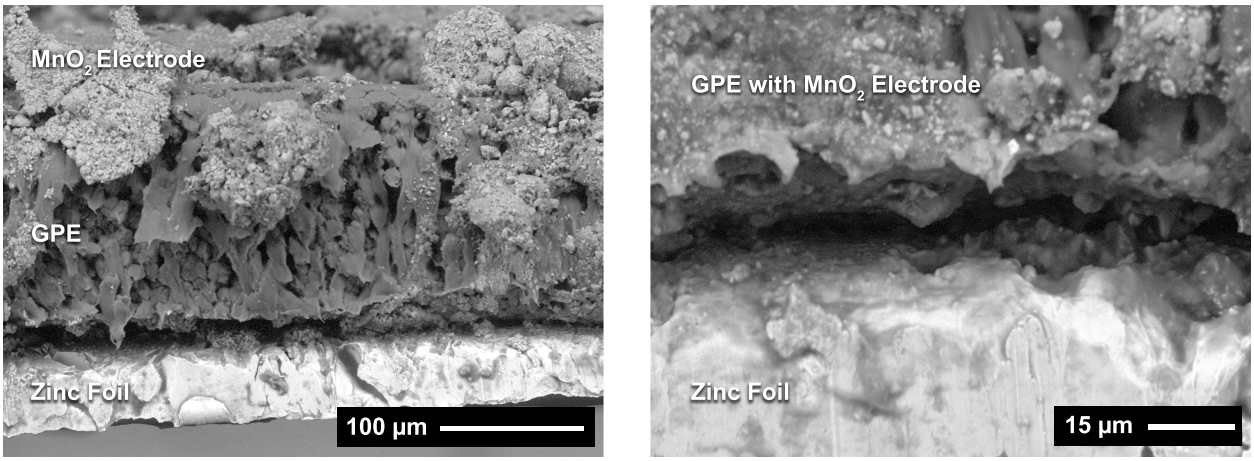


Figure 6.8: SEM images of the edge view of the cell on channel 1-3 where the zinc foil and $MnO_2$ bonded to the GPE.

### 6.4.4 Integration

To test whether the batteries could successfully power commercial electronics, the Texas Instruments MSP430 microcontrol unit (MCU) was used for common use within the laboratory and its low power specifications. With the assistance of another researcher, eight of the nine cells provided for integration were connected in four parallel branches. Two cells in series were connected so each branch achieved at least 2.8 V. Upon assembly the batteries were nearly fully charged, thus they were directly connected without electrochemical modification. For simplicity the cells and MCU were integrated on breadboards with commercial coin cell holders. A multimeter was used to measure the current and confirm functionality. The setup and result is shown in Figure 6.12.

On assembly the MCU was successfully powered and drew 450 $\mu$A. The specification indicated that the MCU would draw 220 $\mu$A for a clock speed of 1 MHz at a potential of 2.2 V. With each branch at 2.8 V, the current draw and clock speed were expected to be higher. As the system was tested, the current did decline by approximately 100 $\mu$A every 15 to 20 s. With the assumption that the impedances of the parallel branches were similar, approximately 112.5 $\mu$A was being drawn from each to provide sufficient current. The cells were previously tested at 60 $\mu$A, approximately half of the current here. The large initial current followed by the rapid decline likely indicated that the assembled experiment approached the limits for reaction kinetics and ion transport within the cells. It is recommended that this be investigated further by adding more parallel branches and measuring the current as it is provided by each branch during testing. The potential of each cell during these tests should also be measured to determine when they achieve the end of their cycle.

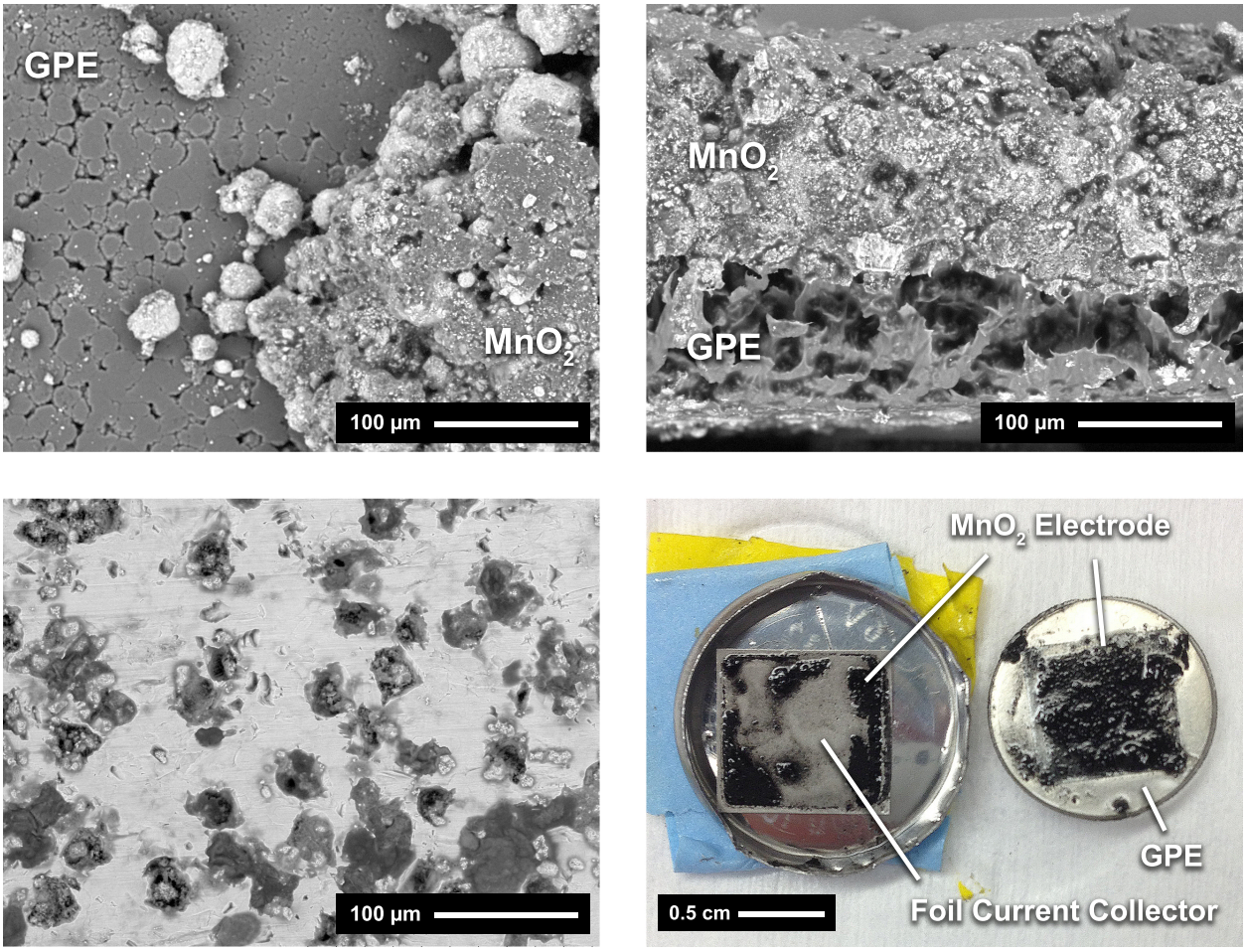


Figure 6.9: SEM images of the components of the cell on channel 1-4. Top left and top right correspond to the top and edge views, respectively, of the $MnO_2$ electrode material on the GPE. Bottom left corresponds to the zinc foil. Bottom right is a photograph of the delamination discovered upon disassembly.

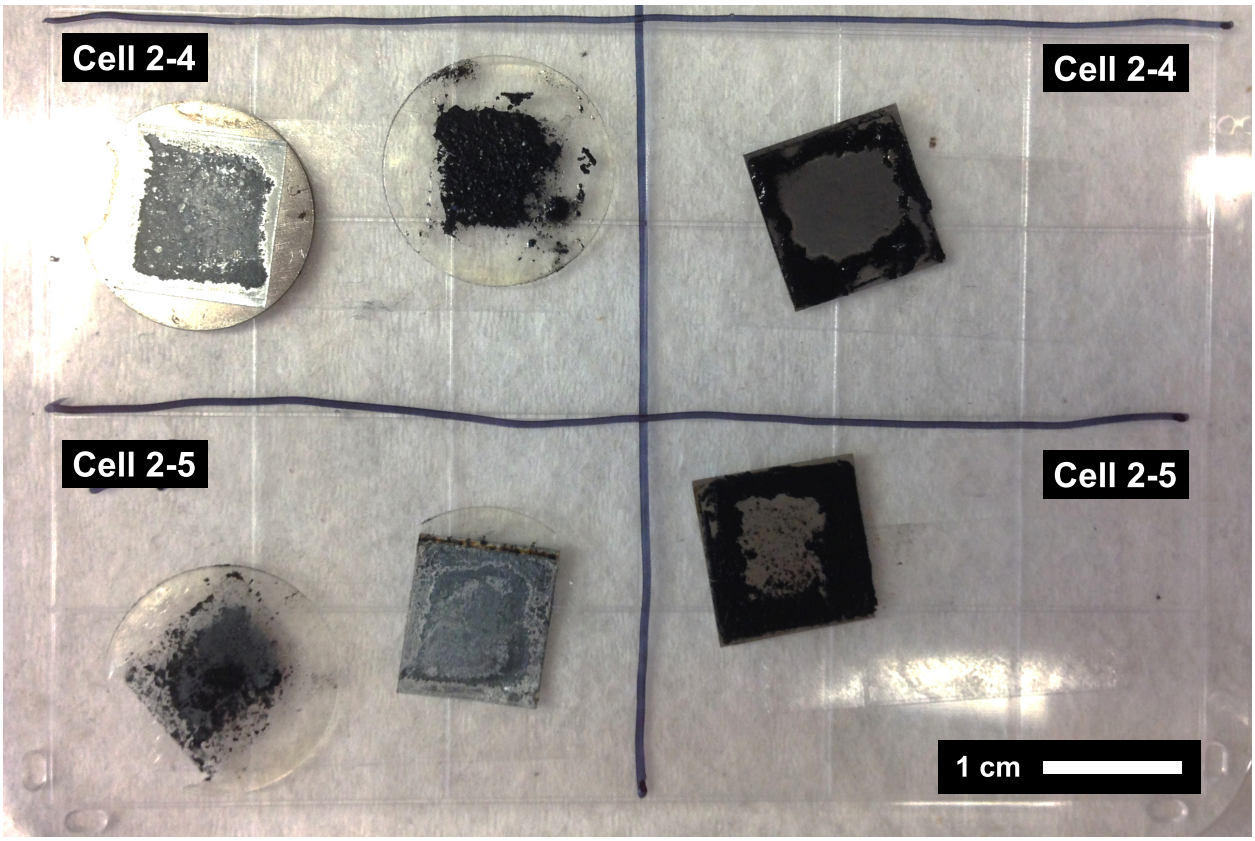


Figure 6.10: Photograph of the components of the cells on channels 2-4 an 2-5.

## 6.5 Conclusions

Investigating the characteristics of the optimal materials resulted in the following results. The surface morphology of the printed $MnO_2$ electrodes made with ink composition C resulted in surfaces with relatively flat features and few to no holes or deep valleys. This was indicated by the average roughness values that were between 2.198 and 2.758 $\mu$m and the average waviness values that were between 15.28 and 18.26 $\mu$m. This type of surface was more desirable because lower quantities of air could be trapped at the interfaces between the GPE and the electrodes. The electrolyte, despite being produced in an ambient environment, contained between 7.67 and 8.12 mg of water/g of solution, lower than the value for the vacuum dried electrolyte discussed previously.

The cells were successfully cycled with a few achieving 50 cycles. The average discharge capacity over all of the cycles was 0.551 mAh/cm$^2$ and a few cells achieved greater than 1 mAh/cm$^2$, although only for a few cycles before failure. The cycle capacities did not vary wildly within any individual cell and followed the expected trend of decreasing capacity with increasing cycle number. The efficiency of the cells was found to be around 100% for virtually all of the cells over all of the cycles. Some variability in the data may have been the result

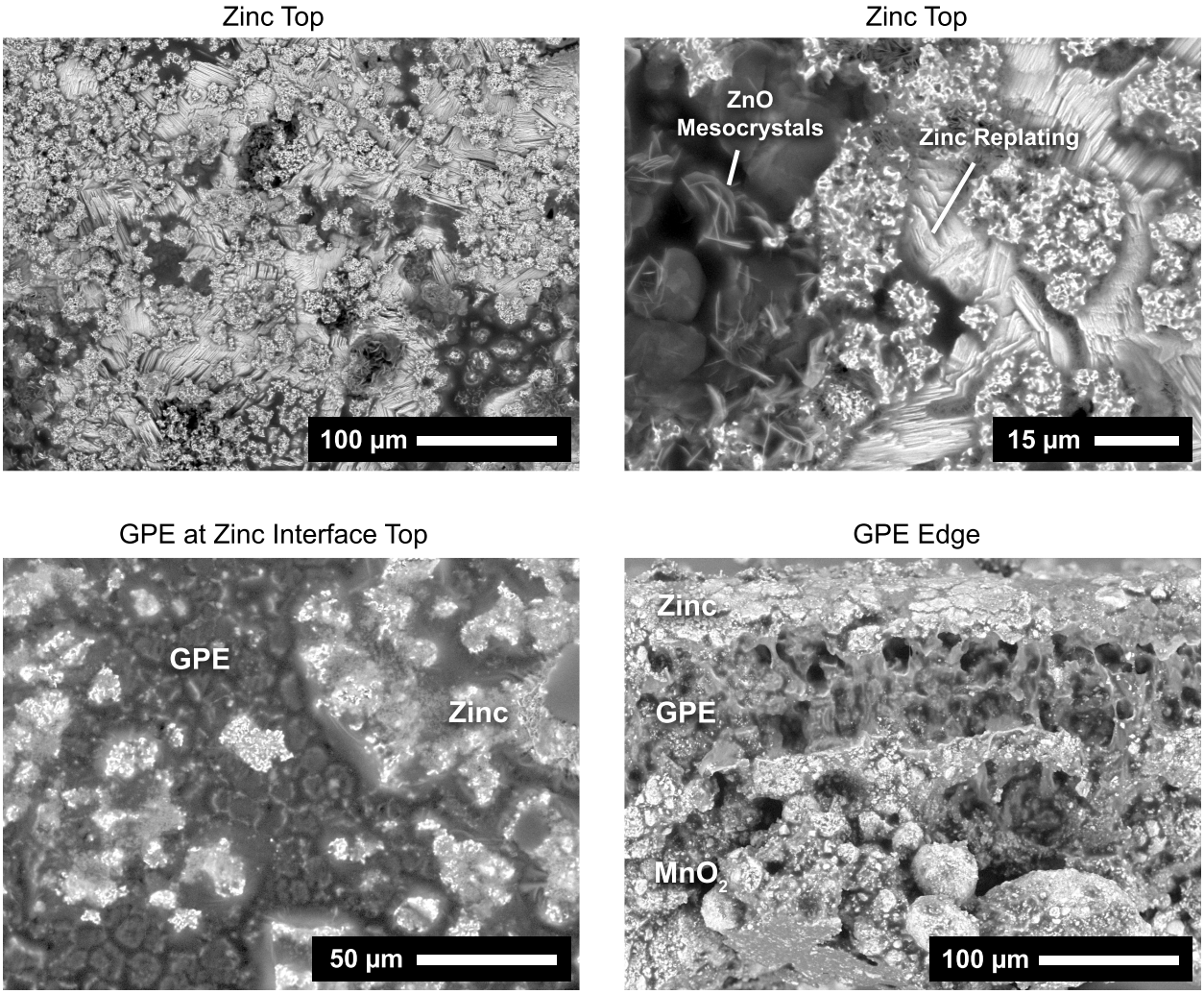


Figure 6.11: SEM images of the surface of the zinc foil, the surface of the GPE in contact with the zinc foil, and the edge of the GPE of the cell on channel 2-5.

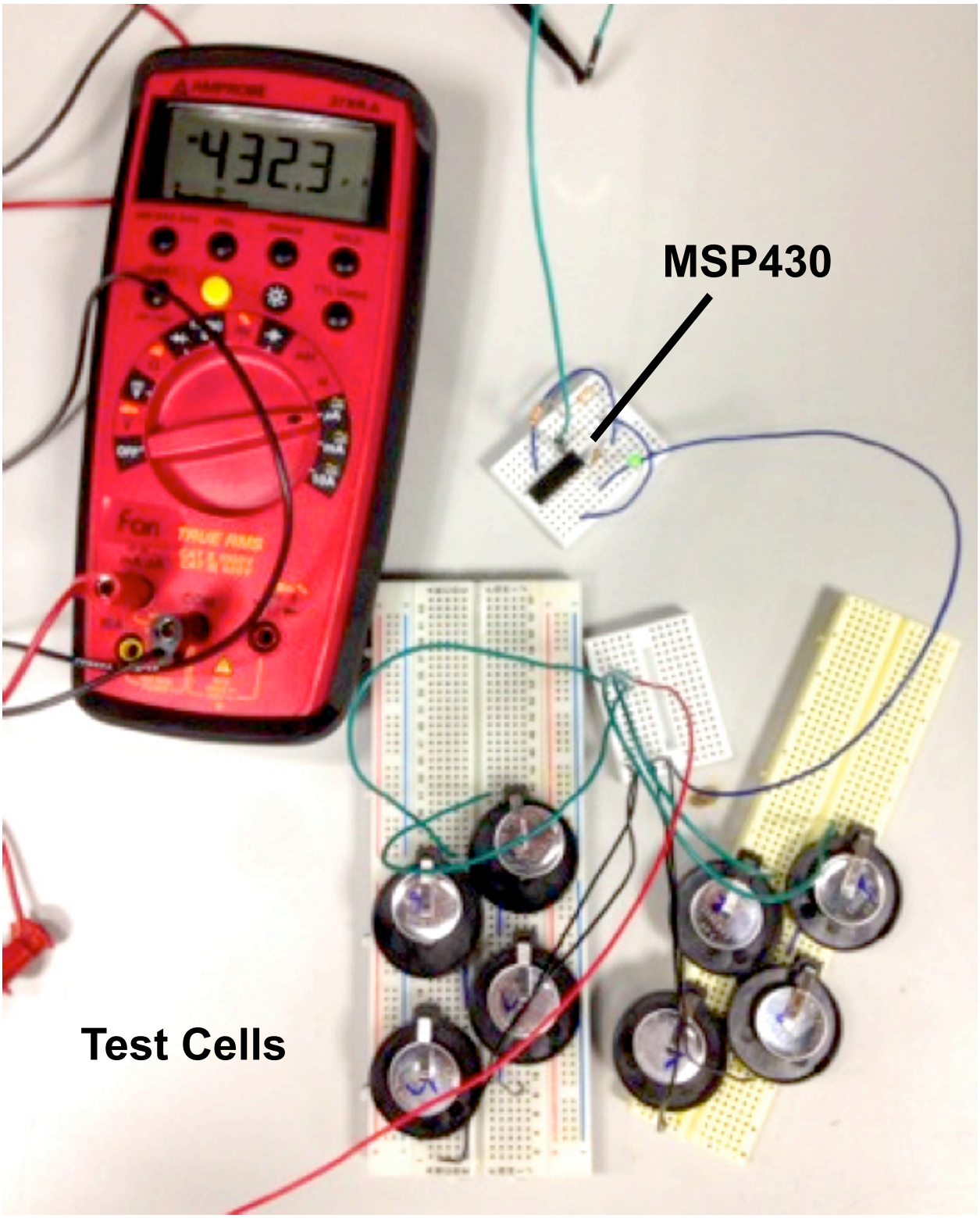


Figure 6.12: Integration setup for eight test cells powering a Texas Instruments MSP430 microcontrol unit.

of temperature changes within the testing laboratory, although that must be investigated further.

The predominant failure mechanism as found over many cells seemed to be delamination of the printed $MnO_2$ electrode. This potentially occurred as the result of repeated expansion and contractions caused by intercalation of $Zn^{2+}$ ions during cycling. The printed electrode surface that was in contact with the stainless steel foil current collector seemed to have a thin layer of PVDF-HFP that had a low quantity of the reactive material. This likely indicated an area of high impedance that could be rectified with an additional ink that would mix with the $MnO_2$ electrode after printing and contain a large quantity of AB. The delamination could be rectified by adding surface treatments to the current collector or roughening the surface to provide better adhesion. Conducting XRD investigations of the printed $MnO_2$ electrode material at several different points of charge and discharge would help elucidate whether intercalation was actually occurring.

Zinc foil from the cells with the highest discharge capacities exhibited dramatically changed surfaces with a large degree of fouling either from zinc replating, the formation of zinc oxide mesocrystals, and the possible formation of dendritic structures. These changes resulted in bonding between the GPE and the zinc foil. SEM images provided visual evidence that zinc structures likely formed within the GPE during cycling which caused the adhesion. These may have been the precursors to dendrites. Conducting XRD on the GPE after cycling could show whether zinc structures did indeed penetrate the film.

# Chapter 7

# Conclusions

Conventional aqueous electrolytes, despite their ubiquity, are poorly suited to the application of printed electronics and flexible batteries. Zinc batteries, though, are well-suited for such applications because of their stability in ambient environments and their high theoretical energy density. The development of printed, ionic liquid-based gel polymer electrolytes has enabled zinc batteries that can be not only integrated with conventional electronics, but also recharged unlike typical alkaline cells. However these advancements brought with them additional manufacturing, environmental, and material factors that must be considered to produce reliable, functional, high-performance batteries.

## 7.1 Achievements

This research has successfully investigated these factors and achieved the following results.

### 7.1.1 Manufacturing Process and Layer Interfaces

- Composition A with 4% PVDF-HFP was brittle but created functional, rechargeable battery cells with discharge capacities on the order of 0.2 mAh/cm$^2$. Conversely composition B with 30% PVDF-HFP was flexible but did not produce a single cyclable cell. Thus too much binder would create non-functional electrodes.

- The rough and wavy surface morphology of the printed electrodes trapped air bubbles at the interface of the electrode and the GPE. These bubbles were unlikely to dissipate during drying, thus creating points of non-ionic conductivity at the interface between the printed $MnO_2$ electrode and the GPE.

- The contact angles between the GPE and the printed $MnO_2$ electrodes did not change much as a result of surface morphology with an average of approximately 24°. More PVDF-HFP in the electrodes did cause a decrease in the contact angle to approximately

10°. Thus the contact between the GPE and the electrodes can be fine-tuned with the quantity of binder in the electrodes.

- The impedance at the interfaces between the GPE and the printed $MnO_2$ electrodes prevented functional, cyclable cells from being produced. This was mitigated by wetting the interfaces with the [BMIm][OTf]-based electrolyte that had a contact angle of 180° with the printed $MnO_2$ electrodes.

### 7.1.2 Electrolyte and Gel Polymer Composition

- The highest mass ratio [1:6.5] of $Zn(OTf)_2$:[BMIm][OTf] generated the lowest ionic conductivities but the highest discharge capacities up to nearly 0.5 mAh/cm$^2$.
- A larger mass fraction of electrolyte in the GPE resulted in higher ionic conductivities and higher discharge capacities on average for nearly all electrolyte and GPE compositions.
- The printed $MnO_2$ electrodes began to break down during cycling. This likely indicated shape change from intercalation.

### 7.1.3 Water-Electrolyte Interactions

- The [BMIm][OTf]-based electrolyte absorbed water from the environment as a function of the concentration of $Zn(OTf)_2$ dissolved within it. More salt resulted in higher water absorption.
- Dry GPEs with little water content exhibited low current densities during cyclic voltammetric tests. Wet GPEs with nearly 2.6% by mass of water also produced cells with low current densities during cyclic voltammetric tests. However, GPEs with some water, approximately 14%, resulted in higher current densities for the same tests.
- When investigating cell cyclability and discharge capacity, some water was required in order to produce functional cells. Cells with a dry GPE exhibited low discharge capacities in all cases when compared to cells with water.

### 7.1.4 Component Optimization and Integration

- Printed $MnO_2$ electrode composition C with 8% PVDF-HFP coupled with a [1:6.5]2:1:5 GPE produced the highest discharge capacities of up to 1 mAh/cm$^2$ and an average of 0.551 mAh/cm$^2$. Additional PVDF-HFP did seem to help cell capacity despite the non-functional cell results made with composition B with 30% PVDF-HFP.
- These cells successfully powered a commercial off-the-shelf microcontrol unit for several tens of seconds at a current draw of approximately 112.5 $\mu$A per parallel branch of two

cells in series. The final integrated application expected that the cells would only have to power the microcontrol unit for milliseconds at a time.

- Cell failure was found to be caused by delamination in every cell investigated. This was likely the result of repeated shape change from the intercalation and deintercalation of $Zn^{2+}$ ions with the printed $MnO_2$ electrode.

## 7.2 Future Work

The research presented herein provides a foundation by which the work can be continued to further improve cell cycle life, reliability, and capacity. The results and advancements achieved are promising in the ability to produce rechargeable zinc-based batteries in standard laboratory environments with these new materials.

From the results obtained, it is clear that additional research must be conducted to improve the printed $MnO_2$ electrode. Primarily, alternative polymer binders and other additives must be investigated to create mechanically stable structures during assembly and cycling. For assembly, the NMP within the GPE was found to dissolve the printed electrode likely because of the use of PVDF-HFP in the electrode that dissolves in organic solvents. If PVDF-HFP could be replaced with a polymer that does not dissolve in NMP, then direct-write printing of the GPE onto the $MnO_2$ electrode would be enabled. Water-based polymers such as PSBR may be potential candidates, but experiments that quantify the interactions between the GPE materials and the candidate polymers must be conducted. Contact angle tests will again be used along with laser confocal microscopy to determine if the polymer selection will affect the surface morphology. Upon selecting a new candidate polymer, several compositions must be made and tested in full cells to determine its feasibility in creating functional batteries and an optimal composition for both manufacturing and electrochemical performance.

Only a single ionic liquid was investigated within this research and many alternatives exist with different material properties and costs. Importantly ionic liquids exist that are hydrophobic, like 1-ethyl-3-methylimidazolium bis(trifluoromethylsulfonyl)imide ([EMIm][TFSI]), whereas [BMIm][OTf] is considered moderately hydrophilic. Testing such alternative ionic liquids may allow for better control of moisture saturation into the electrolyte. However to create functional electrolytes with these ILs, the $Zn(OTf)_2$ must be replaced with a zinc salt that has an anion that matches the one within the IL. Thus $Zn(TFSI)_2$ must be used with [EMIm][TFSI]. With these new materials, cyclic voltammetry at many salt concentrations must be conducted to determine the feasibility of using these materials. Upon the successful acquisition of redox peaks, additional experiments focusing on water saturation and cell capacity and cyclability can then be conducted.

In addition to a focus on discovering new electrolyte materials, research must be conducted to determine possible methods to control the structure of the GPE. The spherulite-like structure achieved in this research was shown to be relatively porous. This is only one of sev-

eral types that can be created with PVDF-HFP, although the addition of the electrolyte into the solution before casting may prevent other structures from being achieved. Such changes could also affect how the GPE wets onto the printed electrodes. Ultimately there will be limits in terms of what can be achieved with these materials, so alternatives to PVDF-HFP should also be investigated. PVDF and and other polymers that dissolve in organic solvents are potential candidates. Water-based polymers such as polyethylene oxide (PEO) should be avoided because of the negative influence of high concentrations of water in the electrolyte. As new polymers are selected, CV and EIS experiments should be conducted to ensure that redox peaks can be achieved and that the impedance of the GPE remains around or above 1 mS/cm.

An emphasis should continue to be placed on research into the interfacial interactions between the GPE and the electrodes. With the goal of printing the GPE directly onto the electrodes, improving the contact between them is paramount. Dispersants and wetting agents could be added to the printed electrode ink to reduce the roughness and waviness. However it is not yet clear how a flatter surface will affect wetting of the GPE. Wetting agents could also be added to the GPE solution but again the effect on electrochemical performance is not yet known. With delamination shown to be the dominant failure mechanism of the cells with the optimized compositions, surface treatments and modification should be tested directly on the substrate. Roughening the stainless steel foil either with sandpaper or through chemical means may improve adhesion and reduce the incidence of delamination.

The final main point of future research should be in developing a printed zinc electrode. Zinc has the potential to form zinc oxide when exposed to moist, ambient environments, thus the polymer binder selection and process control are likely to be very different than for the $MnO_2$ electrode. Water-based polymers may not be ideal choices because of the use of water as a solvent. Just like how the printed $MnO_2$ likely changes volume during cycling, the zinc electrode will do the same. Thus care must be taken when investigating polymers to ensure that a stable matrix can be formed that does not breakdown as zinc dissolves and replates during battery use. Finally, the electrodes should be tested and manufactured in a dry, inert environment like the argon-filled glovebox noted previously. This will provide results that can confirm the environmental sensitivity of the materials.

# Appendix A

# Olympus Calibration Table

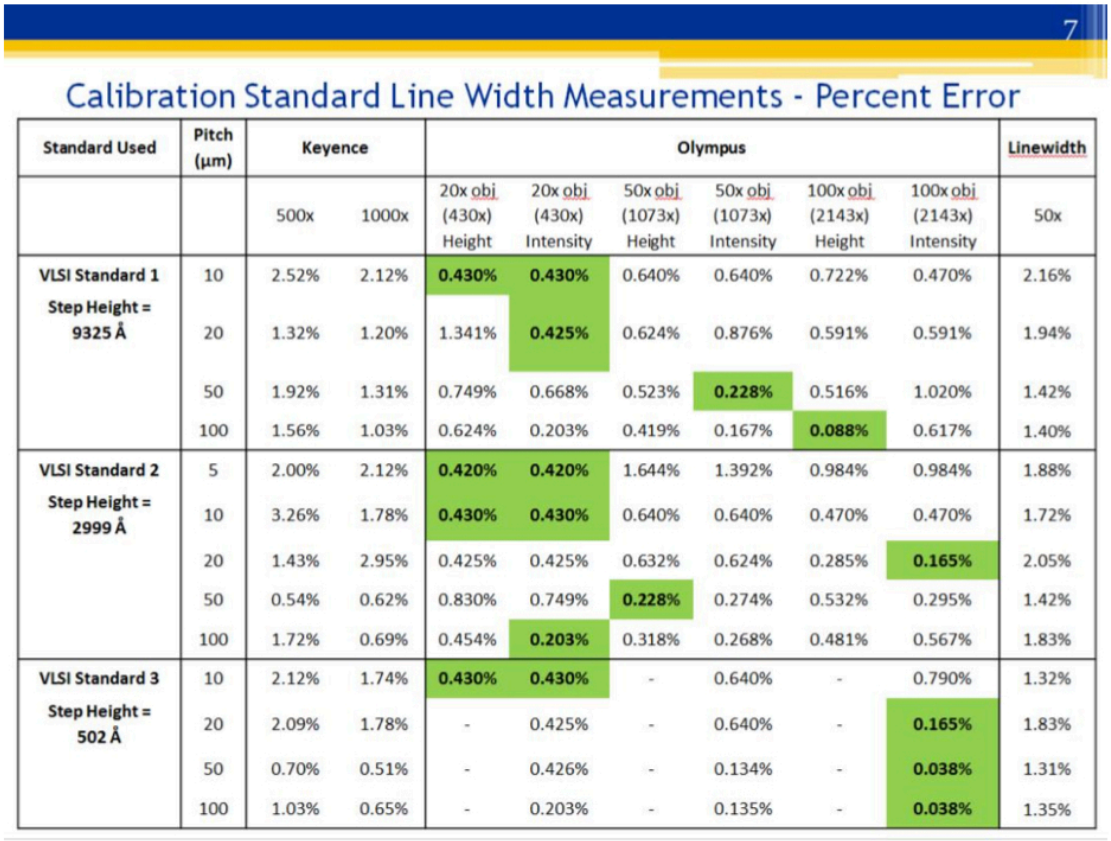

7

## Calibration Standard Line Width Measurements - Percent Error

| Standard Used | Pitch (µm) | Keyence | | Olympus | | | | | | Linewidth |
|---|---|---|---|---|---|---|---|---|---|---|
| | | 500x | 1000x | 20x obj (430x) Height | 20x obj (430x) Intensity | 50x obj (1073x) Height | 50x obj (1073x) Intensity | 100x obj (2143x) Height | 100x obj (2143x) Intensity | 50x |
| VLSI Standard 1 | 10 | 2.52% | 2.12% | **0.430%** | **0.430%** | 0.640% | 0.640% | 0.722% | 0.470% | 2.16% |
| Step Height = 9325 Å | 20 | 1.32% | 1.20% | 1.341% | **0.425%** | 0.624% | 0.876% | 0.591% | 0.591% | 1.94% |
| | 50 | 1.92% | 1.31% | 0.749% | 0.668% | 0.523% | **0.228%** | 0.516% | 1.020% | 1.42% |
| | 100 | 1.56% | 1.03% | 0.624% | 0.203% | 0.419% | 0.167% | **0.088%** | 0.617% | 1.40% |
| VLSI Standard 2 | 5 | 2.00% | 2.12% | **0.420%** | **0.420%** | 1.644% | 1.392% | 0.984% | 0.984% | 1.88% |
| Step Height = 2999 Å | 10 | 3.26% | 1.78% | **0.430%** | **0.430%** | 0.640% | 0.640% | 0.470% | 0.470% | 1.72% |
| | 20 | 1.43% | 2.95% | 0.425% | 0.425% | 0.632% | 0.624% | 0.285% | **0.165%** | 2.05% |
| | 50 | 0.54% | 0.62% | 0.830% | 0.749% | **0.228%** | 0.274% | 0.532% | 0.295% | 1.42% |
| | 100 | 1.72% | 0.69% | 0.454% | **0.203%** | 0.318% | 0.268% | 0.481% | 0.567% | 1.83% |
| VLSI Standard 3 | 10 | 2.12% | 1.74% | **0.430%** | **0.430%** | - | 0.640% | - | 0.790% | 1.32% |
| Step Height = 502 Å | 20 | 2.09% | 1.78% | - | 0.425% | - | 0.640% | - | **0.165%** | 1.83% |
| | 50 | 0.70% | 0.51% | - | 0.426% | - | 0.134% | - | **0.038%** | 1.31% |
| | 100 | 1.03% | 0.65% | - | 0.203% | - | 0.135% | - | **0.038%** | 1.35% |

**Figure 5:** Comparison of percent error between keyence video optical microscope, olympus confocal microscope, and linewidth optical microscope when measuring VLSI standards. Measurements contributed by Katie Neff.

J. Clarkson – January 2013

Figure A.1: Olympus LEXT OLS3000 3D Laser Confocal Microscope provided courtesy of Katie Neff and Jeffrey Clarkson.

# Appendix B

# Electrode Shape Change Calculation

During discharge in lithium-ion batteries, electrodes have been known to increase in volume up to 300% as a result of ion intercalation into the electrode lattice [26]. The modeling of this phenomenon is dependent on the state of charge, the electrode materials used, and whether the active electrode material the ions intercalate into is encased in a rigid or elastic shell. The following calculation is deliberately simplified and uses the conservation of volume to approximate how much the volume could change should the ions displace the lattice in non-ideal intercalation.

With the knowledge that 1 mAh is equivalent to 3.6 coulombs (C), 1 C is approximately $6.241\times10^{18}$ electrons ($e^-$), the oxidation of zinc to $Zn^{2+}$ produces 2 $e^-$, and the atomic radius of a $Zn^{2+}$ ion is 88 pm and is approximated as a sphere, the volume change of the printed $MnO_2$ electrode can be approximated if intercalation did occur for all of the $Zn^{2+}$ produced on a 1 mAh cell discharge. Thus the number of zinc ions, $N_{Zn^{2+}}$ produced for a 1 mAh discharge is given by

$$N_{Zn^{2+}} = \frac{3.6 \times 6.241 \times 10^{18} e^-}{2e^-/Zn^{2+}} = 11.234 \times 10^{18} \tag{B.1}$$

The volume of the $Zn^{2+}$ ion, $V_{Zn^{2+}}$ is then given by

$$V_{Zn^{2+}} = \pi \times 8.8 \times 10^{-9} cm = 2.141 \times 10^{-24} cm^3 \tag{B.2}$$

Thus the volume of all of the $Zn^{2+}$ ions, $V_{all}$ produced on a 1 mAh discharge is given by

$$V_{all} = N_{Zn^{2+}} \times V_{Zn^{2+}} = 2.405 \times 10^{-5} cm^3 = 2.405 \times 10^{7} \mu m^3 \tag{B.3}$$

With the average electrode thickness of 100 $\mu$m and lateral dimensions of 100 $\mu$m-by-100 $\mu$m, the volume of a single printed $MnO_2$ electrode, $V_{electrode}$ is given by

$$V_{electrode} = 100 \times 1000 \times 1000 = 10^8 \mu m^3 \tag{B.4}$$

Thus the volume change of the printed electrode, $\Delta V_{electrode}$ if said electrode absorbed the full mass of the $Zn^{2+}$ ions is given by

$$\Delta V_{electrode} = \frac{2.405 \times 10^7}{10^8} \times 100\% = 24.05\% \tag{B.5}$$

# Appendix C

# Gamry Analysis Python Module

```
''' Module for analyzing results retrieved from Gamry

Author: Rich Winslow
Principal Investigators: Prof. Paul Wright, Prof. James Evans
University: University of California, Berkeley
'''

import matplotlib
# matplotlib.use('SVG')

import matplotlib.pyplot as plt
import numpy

font = {'family': 'Arial', 'size': 16}
matplotlib.rc('font', **font)


class EIS:

    ''' Analyzes data from Gamry EIS

    Pulls data from .dta file for plotting and analysis. Can look at the
    Nyquist plot and determine the DC resistance for ionic conductivity.

    '''

    def __init__(self, filename=None, thickness=0.001, area=1):
        ''' Opens file and retrieves data.

        Retrieves time, frequency, real impedance, imaginary impedance,
        magnitude, and phase. Assumes that the first part of the file is an
        OCV test and that the header for the table consists of two lines.

        Unit requirements:
```

```
            R_solution [ohm]
            Thickness [cm]
            Area [cm^2]
        '''

        self.time = []
        self.freq = []
        self.real = []
        self.imag = []
        self.phaz = []
        self.magn = []

        self.r_solution = None
        self.conductivity = None

        self.filename = filename
        self.thickness = thickness
        self.area = area

        with open(filename, errors='replace') as f:
            rows = f.readlines()

            switch = False
            for index, row in enumerate(rows):
                row = row.split()
                try:
                    if row:
                        if row[0] == 'ZCURVE':
                            switch = index + 2

                        if (self.is_num(row[0]) and switch and index > switch):
                            self.time.append(float(row[1]))
                            self.freq.append(float(row[2]))
                            self.real.append(float(row[3]))
                            self.imag.append(float(row[4]))
                            self.magn.append(float(row[6]))
                            self.phaz.append(float(row[7]))
                except Exception:
                    raise

            try:
                self.calculate_conductivity()
            except Exception:
                raise

    def calculate_conductivity(self):
        try:
            max_imag_index = self.imag.index(max(self.imag))
            self.r_solution = self.real[max_imag_index]
            self.conductivity = (
```

```
                (self.thickness * 1000) / (self.area * self.r_solution))
        except Exception:
            raise

    def list_metrics(self):
        print('File: ' + self.filename)
        print('R_solution: ' + str(self.r_solution) + ' ohm')
        print('Thickness: ' + str(self.thickness) + ' cm')
        print('Area: ' + str(self.area) + ' cm^2')
        print('Conductivity: ' + str(self.conductivity) + ' mS/cm')
        print('--')

    def plot_nyquist(self, log_plot=False, ylim=None, save_svg=False):
        ''' Plots real impedance vs negative imaginary impedance '''

        self.calculate_conductivity()
        conductivity_string = "{0:.3f}".format(self.conductivity)

        if log_plot:
            plt.loglog(self.real, [-1 * v for v in self.imag],
                       marker='.', markersize=15)
        else:
            plt.plot(self.real, [-1 * v for v in self.imag],
                     marker='.', markersize=15)

        if ylim:
            plt.ylim(ylim[0], ylim[1])

        plt.xlabel('Z_real (ohm)')
        plt.ylabel('(-) Z_imag (ohm)')

        if save_svg:
            plt.savefig(self.filename + '.svg')
        else:
            plt.title('Nyquist Plot - ' +
                      conductivity_string + ' mS/cm - ' + self.filename)
            plt.show()

    def is_num(self, s):
        try:
            float(s)
            return True
        except ValueError:
            return False


class CV:

    ''' Analyzes data from Gamry cyclic voltammetry data
```

```
    Pulls data from .dta file for plotting and analysis.

    '''

    def __init__(self, filename=None):
        ''' Opens file and retrieves data. '''

    # Pt   T      Vf     Im   Vu   Sig  Ach  IERange  Over
    # s    V vs.  Ref.   A    V    V    V    #        bits

        self.cycles = {}

        with open(filename, errors='replace') as f:
            rows = f.readlines()

            switch = False
            current_cycle_time = []
            current_cycle_voltage = []
            current_cycle_current = []

            for index, row in enumerate(rows):
                row = row.split()
                try:
                    if row:
                        if row[0][0:5] == 'CURVE':
                            curve_number = int(row[0][5::])
                            switch = index + 2
                            if current_cycle_time:
                                self.cycles[curve_number - 1] = {
                                    'time': current_cycle_time,
                                    'voltage': current_cycle_voltage,
                                    'current': current_cycle_current,
                                    }
                                    current_cycle_time = []
                                    current_cycle_voltage = []
                                    current_cycle_current = []

                        if (self.is_num(row[0]) and switch and index > switch):
                            # Save data and convert current to mA
                            current_cycle_time.append(float(row[1]))
                            current_cycle_voltage.append(float(row[2]))
                            current_cycle_current.append(float(row[3]) * 1000)

                except Exception:
                    raise

            # Save data and convert current to mA
            self.cycles[curve_number] = {
                'time': current_cycle_time,
                'voltage': current_cycle_voltage,
```

```
            'current': current_cycle_current * 1000,
        }

    def plot_current_voltage(self, cycle_index=0, title=None):
        ''' Plots current vs voltage for one or all cycles '''

        if cycle_index:
            plt.plot(self.cycles[cycle_index]['voltage'],
                     self.cycles[cycle_index]['current'],
                     marker='.', markersize=12)
        else:
            for i in range(1, len(self.cycles)):
                plt.plot(self.cycles[i]['voltage'],
                         self.cycles[i]['current'],
                         marker='.', markersize=12)

        plt.xlabel('Potential (V)')
        plt.ylabel('Current (mA)')

        plt.title('CV ' + str(title))
        plt.show()

    def is_num(self, s):
        try:
            float(s)
            return True
        except ValueError:
            return False
```

# Appendix D

# Surface Analysis Python Module

```
''' Module for processing surfaces from Olympus LEXT software

Author: Rich Winslow
Principal Investigators: Prof. Paul Wright, Prof. James Evans
University: University of California, Berkeley

'''

import json
import math
import matplotlib.pyplot as plt
import matplotlib.cm as cm
import numpy as np
import scipy
import scipy.ndimage as ndimage
import scipy.ndimage.filters as filters

from os.path import splitext


class Surface:

    ''' Generates surface profile components and metrics

    Produces primary, waviness, and roughness profiles from a CSV containing
    height information from Olympus LEXT software

    Note that the LEXT software starts indexing at 1 for row numbers, while
    Python starts indexing at 0 for when you're comparing sections of
    profiles

    __init__:
        Parses row by comma because input must be a CSV.
```

```
        All data from a LEXT-generated CSV is on a single line, so it is
        reshaped to a 2-D matrix from a 1-D vector.

        arguments:
            filepath = Path to data
            cutoff = Cutoff wavelength for low pass FFT filter
                default: 80 um
            sample_width = Width of sample area in microns (um)
                default: 643 um at 10x magnification on Olympus
                common: 1789 um for a 3x3 stitched surface with 10 pct overlap

    '''

    def __init__(self, filepath=None, sample_width=643, cutoff=80, **kwargs):
        ''' Opens file and processes all data

        Parses row by comma because input must be a CSV.
        '''

        self.filepath = filepath
        self.cutoff = cutoff
        self.sample_width = sample_width
        self.cmap = cm.coolwarm
        self.cmap = cm.jet

        if (filepath):
            with open(filepath) as f:
                row = f.readlines()
                self.primary = [float(x) for x in row[0].split(',')
                                if x is not None and len(x) > 0]

                print('File: ' + self.filepath)
                print('Total points of data: ' + str(len(self.primary)))
                self.dimensions = self.get_even_dimensions(len(self.primary))
                self.primary = np.reshape(self.primary, self.dimensions)
                print('Data dimensions: ' + str(self.dimensions))

                self.parse_waviness()
                self.zero_average_waviness()
                self.parse_roughness()
                self.calculate_metrics()
                print('----')

    def get_even_dimensions(self, integer):
        ''' Find integer dimensions close to the square root of the number of
        points in the data.

        Assumes that the map will end up with an aspect ratio greater than 1
        (Wider than it is tall)
```

```
        '''
        root_int = int(np.sqrt(integer))
        while integer % root_int:
            root_int += 1
        return [root_int, integer // root_int]

    def rotate_recalculate(self):
        print('File: ' + self.filepath)
        print('Rotating primary profile 90 deg and recalculating')

        self.primary = np.rot90(self.primary)
        self.dimensions = [self.dimensions[1], self.dimensions[0]]

        print('Data dimensions: ' + str(self.dimensions))

        self.parse_waviness()
        self.zero_average_waviness()
        self.parse_roughness()
        self.calculate_metrics()

        print('----')

    def json_out(self, data_names, suffix=None):
        ''' Saves all data in object to a file '''

        output = {}
        for name in data_names:
            output[name] = getattr(self, name)

        output = json.dumps(output, separators=(',', ': '))
        name, extension = splitext(self.filepath)
        if suffix and suffix[0] is not '_':
            suffix = '_' + suffix
        json_path = name + '_' + '+'.join(data_names) + str(suffix) + '.json'

        with open(json_path, 'w') as f:
            f.write(output)
            print('Output data to ' + json_path)

    def parse_waviness(self, primary=None, cutoff=None, sample_width=None,
                       return_results=False):
        ''' Parse waviness from each row of the primary profile

        Computes the FFT of the primary profile line-by-line.

        To prevent non-zero values at the boundaries, the primary profile is
        extended at the beginning and end by a flipped version of itself.

        The dataset is all real valued, so the FFT is symmetric. Thus, the
        signal strength must be doubled to fit the data correctly.
```

```
    For waviness, a low-pass filter is used (allows low frequencies/long
    wavelength signals) to allow the wavelengths longer than the cutoff
    wavelength to contribute to the final waviness profile. All values
    outside the range of allowed values are set to zero.

    '''

    print('Parsing waviness')

    if not primary:
        primary = self.primary
    if not cutoff:
        cutoff = self.cutoff
    if not sample_width:
        sample_width = self.sample_width

    primary_row_len = len(primary[0])

    waviness = []

    for i, row in enumerate(primary):
        profile = []
        flipped = row[::-1]

        profile.extend(flipped)
        profile.extend(row)
        profile.extend(flipped)

        f = np.array(np.fft.fft(profile))
        f[1:-1] = f[1:-1] * 2

        wavelengths = ([
            2 * (3 * sample_width) /
            j for j in range(1, primary_row_len)
        ])

        stop_index = 0
        while wavelengths[stop_index] > cutoff:
            stop_index += 1

        filtered = f
        filtered[stop_index:-1] = 0

        ifft_result = np.real(np.fft.ifft(filtered))
        middle = ifft_result[primary_row_len:2 * primary_row_len]
        waviness.append(middle.tolist())

    if return_results:
        return {'waviness': waviness,
```

```
                'wavelengths': wavelengths}
        else:
            self.wavelengths = wavelengths
            self.waviness = waviness

    def blur_dataset(self, dataset, sigma=5, order=0):
        ''' Uses gaussian filter to blur a dataset '''

        return ndimage.gaussian_filter(dataset, sigma=sigma, order=order)

    def detect_extrema(self, dataset, neighborhood_size=40, threshold=0):
        ''' Detects the extrema in a given dataset

        Uses scipy filters to find extrema, then returns the x and y
        coordinates for the peaks and valleys
        '''

        print('Detecting extrema')

        dataset = self.blur_dataset(dataset, sigma=20)

        data_max = filters.maximum_filter(dataset, neighborhood_size)
        maxima = (dataset == data_max)
        data_min = filters.minimum_filter(dataset, neighborhood_size)
        minima = (dataset == data_min)
        diff_max = ((data_max - data_min) > threshold)
        diff_min = ((data_min - data_max) < threshold)
        maxima[diff_max == 0] = 0
        minima[diff_min == 0] = 0

        labeled, num_objects = ndimage.label(maxima)
        slices = ndimage.find_objects(labeled)
        x_max, y_max = [], []
        for dy, dx in slices:
            x_center = (dx.start + dx.stop - 1) / 2
            x_max.append(x_center)
            y_center = (dy.start + dy.stop - 1) / 2
            y_max.append(y_center)

        labeled, num_objects = ndimage.label(minima)
        slices = ndimage.find_objects(labeled)
        x_min, y_min = [], []
        for dy, dx in slices:
            x_center = (dx.start + dx.stop - 1) / 2
            x_min.append(x_center)
            y_center = (dy.start + dy.stop - 1) / 2
            y_min.append(y_center)

        peaks = [dataset[int(y)][int(x)] for x, y in zip(x_max, y_max)]
        valleys = [dataset[int(y)][int(x)] for x, y in zip(x_min, y_min)]
```

```
        return {
            'maximum': {'x': x_max, 'y': y_max},
            'minimum': {'x': x_min, 'y': y_min},
            'peaks': peaks,
            'valleys': valleys,
        }

    def map_average_climb_distance(self, dataset):
        ''' Finds and returns the average of the shortest distances between
        each minimum to the nearest maximum in units of um '''

        extrema = self.detect_extrema(dataset)
        maxima = list(zip(extrema['maximum']['x'], extrema['maximum']['y']))
        minima = list(zip(extrema['minimum']['x'], extrema['minimum']['y']))

        conversion_ratio = self.sample_width / self.dimensions[0]
        distances = map_extrema_distances(maxima, minima)

        return conversion_ratio * (sum(distances) / len(distances))

    def map_extrema(self, dataset):
        ''' Finds the extrema of a provided dataset '''

        extrema = self.detect_extrema(dataset)
        maxima = list(zip(extrema['maximum']['x'], extrema['maximum']['y']))
        minima = list(zip(extrema['minimum']['x'], extrema['minimum']['y']))

        conversion_ratio = self.sample_width / self.dimensions[0]

        distances = map_extrema_distances(maxima, minima)
        print(distances)
        print(conversion_ratio * (sum(distances) / len(distances)))
        print((sum(distances) / len(distances)))
        print(len(distances))
        print(len(minima))

    def zero_average_waviness(self):
        ''' Shifts the waviness profile so its average is at zero

        Finds the average of each row of waviness data, then subtracts the
        average from each value in the row and appends it to a new instance
        variable.

        '''

        print('Zero averaging waviness')
        waviness_zero_averaged = []
        length = len(self.waviness[0])
        for row in self.waviness:
```

```
            ave = sum(row) / length
            waviness_zero_averaged.append([v - ave for v in row])

        self.waviness_zero_averaged = waviness_zero_averaged

    def parse_roughness(self):
        ''' Parse roughness from primary and waviness profiles

        Runs through each row in primary and waviness profiles and finds the
        difference between them to get the roughness

        '''

        print('Parsing roughness')

        self.roughness = []
        for i, row in enumerate(self.primary):
            self.roughness.append(list(self.primary[i] - self.waviness[i]))

    def generate_metrics_per_row(self, prefix, matrix):
        ''' Calculate and set metrics for each row in a matrix

        Xa - arithmetic average
        Xq - root mean square
        Xp - maximum height of peaks
        Xv - maximum depth of valleys
        Xz - maximum height of surface
        Xz10 - ten point height
        '''

        a = [sum(np.abs(row)) / self.dimensions[0] for row in matrix]
        q = [np.sqrt(sum(np.square(row)) / self.dimensions[0])
             for row in matrix]
        p = [max(row) for row in matrix]
        v = [min(row) for row in matrix]
        z = [np.abs(p) + np.abs(v)]

        # raw_desc = [sorted(row, reverse=True) for row in matrix]
        # peak_sums = [sum(np.abs(raw_desc[0:5])) for row in raw_desc]
        # valley_sums = [sum(np.abs(raw_desc[-1:-6])) for row in raw_desc]
        # z10 = [(peaks + valleys)/5 for peaks, valleys
        #        in zip(peak_sums, valley_sums)]

        setattr(self, prefix + 'a', a)
        setattr(self, prefix + 'q', q)
        setattr(self, prefix + 'p', p)
        setattr(self, prefix + 'v', v)
        setattr(self, prefix + 'z', z)
        # setattr(self, prefix + 'z10', z10)
```

```
    def generate_metrics_for_full_surface(self, prefix, matrix):
        ''' Calculate and set metrics for the full surface

        Xa - arithmetic average
        Xq - root mean square
        Xp - maximum height of peaks
        Xv - maximum depth of valleys
        Xz - maximum height of surface
        Xz10 - ten point height
        Xc - average distance from valley to nearest peak
        Xstd_peaks - standard deviation of peak heights
        Xstd_valleys - standard deviation of valley heights
        '''

        raw = sum(sum(np.abs(row) for row in matrix))
        a = raw / (self.dimensions[0] * self.dimensions[1])

        raw = sum(sum(np.square(row) for row in matrix))
        q = np.sqrt(raw / (self.dimensions[0] * self.dimensions[1]))

        raw = [v for row in matrix for v in row]
        p = max(raw)
        v = min(raw)
        z = np.abs(p) + np.abs(v)

        extrema = self.detect_extrema(matrix)
        ordered_peaks = sorted(extrema['peaks'])[::-1]
        ordered_valleys = sorted(extrema['valleys'])[::-1]
        peak_sum = sum(np.abs(ordered_peaks[0:5]))
        valley_sum = sum(np.abs(ordered_valleys[0:5]))
        z10 = (peak_sum + valley_sum) / 5
        average_climb = self.map_average_climb_distance(matrix)

        std_peaks = np.std(extrema['peaks'])
        std_valleys = np.std(extrema['valleys'])

        setattr(self, prefix + 'a', a)
        setattr(self, prefix + 'q', q)
        setattr(self, prefix + 'p', p)
        setattr(self, prefix + 'v', v)
        setattr(self, prefix + 'z', z)
        setattr(self, prefix + 'z10', z10)
        setattr(self, prefix + 'c', average_climb)
        setattr(self, prefix + 'std_peaks', std_peaks)
        setattr(self, prefix + 'std_valleys', std_valleys)

    def calculate_metrics(self):
        ''' Calculate metrics for each row of waviness and roughness

        Calculates:
```

```
            Wa_rows = Average waviness per row
            Ra_rows = Average roughness per row

        '''

        print('Calculating metrics')

        self.generate_metrics_per_row('R', self.roughness)
        self.generate_metrics_per_row('W', self.waviness_zero_averaged)
        self.generate_metrics_for_full_surface('S', self.roughness)
        self.generate_metrics_for_full_surface(
            'V', self.waviness_zero_averaged)

    def list_metrics(self):
        ''' List all metrics values for surface '''

        print(self.filepath)

        print('Ra, Rq, Rp, Rv, Rz: <matrices>')
        print('Wa, Wq, Wp, Wv, Wz: <matrices>')

        print('Sa: {0:.3f}'.format(self.Sa))
        print('Sq: {0:.3f}'.format(self.Sq))
        print('Sp: {0:.3f}'.format(self.Sp))
        print('Sv: {0:.3f}'.format(self.Sv))
        print('Sz: {0:.3f}'.format(self.Sz))
        print('Sz10: {0:.3f}'.format(self.Sz10))
        print('Sc: {0:.3f}'.format(self.Sc))
        print('Sstd_peaks: {0:.3f}'.format(self.Sstd_peaks))
        print('Sstd_valleys: {0:.3f}'.format(self.Sstd_valleys))

        print('--')

        print('Va: {0:.3f}'.format(self.Va))
        print('Vq: {0:.3f}'.format(self.Vq))
        print('Vp: {0:.3f}'.format(self.Vp))
        print('Vv: {0:.3f}'.format(self.Vv))
        print('Vz: {0:.3f}'.format(self.Vz))
        print('Vz10: {0:.3f}'.format(self.Vz10))
        print('Vc: {0:.3f}'.format(self.Vc))
        print('Vstd_peaks: {0:.3f}'.format(self.Vstd_peaks))
        print('Vstd_valleys: {0:.3f}'.format(self.Vstd_valleys))

        print('----')

    def plot_dataset_surface(self, dataset, title=None, narrow=False,
                             extrema=False, maxima=False, minima=False,
                             contours=False, contour_levels=7, cmap=None):
        ''' Plots a given dataset as a surface '''
```

```
        if not cmap:
            cmap = self.cmap

        if not title:
            title = 'Dataset (Surface)'

        if contours:
            plt.contour(dataset, contour_levels, cmap=cmap)
            plt.contourf(dataset, contour_levels, cmap=cmap)
        else:
            im = plt.imshow(dataset, cmap=cmap)

        if narrow:
            ave = np.average(dataset)
            std = np.std(dataset)
            vmin = ave - (2 * std)
            vmax = ave + (2 * std)
            plt.clim(vmin, vmax)

        if extrema:
            plt.autoscale(False)
            extrema = self.detect_extrema(dataset)
            plt.plot(extrema['maximum']['x'],
                     extrema['maximum']['y'], 'go')
            plt.plot(extrema['minimum']['x'],
                     extrema['minimum']['y'], 'yo')
        elif maxima:
            plt.autoscale(False)
            extrema = self.detect_extrema(dataset)
            plt.plot(extrema['maximum']['x'],
                     extrema['maximum']['y'], 'go')
        elif minima:
            plt.autoscale(False)
            extrema = self.detect_extrema(dataset)
            plt.plot(extrema['minimum']['x'],
                     extrema['minimum']['y'], 'yo')
        else:
            plt.colorbar(label='Height (um)')

        plt.xlabel('X Position (Index)')
        plt.ylabel('Y Position (Index)')
        plt.title(title)
        plt.show()

    def plot_dataset_index(self, dataset, title=None, index=None, cmap=None):
        ''' Plots the given dataset at a single index '''

        X = np.linspace(0, self.sample_width, len(dataset[0]))

        plt.plot(X, dataset[index])
```

```
        plt.xlim(0, self.sample_width)

        plt.xlabel('Position (um)')
        plt.ylabel('Height (um)')
        plt.title('Dataset @ Index ' + str(index))
        plt.show()

    def plot_section(self, index):
        ''' Plots cross section of profile with waviness and roughness on plot

        '''

        X = np.linspace(0, self.sample_width, len(self.primary[0]))

        plt.plot(X, self.primary[index], label='Primary')
        plt.plot(X, self.roughness[index], label='Roughness')
        plt.plot(X, self.waviness_zero_averaged[
                index], label='Waviness', linewidth=3.0)

        plt.xlim(0, self.sample_width)
        plt.xlabel('Position (um)')
        plt.ylabel('Height (um)')
        plt.title('Section @ Index ' + str(index))
        plt.legend(ncol=3, loc='upper center')
        plt.show()

    def plot_metrics(self, metric_name):
        ''' Plots data from one of the metrics and center around zero '''

        metric = getattr(self, metric_name)

        centered = (metric - (sum(metric) / float(len(metric))))

        X = np.linspace(0, self.sample_width, len(centered))
        plt.plot(X, centered)

        plt.gcf().subplots_adjust(bottom=0.3)
        plt.xlim(0, self.sample_width)
        plt.xlabel('Position (um)')
        plt.ylabel('Height (um)')
        plt.title('Metric ' + metric_name)
        plt.show()


def map_extrema_distances(maxima, minima):
    shortest_distances = []
    distances = []
    for min_x, min_y in minima:
        for max_x, max_y in maxima:
            distances.append(
```

```
                math.sqrt((max_x - min_x) ** 2 + (max_y - min_y) ** 2))
        distances.sort()
        shortest_distances.append(distances[0])
        distances = []
    return shortest_distances


def plot_many(x_vals, y_vals, labels, title=None, xlim=None, ylim=None):
    for x, y, label in zip(x_vals, y_vals, labels):
        plt.plot(x, y, label=label)
    if title:
        plt.title(title)
    if xlim:
        plt.xlim(xlim[0], xlim[1])
    if ylim:
        plt.ylim(ylim[0], ylim[1])
    plt.legend(loc='upper right')
    plt.show()
```

# Appendix E

# Thermogravimetric Analysis Python Module

```
import matplotlib.pyplot as plt


class TGA:
    ''' Plots data from TA TGA Q50

    Units for default attributes:
        Time (ms)
        Temperature (C)
        Mass (mg)
    '''

    def __init__(self, filepath, **kwargs):
        self.filepath = filepath

        self.time = []
        self.temp = []
        self.mass = []
        self.weight_pct = []

        self.sample_name = None
        self.method = []
        self.method_steps = []

        collect_data = False

        with open(filepath, encoding='utf-16') as f:
            rows = f.readlines()

            for i, row in enumerate(rows):
                values = row.split()
```

```
            if collect_data and values:
                self.time.append(values[0])
                self.temp.append(values[1])
                self.mass.append(values[2])
            else:
                if values[0] == 'StartOfData':
                    collect_data = True
                elif values[0] == 'Sample':
                    self.sample_name = values[1]
                elif values[0] == 'Size':
                    self.mass_start = values[1]
                elif values[0] == 'Method':
                    self.method.append(values[1])
                elif values[0] == 'OrgMethod':
                    self.method_steps.append(values[1])

        self.weight_pct = [100*float(mass)/float(self.mass[0])
                           for mass in self.mass]

    def plot_time_temp(self):
        plt.plot(self.time, self.temp)

        plt.xlabel('Time (min)')
        plt.ylabel('Temp (C)')
        plt.title('Temperature v. Time - ' + self.filepath)
        plt.show()

    def plot_time_mass(self):
        plt.plot(self.time, self.mass)

        plt.xlabel('Time (min)')
        plt.ylabel('Mass (mg)')
        plt.title('Mass v. Time - ' + self.filepath)
        plt.show()

    def plot_temp_mass(self):
        plt.plot(self.temp, self.mass)

        plt.xlabel('Temp (C)')
        plt.ylabel('Mass (mg)')
        plt.title('Mass v. Temp - ' + self.filepath)
        plt.show()

    def plot_time_temp_mass(self):
        fig, ax1 = plt.subplots()

        left_color = 'b'
        right_color = 'r'

        ax1.plot(self.time, self.mass, color=left_color)
```

```
        ax1.set_xlabel('Time (min)')
        ax1.set_ylabel('Mass (mg)', color=left_color)
        for tick in ax1.get_yticklabels():
            tick.set_color(left_color)

        ax2 = ax1.twinx()
        ax2.plot(self.time, self.temp, color=right_color)
        ax2.set_ylabel('Temp (C)', color=right_color)
        for tick in ax2.get_yticklabels():
            tick.set_color(right_color)

        ax1.set_xlim(0, float(self.time[-1]))
        ax2.set_xlim(0, float(self.time[-1]))

        plt.title('Mass v. Temp - ' + self.filepath)
        plt.show()

    def plot_time_temp_weight_pct(self):
        fig, ax1 = plt.subplots()

        left_color = 'b'
        right_color = 'r'

        ax1.plot(self.time, self.weight_pct, color=left_color)
        ax1.set_xlabel('Time (min)')
        ax1.set_ylabel('Weight (%)', color=left_color)
        for tick in ax1.get_yticklabels():
            tick.set_color(left_color)

        ax2 = ax1.twinx()
        ax2.plot(self.time, self.temp, color=right_color)
        ax2.set_ylabel('Temp (C)', color=right_color)
        for tick in ax2.get_yticklabels():
            tick.set_color(right_color)

        ax1.set_xlim(0, float(self.time[-1]))
        ax2.set_xlim(0, float(self.time[-1]))

        plt.title('Weight Percent v. Temp - ' + self.filepath)
        plt.show()

    def plot_time_weight_pct(self):
        plt.plot(self.time, self.weight_pct)
        plt.xlabel('Time (min)')
        plt.ylabel('Weight (%)')
        plt.title('Weight Percent v. Time - ' + self.filepath)
        plt.show()
```

# Bibliography


[1] ATOFINA Chemicals, Inc. "KYNAR & KYNAR FLEX PVDF". In: *Atofina* ().

[2] Allen J Bard and Larry R Faulkner. *Electrochemical Methods: Fundamentals and Applications, 2nd Edition*. Wiley Global Education, Dec. 2000.

[3] J B Bates and Y T Chu. "Electrode-electrolyte interface impedance: experiments and model". In: *Annals of biomedical engineering* 20.3 (1992), pp. 349–362.

[4] Kyle T Braam, Steven K Volkman, and Vivek Subramanian. "Characterization and optimization of a printed, primary silver–zinc battery". In: *J Power Sources* 199 (Feb. 2012), pp. 367–372.

[5] P Brenni et al. "From Volta onwards: A variety of electrical batteries in the Pavia Museum of Electrical Technology". In: *HISTory of ELectro-technology CONference (HISTELCON), 2012 Third IEEE*. 2012, pp. 1–6.

[6] E Oran Brigham. *The Fast Fourier Transform and Its Applications*. Prentice Hall. Englewood Cliffs, 1988.

[7] Marina Cvjetko Bubalo et al. "A brief overview of the potential environmental hazards of ionic liquids". In: *Ecotoxicology and Environmental Safety* 2014.99 (Nov. 2013), pp. 1–12.

[8] J Cao et al. "Microporous PVDF-HFP-based Polymer Membranes Formed From Supercritical CO2 Induced Phase Separation". In: *Chinese Journal of Polymer Science* 26.01 (2008), pp. 13–21.

[9] Yuanyuan Cao et al. "Water Sorption in Functionalized Ionic Liquids: Kinetics and Intermolecular Interactions". In: *J Chem Eng Data* (Jan. 2013), p. 130124143144001.

[10] Yuanyuan Cao et al. "Water sorption in ionic liquids: kinetics, mechanisms and hydrophilicity". In: *Phys Chem Chem Phys* 14.35 (2012), p. 12252.

[11] A Chen et al. "Dispenser Printed Thermoelectric Energy Generators". In: *cap.ee.ic.ac.uk* ().

[12] C L Cheng, C C Wan, and Y Y Wang. "Microporous PVdF-HFP based gel polymer electrolytes reinforced by PEGDMA network". In: *Electrochemistry Communications* 6.6 (June 2004), pp. 531–535.

[13] Nicholas P Cheremisinoff. *Handbook of Industrial Toxicology and Hazardous Materials*. CRC Press, Jan. 1999.

[14] C Chiappe et al. "An unusual common ion effect promotes dissolution of metal salts in room-temperature ionic liquids: a strategy to obtain ionic liquids having organic–inorganic mixed cations". In: *Green Chem.* 12.1 (2010), p. 77.

[15] Crescent Chemical Company. *Moisture Measurement by Karl Fischer Titrimetry*. GFS Chemicals, Inc. Powell, Ohio, 1991.

[16] Z CUI et al. "Preparation of PVDF/PEO-PPO-PEO blend microporous membranes for lithium ion batteries via thermally induced phase separation process". In: *J Membrane Sci* 325.2 (Dec. 2008), pp. 957–963.

[17] R De Levie. "The influence of surface roughness of solid electrodes on electrochemical measurements". In: *Electrochimica Acta* 10.2 (Feb. 1965), pp. 113–130.

[18] Pablo Fanjul-Bolado et al. "Electrochemical characterization of screen-printed and conventional carbon paste electrodes". In: *Electrochimica Acta* 53.10 (Apr. 2008), pp. 3635–3642.

[19] A Fick. "Taylor & Francis Online". In: *The London* (1855).

[20] C P Fredlake et al. "Thermophysical properties of imidazolium-based ionic liquids". In: *J Chem Eng Data* 49.4 (2004), pp. 954–964.

[21] M G Freire, L M Santos, and A M Fernandes. "An overview of the mutual solubilities of water–imidazolium-based ionic liquids systems". In: *Fluid Phase ...* (2007).

[22] J Fuller, AC Breda, and RT Carlin. "Ionic LiquidPolymer Gel Electrolytes". In: *Journal of the Electrochemical Society* 144 (1997), p. L67.

[23] Abhinav M Gaikwad et al. "A flexible high potential printed battery for powering printed electronics". In: *Appl. Phys. Lett.* 102.23 (June 2013), p. 233302.

[24] M Galinski, A Lewandowski, and I Stepniak. "Ionic liquids as electrolytes". In: *Electrochimica Acta* (2006).

[25] Gamry Instruments. *Basics of Electrochemical Impedance Spectroscopy*. Gamry Instruments. June 2014.

[26] T R Garrick et al. "Modeling Volume Change due to Intercalation into Porous Electrodes". In: *Journal of the Electrochemical Society* 161.8 (Feb. 2014), E3297–E3301.

[27] George A Ghiurcan et al. "Development and Characterization of a Thick-Film Printed Zinc-Alkaline Battery". In: *Journal of the Electrochemical Society* 150.7 (2003), A922.

[28] Ken Gilleo. "Rheology and Surface Chemistry for Screen Printing". In: *Screen Printing* (1989), pp. 128–132.

[29] Craig Gordon and Rolf Rohner. "METTLER TOLEDO Titrators DL32/DL39". In: *bikeitech.com* (Sept. 2003).

[30] M Hilder et al. "Paper-based, printed zinc–air battery". In: *J Power Sources* 194.2 (Dec. 2009), pp. 1135–1141.

[31] CC Ho and JW Evans. "Direct write dispenser printing of zinc microbatteries". In: *Proc PowerMEMS* (2009).

[32] C.C Ho et al. "A super ink jet printed zinc–silver 3D microbattery". In: *J. Micromech. Microeng.* 19.9 (Aug. 2009), p. 094013.

[33] C.C Ho et al. "Direct write dispenser printing of a zinc microbattery with an ionic liquid gel electrolyte". In: *J. Micromech. Microeng.* 20.10 (2010), p. 104009.

[34] Christine Chihfan Ho. "Dispenser Printed Zinc Microbattery with an Ionic Liquid Gel Electrolyte". PhD thesis. University of California, Berkeley, Dec. 2010.

[35] Andreas Hofmann, Michael Schulz, and Thomas Hanemann. "Effect of Conducting Salts in Ionic Liquid based Electrolytes: Viscosity, Conductivity, and Li-Ion Cell Studies". In: *Int. J. Electrochem. Sci* 8 (2013), pp. 10170–10189.

[36] Petri Ihalainen et al. "Influence of Surface Properties of Coated Papers on Printed Electronics". In: *Industrial & Engineering Chemistry Research* 51.17 (2012), pp. 6025–6036.

[37] A D Jenkins et al. "Glossary of basic terms in polymer science (IUPAC Recommendations 1996)". In: *Pure Appl. Chem.* 68.12 (1996), pp. 2287–2311.

[38] G L Ji et al. "PVDF-HFP Membrane Prepared via TIPS Process as the Matrix of Gel Electrolyte for Lithium Ion Battery". In: *Journal of Macromolecular Science®, Part B: Physics* 50.2 (2010), pp. 275–290.

[39] Yide Jin et al. "Functionalized ionic liquids based on guanidinium cations with two ether groups as new electrolytes for lithium battery". In: *J Power Sources* 196.24 (Dec. 2011), pp. 10658–10666.

[40] Max Kamenetsky. "Filtered Audio Demo". In: (Dec. 2014), pp. 1–14.

[41] Hiroshi Kataoka et al. "Conduction Mechanisms of PVDF-Type Gel Polymer Electrolytes of Lithium Prepared by a Phase Inversion Process". In: *J. Phys. Chem. B* 104.48 (Dec. 2000), pp. 11460–11464.

[42] Jayme Scot Keist. "In-situ Analysis of Zinc Electrodeposition within an Ionic Liquid Electrolyte". PhD thesis. Materials Science: University of California, Berkeley, May 2013.

[43] H. Kippan. *Handbook of Print Media*. Berlin-Heidelberg: Soringer-Verlag.

[44] Maaike C Kroon et al. "Decomposition of ionic liquids in electrochemical processing". In: *Green Chem.* 8.3 (2006), pp. 241–245.

[45] Takashi Kuboki et al. "Lithium-air batteries using hydrophobic room temperature ionic liquid electrolyte". In: *J Power Sources* 146.1-2 (Aug. 2005), pp. 766–769.

[46] G Kumar. "Electrochemical characterization of poly(vinylidenefluoride)-zinc triflate gel polymer electrolyte and its application in solid-state zinc batteries". In: *Solid State Ionics* 160.3-4 (June 2003), pp. 289–300.

[47] G G Kumar and S Sampath. "Electrochemical characterization of a zinc-based gel-polymer electrolyte and its application in rechargeable batteries". In: *Journal of the Electrochemical Society* 150.5 (2003), A608–A615.

[48] Kynar. "KYNAR & KYNAR FLEX PVDF". In: *Arkema Inc* ().

[49] Massimo Lazzari, Guojun Liu, and Sebastién Lecommandoux. *Block Copolymers in Nanoscience*. John Wiley & Sons, Jan. 2007.

[50] Jonghyuk Lee et al. "Todorokite-type MnO2 as a zinc-ion intercalating material". In: *Electrochimica Acta* 112 (2013), pp. 138–143.

[51] S Leppävuori et al. "A novel thick-film technique, gravure offset printing, for the realization of fine-line sensor structures". In: *Sensors and Actuators A: Physical* 42.1-3 (Apr. 1994), pp. 593–596.

[52] Chiam-Wen Liew, S Ramesh, and R Durairaj. "Impact of low viscosity ionic liquid on PMMA–PVC–LiTFSI polymer electrolytes based on AC-impedance, dielectric behavior, and HATR–FTIR characteristics". In: *Journal of Materials Research* 27.23 (2012), pp. 2996–3004.

[53] David Linden and Thomas B Reddy. "Basic Concepts". In: *Handbook of Batteries*. McGraw-Hill Professional, 2001.

[54] Andrzej Marciniak. "The Solubility Parameters of Ionic Liquids". In: *International Journal of Molecular Sciences* 11.5 (2010), pp. 1973–1990.

[55] E T McAdams et al. "The linear and non-linear electrical properties of the electrode-electrolyte interface". In: *Biosensors and Bioelectronics* 10.1 (1995), pp. 67–74.

[56] Denis Menshykau, Ian Streeter, and Richard G Compton. "Influence of Electrode Roughness on Cyclic Voltammetry". In: *J Phys Chem C* 112.37 (Sept. 2008), pp. 14428–14438.

[57] Gwan-Hong Min et al. "Synthesis and Properties of Ionic Liquids: Imidazolium Tetrafluoroborates with Unsaturated Side Chains". In: *Bulletin of the Korean Chemical Society* 27.6 (Jan. 2006), pp. 847–852.

[58] Manickam Minakshi and Mihail Ionescu. "Anodic behavior of zinc in Zn-MnO". In: *International Journal of Hydrogen Energy* 35.14 (July 2010), pp. 7618–7622.

[59] Manickam Minakshi et al. "The Zn–MnO2 Battery: The Influence of Aqueous LiOH and KOH Electrolytes on the Intercalation Mechanism". In: *Electrochemical and Solid-State Letters* 11.8 (), A145–A149.

[60] J Newman and C Tobias. "Theoretical Analysis of Current Distribution in Porous Electrodes". In: *Journal of the Electrochemical Society* 109.12 (), pp. 1183–1191.

[61] Helen L Ngo et al. "Thermal properties of imidazolium ionic liquids". In: *Thermochimica Acta* 357-358 (Aug. 2000), pp. 97–102.

[62] Hiroyuki Ohno. *Electrochemical Aspects of Ionic Liquids*. Wiley, May 2011.

[63] Mark E Orazem and Bernard Tribollet. *Electrochemical Impedance Spectroscopy*. John Wiley & Sons, Oct. 2011.

[64] Myounggu Park et al. "A review of conduction phenomena in Li-ion batteries". In: *J Power Sources* 195.24 (July 2010), pp. 7904–7929.

[65] V Prasad, D Semwogerere, and Eric R Weeks. "Confocal microscopy of colloids". In: *J. Phys.: Condens. Matter* 19.11 (Feb. 2007), p. 113102.

[66] S Ramesh. "Atypical behaviors of BMIMTf ionic liquid present in ionic conductivity, SEM, and TG/DTG analyses of P (VdF-HFP)/LiTf-based solid polymer electrolyte system". In: *Journal of Materials Research* (2011).

[67] S Ramesh et al. "Enhancement of ionic conductivity and structural properties by 1-butyl-3-methylimidazolium trifluoromethanesulfonate ionic liquid in poly(vinylidene fluoride-hexafluoropropylene)-based polymer electrolytes". In: *ChemPhysChem* 126.S2 (May 2012), E484–E492.

[68] J. Ranke et al. "Explaining ionic liquid water solubility in terms of cation and anion hydrophobicity". In: *International Journal of Molecular Sciences* 10.3 (2009), pp. 1271–1289.

[69] Luís P N Rebelo et al. "On the Critical Temperature, Normal Boiling Point, and Vapor Pressure of Ionic Liquids". In: *J. Phys. Chem. B* 109.13 (Apr. 2005), pp. 6040–6043.

[70] Eugen Scholz. *Karl Fischer Titration*. Determination of Water. Springer, Nov. 2011.

[71] Kenneth R. Seddon et al. "Influence of chloride, water, and organic solvents on the physical properties of ionic liquids". In: *Pure Appl. Chem.* 72.12 (2000), pp. 2275–2287.

[72] M. Shamsipur et al. "Physical and electrochemical properties of ionic liquids 1-ethyl-3-methylimidazolium tetrafluoroborate, 1-butyl-3-methylimidazolium trifluoromethanesulfonate and 1-butyl-1-methylpyrrolidinium bis (trifluoromethylsulfonyl) imide". In: *J Mol Liq* 157.1 (2010), pp. 43–50.

[73] S Slane. "Composite gel electrolyte for rechargeable lithium batteries". In: *J Power Sources* (1995).

[74] J Y Song, Y Y Wang, and C C Wan. "Review of gel-type polymer electrolytes for lithium-ion batteries". In: *J Power Sources* 77.2 (Feb. 1999), pp. 183–197.

[75] V Srikant and D R Clarke. "On the optical band gap of zinc oxide". In: *J. Appl. Phys.* 83.10 (1998), p. 5447.

[76] V Subramanian et al. "Printed electronics for low-cost electronic systems: Technology status and application development". In: *Solid-State Circuits Conference, 2008. ESSCIRC 2008. 34th European*. 2008, pp. 17–24.

[77] Waiping G Tam and Jesse S Wainright. "A microfabricated nickel-hydrogen battery using thick film printing techniques". In: *J Power Sources* 165.1 (2007), pp. 481–488.

[78] José S Torrecilla et al. "Effect of Relative Humidity of Air on Density, Apparent Molar Volume, Viscosity, Surface Tension, and Water Content of 1-Ethyl-3-methylimidazolium Ethylsulfate Ionic Liquid". In: *J Chem Eng Data* 53.4 (Apr. 2008), pp. 923–928.

[79] Mingsong Wang et al. "Rapid room-temperature synthesis of nanosheet-assembled ZnO mesocrystals with excellent photocatalytic activity". In: *CrystEngComm* 15.4 (2013), pp. 754–763.

[80] Zuoqian Wang et al. "Development of a Zinc-Based Battery System for Grid-Scale Energy Storage and Application of Flexographic Printing for the Fabrication". In: *Meeting Abstracts* (2012).

[81] Peter Wasserscheid and Annegret Stark. *Handbook of Green Chemistry, Green Solvents, Ionic Liquids*. John Wiley & Sons, Apr. 2014.

[82] Peter Wasserscheid and Tom Welton. *Ionic Liquids in Synthesis*. 2nd. Vol. 1st. Weinheim: Wiley-VCH Verlag GmbH & Co.

[83] Gene Whyman, Edward Bormashenko, and Tamir Stein. "The rigorous derivation of Young, Cassie-Baxter and Wenzel equations and the analysis of the contact angle hysteresis phenomenon". In: *Chemical Physics Letters* 450.4-6 (2008), pp. 355–359.

[84] R Winslow et al. "Development and manufacture of printable next-generation gel polymer ionic liquid electrolyte for Zn/MnO2 batteries". In: *Journal of Physics: ...* (2013).

[85] Jun John Xu, Hui Ye, and Jian Huang. "Novel zinc ion conducting polymer gel electrolytes based on ionic liquids". In: *Electrochemistry Communications* 7.12 (Dec. 2005), pp. 1309–1317.

[86] M Xu et al. "The state of water in 1-butly-1-methyl-pyrrolidinium bis (trifluoromethanesulfonyl)imide and its effect on Zn/Zn(II) redox behavior". In: *Electrochimica Acta* 97 (May 2013), pp. 289–295.

[87] Hui Ye et al. "Li Ion Conducting Polymer Gel Electrolytes Based on Ionic Liquid/PVDF-HFP Blends". In: *Journal of the Electrochemical Society* 154.11 (2007), A1048.

[88] Yun-Sheng Ye, John Rick, and Bing-Joe Hwang. "Ionic liquid polymer electrolytes". In: *J. Mater. Chem. A* 1.8 (2013), p. 2719.

[89] Weilie Zhou and Zhong Lin Wang. *Scanning Microscopy for Nanotechnology*. Techniques and Applications. Springer Science & Business Media, Mar. 2007.